Analysis of Two-point Turbulence Measurements for Aeroacoustics

Christian W. Wenger

Thesis submitted to the Faculty of the
Virginia Polytechnic Institute and State University
in partial fulfillment of the requirements for the degree of

Master of Science
in
Aerospace Engineering

Dr. William Devenport, Chair
Dr. Bernard Grossman
Dr. Roger Simpson

January 8, 1999
Blacksburg, Virginia

Keywords: Aeroacoustics, Turbulence, Two-point Measurements, Wave Number Frequency Spectra, Space-time Correlations, Blade-wake Interaction, Rotor wake/Stator Interaction

Analysis of Two-point Turbulence Measurements for Aeroacoustics

Christian W. Wenger

(ABSTRACT)

Simultaneous two-point three-component four-sensor hot-wire velocity measurements taken in three flows of aeroacoustic interest are here analyzed. The analyses provide information on the turbulence structure of the flows as it would be encountered by hypothetical noise producing blades passing through the flows. Two-point measurements taken in the first flow, a lifting wake from a rectangular NACA 0012 half wing, are used to calculate space-time correlation functions and 'pointwise' wave number frequency spectra. Two upwash spectra, calculated for locations in the region of the wake that is roughly homogenous in the spanwise direction, are direct estimates of the full wave number frequency spectra at their locations. As such, they are used to perform aeroacoustic calculations, and the results are compared to results achieved using the von Kármán isotropic spectrum. Amiet's approximation, where the wave number frequency spectra can be represented by the correlation length scales is found to hold reasonably well for the measured spectra.

The two-point measurements in the second flow, a vortex/blade-tip interaction, are analyzed to provide information useful to researchers of blade-wake interaction noise produced by helicopter rotors. Space-time correlation functions and wave number frequency spectra are calculated for five cuts through the region of interaction. The correlation functions provide information concerning the turbulence length scales found in the interaction region. The spectra are compared to the von Kármán isotropic spectrum and found to be greatly different. However, the spectra do bear some resemblance to spectra calculated in the spanwise homogenous region of the lifting wake.

The two-point measurements taken in the third flow, the wake from a fan cascade, are analyzed to provide information of use to modelers of broadband noise produced through rotor wake/stator interactions. In particular, space-time correlation functions are calculated for a grid of two-point measurements, which allows the estimation of the turbulence structure as seen by a passing stator blade. Space-time correlation functions and wave number frequency spectra are calculated for various stator configurations. The implications of engine operating speed and stator configuration for broadband noise production are discussed.

ACKNOWLEDGEMENTS

Foremost appreciation goes to my parents, Wade and Eunice Wenger, who despite the uncertainties of child raising managed to instill within me a desire to accomplish. Without their support, both moral and other, this thesis would never have been completed.

Appreciation for his direct involvement with this work goes to my advisor, Dr. William Devenport. Without his selfless patience and guidance, none of this work would have been produced by me. Dr. Devenport has exemplified those spirits of exploration and pedagogical excellence, which characterize the best aspects of the academic community.

I would also like to thank the other experimenters who were responsible for taking the data, which I analyzed in this work. Those are Dr. Ken Wittmer and Joe Miranda.

Thanks to the financial sponsors of this work, Drs. Tom Brooks, Casey Burley, and Joe Posey at NASA Langley (grants NAG-1-1539, NAG-1-1942, and NAG-1-1801) and Dr. L. Patrick Purtnell at ONR (grants N00014-94-1-0744 and N00014-96-1-0970).

TABLE OF CONTENTS

CHAPTER 1. INTRODUCTION

Over the past few decades the use of helicopters and turbomachinery has increased to the extent that noise pollution has become a serious nuisance. Maxwell and Evans (1998) have even found that noise from a major airport hinders children's learning abilities at a nearby school. In light of such concerns, significant efforts have been underway for some years now to reduce noise produced by helicopter rotors and aircraft engines.

1.1. Helicopter Rotor Noise Research

Much work has been conducted to identify specific sources of helicopter rotor noise, as exemplified by the work of Brooks *et al*. (1987). In this study, the interaction of the rotor blades with their own wakes (blade-wake interaction or BWI) was found to be the dominant source of broadband noise production during level-flight and mild climb conditions.

Helicopter rotor wakes are dominated by the spiral turbulence associated with the tip vortices produced by the rotors. According to Glegg (1991), Burley *et al*. (1997), and Brezillion *et al*. (1997), the most significant production of BWI noise occurs as a result of perpendicular interactions between the tip vortices and the rotors. To aid in the development of BWI noise reducing rotor designs, Glegg (1991) developed a BWI prediction method based on the seminal aeroacoustic work of Amiet (1975), which gives a general method for predicting the noise produced by a simple airfoil in a turbulent flow. Burley *et al*. (1997) have also developed a prediction scheme, which relates surface pressure fluctuations to far-field noise radiation.

Both prediction methods require knowledge of the turbulent wake structure. In particular, Glegg's method requires that the turbulent wake structure be expressed in terms of its upwash wave number frequency spectrum, which gives the intensity of the upwash velocity fluctuations and the spanwise length scales at each frequency associated with those motions. Such knowledge has not been readily available for helicopter rotor wakes. As such, both Glegg (1991) and Burley *et al*. (1997) express the need for work to determine the turbulent structure of rotor wakes.

In order to satisfy some of the need for such research, Glegg and Devenport (1992) and Devenport *et al*. (1996) measured the turbulence structure of a tip vortex shed from a rectangular half wing. Then, Wittmer *et al*. (1995) and Wittmer (1996) went on to study the idealized perpendicular interaction between a tip vortex shed by a rectangular half wing and another fixed wing. Based on these measurements, Glegg and Devenport (1992) and Glegg *et al*. (1997) determined that the turbulence in an undisturbed tip vortex is insufficient to produce most of the BWI noise generated when interacting with helicopter rotors. However, the perpendicular interaction between the tip vortex and the fixed wing was found to cause turbulent breakdown of the vortex and the rapid growth of the spiral turbulence surrounding it. Thus, it was determined that such interactions as would be found in helicopter rotor flows could generate sufficient turbulence to account for the BWI noise measured in previous experiments. Brezillon *et al*. (1997) has confirmed that, indeed, more BWI noise is produced from rotor encounters with vortices that have undergone previous rotor interactions, as compared to that produced by encounters with previously undisturbed vortices.

1.2. Fan Noise Research

In a study of current technology available at the time for the reduction of noise in aircraft engines, Gliebe (1992) states that fan noise has become a significant contributor to overall noise output in engines with ultra high bypass ratios. He also states that fan noise reduction methods, such as those explored by Dittmar and Woodward (1976), have not been sufficient to reduce noise to satisfactory levels. Dittmar and Woodward redesigned a fan stage to reduce stator lift fluctuations by increasing the stator chord and adjusting incidence angles. Therefore, according to Gliebe (1992) "new and novel ideas and concepts must be explored, developed and demonstrated..."

More recently, significant advances have been made toward prediction and reduction of tone noise in high bypass ratio engines. In order to validate the state-of-the-art prediction code, the *V072 Rotor Wake/Stator Interaction Code,* Sutliff *et al*. (1997) compared predictions with experimentally measured mode levels for noise produced by the 48 inch Active Noise Control Fan at NASA Lewis Research Center. The predictions were made using both single two-component hot-wire wake measurements and wake

models. The code was found to produce fairly accurate results using both the measured input data and the model input data.

According to Glegg and Jochault (1997), the ultra high bypass ratios and lower rotational fan speeds of modern engines have reduced tone noise to the extent that broadband noise is now of at least equal concern. Glegg and Jochault identify two main types of broadband noise produced by fan stages, self noise and inflow noise. Self noise is produced by the interaction of turbulence generated close to a blade surface with the blade itself. Inflow noise is produced by the interaction of blades with turbulence that was generated upstream, such as rotor wake/stator interactions. In their study, Glegg and Jochault present a method to predict the broadband self noise produced in a ducted fan.

1.3. The Purpose of the Present Work

This work aims to contribute to noise reduction efforts for both helicopter rotors and high bypass ratio engine fans by analyzing two-point turbulence measurements that were taken by other researchers in three flows relevant to these two fields. These flows have previously been examined by others using single-point turbulence measurements, however, two-point measurements are able to provide cross-correlation data that are unavailable from the single-point measurements. The cross-correlation data provides information on the turbulence length scales found in each flow. This information is designed to facilitate further research, in which noise reduction/prediction methods would be improved or developed for helicopter rotors and engine fans.

The second chapter gives a basic description of the hot-wire instrumentation used by the experimenters who took the two-point data that is here analyzed. The third chapter is devoted to the analysis of two-point measurements taken by Miranda (1996) in the lifting wake of a rectangular half wing. A description of his experimental setup is given along with a summary of the results from his single-point data analysis. The two-point measurements are then analyzed to provide fundamental aeroacoustic information concerning this basic flow. Wave number frequency spectra are calculated at two locations within the two-dimensional wake, one location in the spiral wake surrounding the tip vortex, and in the tip vortex itself. Because, the turbulence in the two-dimensional wake is approximately homogenous in the spanwise direction, the wave number

frequency spectra calculated in this region can be used directly in the noise prediction methods of Glegg (1991) and Amiet (1975). As such, some aeroacoustic calculations are performed and their implications are discussed. These two-point measurements also served to test analysis methods that were later used on the other, more complex flows. The conclusions based on the two-point results in this flow are outlined.

The fourth chapter covers the analysis of two-point measurements taken by Devenport *et al.* (1997) in a flow modeling the interaction of a tip vortex shed by a rectangular half wing with the tip vortex from another downstream half wing. This flow was designed to provide data of direct interest to researchers studying BWI noise produced by helicopter rotors. This type of interaction has also been identified by Burley *et al*. (1997) and Brezillon *et al*. (1997) as a significant source of BWI noise during level flight and mild climbing conditions. In this flow, a tip vortex passes near the tip of a downstream half wing, and the two vortices wind up around each other. A description of the experimental setup is given along with a summary of the results from his single-point data analysis. The two-point hot-wire measurements taken at various locations in the region of interaction are then analyzed to provide information concerning the turbulence length scales that would be encountered by a hypothetical noise producing blade passing through this region. The conclusions based on the two-point results in this flow are outlined.

Chapter 5 deals with the analysis of two-point measurements taken by Wenger *et al*. (1998) in a fan cascade wind tunnel built by Muthanna (1998). This flow was designed to model the flow through a fan stage of a high bypass ratio jet engine. As before, a basic description of the experimental setup is given and the single-point results are summarized. As noted above much work has been done to develop prediction methods for fan tone noise and broadband self noise. However, methods for predicting broadband inflow noise are still lacking adequate flow information. Therefore, the two-point hot-wire measurements are here analyzed to provide data on the turbulence structure that will be of use to future developers of prediction methods for rotor wake/stator interaction noise. Because the noise is produced by the interaction of rotor turbulence with the downstream stators, the two-point data is analyzed to determine the length scales of the turbulence as seen by stators moving tangentially relative to the

rotors. The implications of engine operating speed and stator configuration for noise production are discussed. The conclusions based on the two-point results from this flow are outlined.

Finally, chapter 6 summarizes the conclusions arrived at in the discussions of the two-point results in chapters 3, 4 and 5.

CHAPTER 2. HOT-WIRE ANEMOMETRY

While no measurements were made as part of the present study, all the data analyzed here were obtained using the same hot-wire techniques. Therefore, a summary description of these techniques is included in this chapter. All simultaneous two-point, three-component hot-wire measurements analyzed in this study were taken using a computerized system described in detail by Wittmer *et al*. (1997) and Devenport *et al*. (1996). The miniature four-sensor hot-wire probes were manufactured by Auspex Corporation (type AVOP-4-100). Each probe has two orthogonal X-wire arrays with each sensor inclined at a nominal 45° angle to the probe axis. The probe tip occupies a measurement volume of approximately 0.5 mm^3.

Each of the eight hot-wire sensors is operated separately using a Dantec 56C17/56C01 constant temperature anemometer unit. The anemometer bridges are optimized to give a matched frequency response greater than 20 kHz. For each sensor/cable/bridge combination, the magnitude and phase response calibrations were measured by shining the beam of a pulsed YAG laser on the hot-wire sensor in a flow. The laser pulses appear as impulses to the sensor/cable/bridge combination, and thus, the dynamic response of the combination can be determined from the bridge outputs. Using this method, the magnitude response of the probes was determined to be flat from zero Hz to a 3dB point close to 22kHz (Muthanna, 1998). The phase responses of the individual hot-wire sensors are also closely matched.

During a measurement, the output voltages from the anemometer bridges are recorded by an IBM AT compatible computer using an Analogic 12 bit HSDAS-12 A/D converter. Before being sampled, the hot-wire signals pass through $\times 10$ buck-and-gain amplifiers with calibrated RC-filters that limit the frequency response to 50 kHz. The A/D converter is also used to sample voltage outputs from a digital thermometer and pressure transducer.

The hot-wire probes are calibrated for velocity before and after each session of measurement-taking by placing them in the uniform jet of a TSI calibrator. King's law is used to correlate the hot-wire output voltages with the cooling velocities. To determine the velocity components from the cooling velocities, a direct angle calibration was

performed. During a direct angle calibration the probe was pitched and yawed over the acceptance cone of the probe in the calibrator jet. By comparing the known pitch and yaw angles with probe outputs, the true relationship between the cooling velocities and the flow angle can be determined. The hot-wire measurements are corrected for ambient temperature drift using the method of Bearman (1971). Wittmer (1996) performed studies to ensure that angle calibration does not vary excessively with flow velocity. His results showed that for velocities between 62 and 112 ft/s (19-34 m/s) the direct angle calibration at selected points varies by less than 1%.

CHAPTER 3. ANALYSIS OF TWO-POINT MEASUREMENTS IN A TIP VORTEX FLOW

3.1. Nomenclature

c – chord length

x, y, z – coordinates describing location within flow

u, v, w – velocity components

K_x – nominal streamwise wave number calculated from angular frequency using Taylor's hypothesis, $K_x = \omega/U_\infty$

k_y – spanwise wave number

f – frequency

ω – angular frequency

U_∞ – free stream velocity

$S_{pp}()$ – far-field acoustic power spectral density

ρ_0 – density of flow

c_0 – speed of sound

$\sigma = \sqrt{x^2 + b^2\left(y^2 + z^2\right)}$

$\beta = \sqrt{1 - M^2}$

M – Mach number

b – the semi-chord of an airfoil

d – the semi-span of an airfoil

$L()$ – the transfer function giving the lift response of an airfoil passing through a turbulent flow

$j = \sqrt{-1}$

θ – angular position above an airfoil relative to a vertical axis

Δy – spanwise probe separation

i and k – indices, 1 to 3, indicating velocity component

$\Phi_{ii}()$ – the wave number frequency spectrum calculated from the ith velocity fluctuations

$\phi_{ii}()$ – the 'pointwise' wave number frequency spectrum calculated from the *i*th velocity fluctuations

$G_{ii}()$ – the cross-spectrum between two time dependent velocity signals calculated from the *i*th velocity component

T – the duration of a velocity measurement

E[] – the expected value operation

R – the maximum probe separation in a series of two-point measurements

τ - time delay

$l_y()$ – correlation length scale

L – integral length scale

$R_{ii}()$ – space-time correlation function calculated from the *i*th velocity component

V_s – velocity component in the direction following the center of the spiral wake

U_s – local velocity scale

L_s – local length scale

n – coordinate specifying normal distance from center line of spiral wake

$$k_e = \left(\frac{\Gamma\left(\frac{5}{6}\right)}{\Gamma\left(\frac{1}{3}\right)} \right) \left(\frac{\sqrt{p}}{L} \right)$$

$\Gamma()$ – the gamma function

$D()$ – directionality

$\overline{u^2}, \overline{v^2}, \overline{w^2}$ – variances for the fluctuations of the three velocity components

3.2. Introduction

Two-point profiles were measured by Miranda (1996) in the wake of a half-wing set at an angle of attack, in order to study the turbulence correlations produced by a lifting wake. These are here analyzed by calculating space-time cross correlation functions, which are used to reveal the scales of the turbulence at the measured regions of the flow. Wave number frequency spectra are then computed from the correlation functions and compared with the von Kármán isotropic turbulence spectrum, which is often used in broadband noise calculations. The comparisons are used to examine the

implications that the differences have for prediction of the broadband noise produced by a hypothetical blade intersecting the wake.

3.3. Description of Miranda's (1996) Experiment and Single-Point Results

3.3.1. Experimental Setup

The flow was generated in the 3 x 2 x 20 ft^3 test section of the Virginia Tech Subsonic Wind Tunnel using a NACA 0012 half-wing of aspect ratio 6 and 5° angle of attack with a Reynolds number of 3.2 x 10^5 (based on .203 m chord, *c*). Flow qualification measurements in the Subsonic Wind Tunnel conducted by Engel () showed that the flow velocity varies across the potential core by no more than 0.4% with turbulence levels of approximately 0.2% to 0.3%. The wing was mounted horizontally in the test section at midheight and extended 2 feet across its width. Figure 3.1 is a diagram showing the location of the wing and the measurement plane in the test section. Boundary layer trips made of glass beads were installed on both sides of the airfoil to avoid instability associated with transition and to increase the Reynolds number of the axial wake.

The two probes were mounted on a computer controlled holder (shown in figure 3.2), which allowed the separation between the two probes to be varied. The fixed probe was held in a stationary mount on the holder, while the other probe was moved via a small computerized traverse. The holder itself was mounted on another computerized traverse, which allowed the two-point measurement location within the flow to be varied independently of the probe separation.

Miranda (1996) conducted probe interference studies using the two-probe holder. Helium bubble flow visualization showed that the flow was unaffected by the presence of the holder at the measurement location. Velocity measurements were also made, and a small effect of at most 0.7% change in the measured mean velocity was found for the smallest probe separation. Devenport *et al.* (1996) predicted the approximate magnitude of this effect using a potential flow model of a single four-sensor hot-wire probe.

3.3.2. Single-point Results

The general flow 10 chord lengths downstream of the wing leading edge (the location of the two-point measurements) structure can be seen in figure 3.3, which shows contours of axial turbulence normal stress normalized on the freestream velocity. The origin of the coordinate system is located at the same downstream location as the wing leading edge. The y = 0 and z = 0 coordinates are located such that they coincide with the vortex core 10 chord lengths downstream of the origin. As shown in figure 3.1, the *x*, *u* direction is pointed downstream, the *y*, *v* direction is pointed away from the tip of the wing, and the *z*, *w* direction is pointed such that it completes the right handed coordinate system.

The wake consists of an inboard region of two-dimensional flow that winds up into a circulating velocity field about a small concentrated vortex core. In the two-dimensional region, the flow is nearly homogeneous in the spanwise *y* direction. Mean velocity and turbulence stress profiles in this region are similar to those measured by Wygnanski *et al*. (1986), Townsend (1956), and Antonia and Britz (1989) in equilibrium two-dimensional turbulent wakes. At this downstream location (10*c*) the half-thickness of the wake is .083*c*. The autospectrum of the upwash (*w* – component) velocity fluctuations at the furthest inboard fixed probe location (point A on figure 3.3), shown in figure 3.4, has a peak at $K_x c = \omega c/U_\infty \approx 20$, which presumably indicates the passage frequency of the spanwise-oriented eddies that one would expect to dominate this flow.

Closer to the vortex, the wake is wound up by the circulating velocity field, and experiences lateral stretching, curvature, and skewing. As Keffer (1965) reports, stretching thins a wake as well as organizes and intensifies the dominant spanwise eddies. This increases the axial turbulence levels to a maximum near $y/c = .2$ and $z/c = -.4$. As the wake continues to thin, turbulence levels fall. In the vortex core, the turbulence levels drop despite the seeming increase shown in figure 3.3. This apparent increase is really caused by vortex wandering, which appears as increased turbulence levels due to the high-velocity gradients in the core. Miranda and Devenport (1998) estimated the rms amplitude of the wandering to be .35%*c*. The autospectrum of the upwash velocity fluctuations taken at point D (figure 3.4) shows high spectral levels at low frequencies, $K_x c < 20$, and low levels at high frequencies, $K_x c > 200$, which indicates an absence of

small scale turbulence. Indeed, Devenport et al. (1996) showed that the core is, in fact, laminar.

3.3.3. Two-point Data Acquisition

Four two-point profiles, shown in figure 3.3, were taken by Miranda (1996) at a downstream location of 10*c*. For each profile, the fixed probe location is indicated by the letters A-D, and the series of locations where the movable probe took data is indicated by the lines extending from the fixed probe points, L1- L4. Profile A/L1 is located far from the tip vortex, in the nearly two-dimensional region of the flow. Profile B/L2 lies in the region of maximum turbulence levels caused by spanwise stretching of the wake. Profile C/L3 is located in the highly curved and strained region above the tip vortex, and, finally, profile D/L4 extends radially from the core center.

The smallest probe separation for each two-point profile was 3 mm (0.0158*c*). Considering the 0.8 mm diameter of the probe measurement volumes, it is unlikely that measurements at smaller separations would be meaningful. It order to keep probe interference to a minimum at the smallest separations, Miranda (1996) angled the probes toward each other by about two degrees each as depicted in figure 3.2. The velocity vectors were then correspondingly rotated back during processing.

Two-point profile A/L1 consists of 73 two-point measurements with a maximum probe separation of 2.56 in. (0.32*c*). Profile B/L2 consists of 80 measurements with a maximum probe separation of 3.04 in. (.38*c*). Profile C/L3 is shorter with only 49 measurements and a maximum probe separation of 1.12 in. (.14*c*). Profile D/L4 has only 34 measurements, but extends to a maximum probe separation of 2.4 in. (0.3*c*). At each probe separation of each two-point profile, 100 records of 3072 samples were taken for each of the eight hot-wire sensors. The samples, taken at a frequency of 50 kHz with breaks between the records, cover a total time of two minutes per measurement.

3.4. Two-point Results and Discussion

3.4.1. Data Analysis

Amiet (1975) presented a method for calculating the broadband noise produced by an airfoil in a turbulent flow. According to his formulation, the far-field acoustic power spectral density produced by the airfoil is

$$S_{pp}(x,y,z,w) = \left(\frac{wzr_0 b}{c_0 s^2}\right)^2 pU_\infty d \left| L(x, K_x, \frac{wy}{c_0 s}) \right|^2 \Phi_{ww}(K_x, \frac{wy}{c_0 s}), \qquad (3.1)$$

where (x, y, z) is the location of the observer relative to the noise producing airfoil as shown in figure 3.5, w is the angular frequency, ρ_0 is the air density, b is the semi-chord, c_0 is the speed of sound, $s = \sqrt{x^2 + b^2(y^2 + z^2)}$, U_∞ is the free stream velocity, d is the semi-span of the noise producing airfoil, $b = \sqrt{1 - M^2}$, and M is the Mach number. The function $L(x, K_x, \frac{wy}{c_0 s})$ is a transfer function, which gives the lift response of the hypothetical airfoil passing through the turbulent flow. An exact expression can be derived for this, if the airfoil is idealized as a semi-infinite flat plate (Devenport *et al*., 1998). This expression is,

$$L\left(x, K_x, \frac{wy}{c_0 s}\right) = \frac{b}{jpK_x \sqrt{M(1 + M\cos q)(\cos q - x/s)}} \qquad (3.2)$$

where θ is the spanwise location of an observer located directly over the airfoil, as shown in figure 3.5.

The function $\Phi_{ww}()$ is the wave number frequency spectrum of the upwash velocity fluctuations. This spectrum is the distribution of energy over the frequencies, expressed as nominal streamwise wave numbers by invoking Taylor's hypothesis, and spanwise wave numbers of the turbulence encountered by the leading edge of the airfoil as it passes through the flow. For general flows, this spectrum is unknown. Therefore, the spectrum based on the von Kármán model of isotropic turbulence (shown in figure 3.6) is typically used in the calculations. The contours of the spectrum are semi-circular, because the turbulence properties are identical in every direction. The spectral levels increase from zero at the origin to a semi-circular peak then decay at higher wave

numbers.

Wave number frequency spectra were calculated from data taken by Miranda (1996. Miranda (1996) took two-point profiles in the spanwise direction only, therefore in this chapter, the locations of the movable probe will simply be expressed relative to the fixed probe location as probe separations denoted by the symbol Δy.

The definition used in this study to calculate wave number frequency spectrum of the *i* - component velocity fluctuations from a profile of two-point measurements (Amiet, 1975) is

$$f_{ii}(y,k_y,w)=\frac{1}{2p}\int_{-\infty}^{\infty}G_{ii}(y,\Delta y,w)e^{-jk_y\Delta y}d\Delta y\,, \tag{3.3}$$

where *y'* is the probe separation, and *w* is the angular frequency. $G_{ii}(y,\Delta y,w)$ is the cross-spectrum of the *i* - velocity component between the velocity signals at *y* and $y + \Delta y$. $G_{ii}(y,\Delta y,w)$ was calculated using the definition

$$G_{ii}(y,\Delta y,w)=\lim_{T\to\infty}\left(\frac{p}{T}\right)E[v_i{}^*(y,w)v_i(y+\Delta y,w)] \tag{3.4}$$

where *E*[] is the expected value operator. Definition 3.3 is simply the Fourier transform of the cross-spectrum with respect to probe separation (Bracewell, 1986).

The definition given by equation 3.3 does not produce precisely the same wave number frequency spectra as that used in equation 3.1. Rather, equation 3.3 is a 'pointwise' definition, meaning that the spectra are calculated from two-point data gathered for only one fixed probe location. Rigorously, the wave number frequency spectrum is defined as the double Fourier transform of the space-time velocity autocorrelation function,

$$\Phi_{ii}(w,k_y)=\frac{1}{4p^2}\int_{-\infty}^{\infty}\int_{-\infty}^{\infty}\lim_{T\to\infty}\frac{1}{RT}\int_{-T/2}^{T/2}\int_{-R/2}^{R/2}w(y,t)w(y+\Delta y,t+t)dydte^{-jwt}e^{-jk_y\Delta y}dtd\Delta y \tag{3.5}$$

where *R*/2 is the greatest probe separation. If the two-point cross-spectrum, $G_{ii}(y,\Delta y,w)$, is substituted into this equation, the definition becomes

$$\Phi_{ii}(w,k_y)=\frac{1}{2pR}\int_{-\infty}^{\infty}\int_{-R/2}^{R/2}G_{ii}(y,\Delta y,w)dye^{-jk_y\Delta y}d\Delta y \tag{3.6}$$

And now substituting in the pointwise definition given in equation 3.3,

$$\Phi_{ii}(w,k_y) = \frac{1}{R}\int_{-R/2}^{R/2} f(y,k_y,w)dy \tag{3.7}$$

From this equation, it can be seen that the rigorous definition of the wave number frequency spectra is simply the average over all probe separations of the pointwise wave number frequency spectra. The pointwise definition becomes the same as the rigorous definition for flows homogeneous in *y,* because equation 3.3 becomes independent of the *y* location in the flow. Later in this chapter, several rigorous wave number frequency spectra are estimated using two-point data taken by Miranda (1996) in roughly spanwise homogeneous flow. However, in general, the wave number frequency spectra in this study are calculated from data taken in highly inhomogeneous flows, and the differences between the rigorous and pointwise definitions must be kept in mind.

While the rigorous definition could theoretically be used to calculate wave number frequency spectra, the amount of data necessary for this is many times greater than that needed using the pointwise definition. Also, the averaging involved in calculating such spectra would likely mask valuable information concerning the turbulence structure of the flow in the vicinity of the fixed probe locations.

The Fourier transforms of $G_{ii}(y,\Delta y,w)$ with respect to probe separation were performed using a Fast Fourier Transform (FFT) algorithm. To use this, it was necessary for the data to be double sided and evenly spaced with a total number for values equal to a power of 2. Miranda's (1996) two-point profiles included only positive probe separations, and the data were not evenly spaced or in sets with the number of separations equal to powers of 2. Therefore, the data were mirrored to the negative probe separations, interpolated to even spacings equal to the smallest actual probe separation in each two-point profile, and the values were zero-padded to a length of a power of 2. Because the data were symmetrical about the zero probe separation axis, the resulting wave number frequency spectra were also symmetrical and entirely real.

In order to be sure that the process described above would produce functions that are well conditioned for Fast Fourier Transforming, the variation of the cross-spectra with respect to probe separation was examined. The cross-spectral density, defined as the

cross-spectra as a function of probe separation, calculated from profile A/L1 (see figure 3.3) is shown in figure 3.7. In this figure, the contours of cross-spectral density are plotted against normalized frequency along the vertical axis and normalized probe separation along the horizontal axis. The frequency is normalized by the chord length, c, of the airfoil used to generate the tip-vortex and by the free stream velocity, U_∞. The probe separation is also normalized by the chord length, c, and the density levels are normalized by the chord length and the free stream velocity.

From this figure, it can be seen that the function is generally well defined, in particular the probe separations are large enough to capture the complete decay to zero at large Δy. However, as the frequency increases, the peak along the $\Delta y/c = 0$ axis becomes sharper and sharper until it resembles a delta function. Given the limitations on the smallest probe separation, this feature cannot be completely defined at higher frequencies. The smallest probe separation is critical also, because it determines the maximum spanwise wave number at which the wave number frequency spectra are known. If the smallest probe separation is too large, the wave number frequency spectra will suffer from aliasing.

To be certain that the smallest probe separation (3 mm) in Miranda's (1996) two-point data profiles was small enough to avoid problems with aliasing, the upwash wave number frequency spectrum for profile A/L1 (shown in figure 3.8A) was calculated using the above process. Then, for comparison, the same wave number frequency spectrum was recalculated with a significantly reduced effective smallest probe separation. To do this, data based on the Liepmann model of isotropic turbulence was added at separations below the smallest measured probe separation. The wave number frequency spectrum calculated using this supplemented cross-spectral density is shown in figure 3.8B. It can be seen that there is virtually no difference between the two spectra. Thus, it was decided that the measurement limitations on the smallest probe separation did not pose a problem in calculating accurate wave number frequency spectra. All wave number frequency spectra were then simply calculated using the smallest probe separation as the increment in the FFT routine.

As a compact means of characterizing wave number frequency spectra, Amiet (1975) defines the spanwise correlation length scale as a function of frequency. His definition is modified here to account for inhomogeneous turbulence.

$$l_y(w) = \frac{1}{G_{ww}(y,0,w)} \int_0^\infty G_{ww}(y,\Delta y,w)\, d\Delta y \tag{3.8}$$

It should be noted that this definition applies when only positive probe separations are known. If both positive and negative separations are known, then the lower limit of integration would be negative infinity, and the integral would also be divided by two. This definition simply corresponds to the wave number frequency spectra along the $k_y c$ = 0 axis divided by the autospectrum at the fixed probe location.

$$l_y(w) = \frac{p}{U_\infty} \frac{f_{ww}(y,0,w)}{G_{ww}(y,0,w)} \tag{3.9}$$

Amiet used the correlation length scale to simplify equation 3.1 in the case where the wave number frequency spectrum is relatively constant with respect to the spanwise wave number. In this case, the wave number frequency spectrum is well characterized at all spanwise wave numbers by the spectral levels along the $k_y c = 0$ axis.

The integral length scale commonly defined as

$$L_{u,x} = \int R_{uu}(x)\, dx \tag{3.10}$$

is also of interest, because it has been used to nondimensionalize wave number frequency spectra (Amiet 1975). This definition calculates the integral length scale by integrating the autocorrelation coefficient function of the u - component velocity fluctuations in the streamwise direction. The integral length scale can also be defined using different velocity components and by integrating in different directions. In general,

$$L_{i,k} = \int R_{ii}(x_k)\, dx_k \tag{3.11}$$

For isotropic turbulence, the first definition is sufficient, because the turbulence is identical in all velocity components and in all directions.

While wave number frequency spectra are necessary for aeroacoustic calculations, the fluid dynamic information present in them is often better presented in the form of circular space-time correlation functions. These are simply defined here as the inverse Fourier transform of the cross-spectra

$$R_{ii}(y,\Delta y,t) = \int_{-\infty}^{\infty} G_{ii}(y,\Delta y,w)e^{jwt}\,d\Delta y \qquad (3.12)$$

This operation results in correlations that are functions of probe separation and time delay.

The space-time correlation functions can be particularly useful in making physical interpretations concerning turbulence structures, if Taylor's hypothesis is used to express time delay as streamwise distance. So doing allows the average streamwise and spanwise extents of the coherent turbulent structures to be inferred. The accuracy with which Taylor's hypothesis can be applied to a flow depends largely on the characteristic velocity of the turbulent fluctuations relative to the convection speed and also on the uniformity of the velocity field. With the flows here examined, there is certain to be some inaccuracy associated with the application of Taylor's hypothesis. However, Taylor's hypothesis remains the best tool available for making inferences concerning turbulence structure, since the results here obtained are designed to be qualitative in nature. It should also be noted that from an aeroacoustic point of view only the frequency domain is of interest, and as such the aeroacoustic results are not affect by the validity of Taylor's hypothesis.

3.4.2. Space-time Cross Correlation Functions

The three normal components of the space-time cross correlation function, $R_{ii}(y,\Delta y,z,0,\tau)$, for the two-point profiles are shown in figures 3.9 - 3.12. The correlation functions are plotted against $\Delta y/c$ and $\tau U_\infty/c$. Assuming Taylor's hypothesis, τU_∞ represents distance in the streamwise direction. As are all correlation plots in this work, these are normalized by the variance of the turbulent fluctuations in the corresponding velocity component at the fixed probe location.

The uncertainties of the space-time correlation functions were estimated by considering the relative bias uncertainties in the velocity fluctuations, the relative random uncertainties in the velocity fluctuations, and the total and effective number of samples per measurement. The uncertainty estimates also required an autocorrelation coefficient value, which was taken to be 0.1. The estimated uncertainties for the correlation plots calculated in this flow are ± 0.04 R_{uu}, R_{vv}, and R_{ww}.

Figure 3.9 shows the correlation functions for the two-point profile A/L1. Far wakes are known to be dominated by large-scale quasiperiodic eddies with smaller spanwise than streamwise extent (Barsoum, *et al.*, 1978). This can be readily seen in the u – component of the cross correlation function for profile A/L1. The eddies produce correlation over a region extending to ~0.15c in the streamwise direction but only to ~0.08c in the spanwise direction. The differences in length scales are also present in the v and w – components. The most striking feature in these plots is the degree of periodicity as shown by the large regions of negative correlation which extend to ~0.2c in both the streamwise and spanwise directions. From these regions, the streamwise spacing of the passing turbulent eddies can be estimated as ~0.2c assuming Taylor's hypothesis. The slant in the negative streamwise direction evident in the v – component indicates that the wave fronts of the v – velocity fluctuations are slanted toward the movable probe such that it experiences a particular v – fluctuation before the fixed probe does.

Figure 3.10 shows the three component of the correlation function calculated from the two-point profile, B/L2. At this location, spanwise length scales are larger relative to streamwise length scales, because spanwise stretching occurs as the wake begins to wind up into the tip vortex, thus organizing the turbulent eddies in the spanwise direction. Miranda (1996) calculated this rate of stretching at the fixed probe location to be $\frac{\partial(V_s / U_s)}{\partial(\mathrm{n/L_s})} = 0.2$, where V_s is the velocity in a direction following the curve of the center line of the spiral wake, U_s is the local velocity scale, $\mathrm{L_s}$ is the local length scale, and n is the coordinate specifying wake normal distance from the center line of spiral wake. In the u – component, this spanwise organization gives the correlation function a more isotropic form as compared to that of profile A/L1, with significant correlation up to ~0.1c in both directions. The v and w – components show increased degrees of periodicity (as compared to profile A/L1), indicated by the stronger regions of negative correlation. The outlying regions of positive correlation presumably correspond to wave fronts of eddies immediately following the eddy impinging on the probe at the time. Thus, the apparent eddy spacing is ~0.3c. The increased degree of periodicity is a result of the spanwise organization of the turbulent structures caused by the spanwise

stretching. Spanwise stretching also extends the correlations produced by the coherent structures to ~0.4*c* in the spanwise direction.

The correlation function for two-point profile C/L3 is shown in figure 3.11. The turbulence at this location (in the tangential velocity field of the vortex) is subject to rates of stretching and skewing that are comparable to the peak axial velocity gradients (Miranda and Devenport, 1996) in the flow. In general, the spanwise and streamwise extents of correlation are much smaller here, extending to at most ~0.15*c* in the *w* – component. There appears to be significant periodicity indicated in the *w* – component correlations. However, it is absent from the *v* – component.

The correlation function for profile D/L4, taken about the vortex center and shown in figure 3.12, is dominated by the wandering of the vortex core. In particular the *v* and *w* – components have significant correlation at small probe separations that reach up to ~0.8*c* in the streamwise direction. This is consistent with the very low-frequency motions of small spanwise extent that characterize vortex wandering. In the *w* – component, there is also a large region of negative correlation at probe separations around 0.1*c*. This region could result from core motions stimulated as the core is buffeted by the surrounding turbulence (Devenport et al. 1998).

3.4.3. Wave Number Frequency Spectra

Having calculated the cross-correlation functions for each two-point profile, the wave number frequency spectra (defined as the two dimensional Fourier Transform of the correlation functions) can be calculated. Figures 3.13 - 3.16 show the wave number frequency spectra for the three velocity components at each measurement location. The spectra are plotted against frequency expressed as nominal streamwise wave number, $K_x c$, by assuming Taylor's hypothesis and spanwise wave number, $k_y c$. The spectral levels have also been normalized by the mean square fluctuation of the relevant velocity component at the fixed probe location, so that each spectrum integrates to unity.

The uncertainties in the wave number frequency spectra were estimated by considering the number of independent averages used to form the time spectra and the absolute uncertainties in the turbulence normal stresses. The uncertainty estimates for the wave number frequency spectra calculated in this flow are ±12% for ϕ_{uu}, and ±14% for

ϕ_{vv} and ϕ_{ww}. Also, the ranges of streamwise and spanwise wave numbers where meaningful spectra levels can be calculated are limited by the sampling frequency and the smallest spanwise probe separation, respectively. Given a sampling frequency of 50 kHz, the maximum measurable frequency, expressed as streamwise wave number, is $K_x c$ = 1227. Based on the smallest probe separation, which was Δy_{min} = .0157c in this case, the maximum measurable spanwise wave number is $k_y c$ = 200.

Looking at the u – component spectrum for location A/L1 in figure 3.13, the differences between the streamwise and spanwise length scales are immediately apparent. The horizontal elongation of the spectral peak near $K_x c$ = 0, indicates a spanwise length scale much smaller than the streamwise length scale. This is the same difference in length scales that can be seen in the correlation function for this measurement (figure 3.9A). The elongation is also present in the v and w – components. However, these spectra show distinct peaks associated with the passage frequency of the large turbulent eddies. The peak in the upwash (w – component) spectrum is centered on the $K_x c$ axis at $K_x c$ = 20, the same frequency as the peak in the w autospectrum at point A (figure 3.4). Considering the mean flow speed, and assuming Taylor's Hypothesis, the peak streamwise wave number of $K_x c$ = 20 implies a turbulent eddy spacing of ~0.3c. The peak in the v – component spectrum lies left of center at $k_y c \approx$ -25, because of a phase lag between point A and the other points along L1. This corresponds to the skewing noted above in the correlation function (figure 3.9B).

Most interesting, from an aeroacoustic standpoint, is the spectrum for the upwash component. Comparing the spectrum shown in figure 3.13 to the von Kármán isotropic turbulence spectrum shown in figure 3.6, the most apparent difference is the lack of isotropy in the measured spectrum. The semicircular contours associated with isotropic turbulence are simply not present. Even at higher wave numbers, the contours in the measured spectra remain elongated in the spanwise direction, suggesting that the smaller scale turbulent motions tend to be organized by the anisotropy of the large eddies or that the nonsinusoidal components of those eddies contribute substantially to the spectrum at higher wave numbers. Not only is anisotropy apparent in the spectrum for each velocity component, the fact that those spectra are different also points to anisotropy.

Thus, it can be seen that the idealized von Kármán spectrum does not accurately represent the wave number frequency spectrum of this flow. Indeed, anisotropy due to large scale coherent turbulence is present in many common flows, particularly wakes. Therefore, the von Kármán spectrum should not be expected to be generally representative of wave number frequency spectra of typical flows.

Figure 3.14 shows the wave number frequency spectra for two-point profile B/L2. As noted for the corresponding correlation plot (figure 3.10), the *u* – component at B/L2 seems more isotropic as compared to the *u* – component at A/L1, although there is still some spanwise elongation of the contours, particularly at higher frequencies. The *v* and *w* – components are similar to those for profile A/L1, however, some differences due to the stretching of the turbulence at this location are noticeable. The peak spectral levels are higher, because the stretching is organizing and intensifying the spanwise turbulent eddies. The stretching also increases the spanwise length scales, as was noted in the corresponding correlation plots. Thus, the contours are less elliptical as compared to those in figures 3.13B and 3.13C, producing contours at higher wave numbers that are slightly more isotropic.

The wave number frequency spectra for two-point profile C/L3 are shown in figure 3.15. In this region of high curvature and axial velocity gradients, the spectrum for the *u* – component is remarkably lopsided, with the main peak lying left of center at $k_y c \approx 50$. The *v* and w – components, however, appear much more similar to those of the other measurements. They both display a peak at $K_x c \approx 20$, albeit the peaks are weaker, and the decay at higher wave numbers is slower. The decay occurs at roughly the same rates in both the spanwise and streamwise wave numbers, resulting in spectra that seem much more isotropic. Conceivably, the stretching, skewing, and curvature experienced by the flow at this location break up the large scale coherent motions, thus releasing their influence over the small scale turbulence and creating a more isotropic flow. However, it is still clear that the spectrum does not resemble the von Kármán isotropic spectrum, in that the contours are centered on the peak and not on the origin. Such a shift in the origin of a spectrum could be produced by modulation of the smaller structures in the time-space domain by the dominant large-scale eddies.

The final spectra, those taken with the fixed probe located in the vortex core, are shown in figure 3.16. The spectra for this profile are dominated by the low frequency motions associated with vortex wandering. The u – component has a region of negative correlation a low streamwise and spanwise wave numbers. The v and w – components both have contours that are almost parallel to the k_y axis, and peak values at the lowest streamwise wave numbers (lowest frequencies). The valley on the K_x axis in the spectrum for the w – component is presumed to be an effect of the core motions resulting from buffeting of the core by the surrounding turbulence.

3.4.4. Length Scales

As compact characterizations of the wave number frequency spectra, the correlation length scales as functions of frequency were calculated for two-point profiles A/L1, B/L2, and C/L3. These correlation length scales are shown in figure 3.17 along with that calculated from the von Kármán isotropic spectrum. The correlation length scales of the measured spectra are nondimensionalized by the local half-width of the wake, L, given in table 3.1. The frequency is expressed in terms of streamwise wave numbers ($K_x = \omega/U_\infty$) and nondimensionalized using $k_e = \left(\frac{\Gamma\left(\frac{5}{6}\right)}{\Gamma\left(\frac{1}{3}\right)}\right)\left(\frac{\sqrt{p}}{L}\right)$. To nondimensionalize $l_y(\omega)$ based on the von Kármán isotropic spectrum, the integral length scale (equation 3.13) was used.

Significant differences are apparent between the measured correlation length scales and that based on the von Kármán isotropic spectrum. Namely, at lower frequencies, the measured length scales are dominated by the influence of the quasiperiodic large-scale eddies, which produce much more pronounced peaks as compared to the that based on the von Kármán isotropic spectrum. However, the spectra are similar in that they all decay with a slope of -1 on the log-log scale at higher normalized frequencies ($K_x/k_e > 4$).

Some of the quantitative differences in the correlation length scales may be due to the nondimensionalizing length, L. Ideally, the measured correlation length scales would be nondimensionalized using the integral length scale as was done for the von Kármán

correlation length. However, the anisotropy of the measured turbulence makes this virtually impossible.

The streamwise length scale of the streamwise velocity component is defined as,

$$L_{u,x} = U_\infty \int R_{uu}(t)dt \tag{3.13}$$

where R_{uu} is the autocorrelation coefficient function. For time delay correlations, the definition is Likewise, the spanwise length scale of the streamwise component is defined by,

$$L_{u,y} = \int R_{uu}(\Delta y)d\Delta y, \tag{3.14}$$

where $R_{uu}(\Delta y)$ is the cross correlation between two-point measurements. For homogenous, isotropic turbulence this length scale is $0.5L_{u,x}$ (Hinze, 1975). Analogously, the streamwise length scale of the upwash velocity component, $L_{w,x}$, and the spanwise length scale of that component, $L_{w,y}$, can also be calculated. Both of these length scales will also be $.5L_{u,x}$ for homogenous, isotropic turbulence.

Isotropic turbulence, by definition, is the same in every direction, therefore only one of these length scales is needed to characterize the scale of the turbulence. For the measured turbulence, however, these equations do not provide consistent length scales. Indeed, one gets different values for each length scale. The values of the length scales of the measured turbulence as calculated for the four locations in the present flow are listed in table 3.1. The streamwise length scales of the upwash component, calculated in this manner, are smaller than the spanwise length scales. This clearly contradicts what the wave number frequency spectra show, namely, that the spanwise length scale is smaller than the streamwise length scale. This contradiction is due to large scale quasi-periodic eddies that introduce negative areas into $R_{ww}(x)$, which significantly reduce the value calculated for the streamwise length scale of the upwash component.

A length that is not dependent on direction, yet characteristic of the turbulence size is the half wake width (table 3.1). For lack of a better, statistically defined, length scale, this value will be used for normalizing the broadband noise calculations. This value also has the added advantage of being easy to measure.

Table 3.1. Comparison of different possible methods of calculating the length scales. The length scales are in mm.

	A/L1	B/L2	C/L3
Method 1 - Integrating R_{uu} and R_{ww}			
$L_{u,x}$	10.6	7.7	5.5
$L_{w,x}$	2.8	2.7	2.0
$L_{w,y}$	9.8	15.0	7.9
Method 3 - Using the half wake width			
L	**16.9**	**12.2**	**6.7**

3.4.5. Aeroacoustic Implications

The upwash wave number frequency spectra for two-point profiles A/L1 and B/L2 can be used to examine the aeroacoustic implications of the above results for the broadband noise radiated from an airfoil in a turbulent flow. The spectra from these profiles are used, because the flow at these locations is spanwise homogeneous, which means that the measured wave number frequency spectra give direct estimations of the full spectra as discussed in Section 3.5.1.

Amiet considered the simplification to his definition of the far-field acoustic power spectral density produced by an airfoil in a turbulent flow (equation 3.1), where the cross spectrum, $G_{ii}(y,\Delta y,w)$, decays fast enough that $\Phi_{ww}(K_x,k_y)$ can be replaced by $\Phi_{ww}(K_x,0)$. Amiet's simplification is examined by comparing $\Phi_{ww}(K_x,K_x)$ and $\Phi_{ww}(K_x,0)$ for the measured spectra and for the von Kármán isotropic spectrum (figure 3.18). For the measured spectra, a the spectral peaks for $\Phi_{ww}(K_x,0)$ occur at lower frequencies than for $\Phi_{ww}(K_x,K_x)$. Also, the peaks levels for $\Phi_{ww}(K_x,K_x)$ are about 4 dB lower than for $\Phi_{ww}(K_x,0)$. The von Kármán spectrum experiences smaller differences in peak frequencies and no differences in the peak level. Despite, the differences between $\Phi_{ww}(K_x,0)$ and $\Phi_{ww}(K_x,K_x)$ for the measured spectra, the basic shapes are similar enough that Amiet's simplification is considered to be reasonable for this case.

As noted above, during the discussion of the wave number frequency spectra, the von Kármán isotropic spectrum, which is often used in aeroacoustic calculations, is quite dissimilar from the measured spectra of the upwash component. Comparisons of

aeroacoustic calculations, such as directionality, using both the measured wave number frequency spectra and the von Kármán spectra can be made to judge the usefulness of the von Kármán spectrum for noise prediction.

Directionality is the sound pressure levels over a semi-circular arc directly above a semi-infinite flat plate. As defined in Devenport *et al*. (1998) directionality is calculated using the expression

$$D(q) = 10 \log_{10} \left[\frac{S_{pp}(0, y, z, w)}{S_{pp}(0,0, z, w)} \right] \tag{3.15}$$

where $\sin q = \frac{yb}{s}$.

Figure 3.19 shows the directionality using both the von Kármán spectrum and the measured spectra. The directionality is calculated at two different frequencies for a hypothetical blade Mach number of 0.7, typical of helicopter rotors. At the lower frequency, $K_x c \approx 15$, the directionality calculated with the von Kármán spectrum shows more variation than those calculated with the measured spectra. For the higher frequency, $K_x c \approx 65$, the directionality based on the von Kármán spectrum shows even more variation with respect to θ. However, the directionalities calculated with the measured spectra change only slightly and remain relatively invariant at lower angles.

The reason for this invariance can be seen by referring back to the upwash wave number frequency spectra for profiles A/L1 and B/L2 shown in figures 3.13C and 3.14C. The relative differences in the streamwise and spanwise length scales cause the spectra to be almost constant with respect to k_y for values much less than K_x. What variation in directionality exists is due largely to the blade response function and the dipole directivity. Interestingly, this further justifies Amiet's approximation, where he replaces $\Phi_{ww}(K_x, k_y)$ with $\Phi_{ww}(K_x, 0)$.

In light of the significant differences in aeroacoustic results produced using the von Kármán spectrum and the real spectra, it is concluded that the von Kármán spectrum does not serve as an adequate model of real spectra. If accurate broadband noise predictions are to be performed, new models of real wave number frequency spectra will need to be developed.

It is possible to adjust the von Kármán wave number frequency spectrum so that it

produces directionality calculations that more closely match those based on measured spectra. To do this the streamwise and spanwise length scales of the von Kármán spectrum can be changed to match those of the measured spectra. Since, there is no reliable method of calculating the length scales, and since the goal is for the von Kármán spectrum to more closely match the measured spectra, the ratio of the length scales was found by taking the ratio of the k_y and K_x axes of the elliptical peaks in the measured spectra. These ratios are then taken to be the ratios of the streamwise to spanwise length scales. Table 3.2 lists the ratios for several contour levels and shows the final chosen values. The von Kármán spectrum with the adjusted length scales is shown in figure 3.20.

Table 3.2. Ratios of major to minor axes for several contour levels on the measured spectra. The average values are used to adjust the length scales of the von Kármán spectra for broadband noise calculations.

	Ratio of major to minor axes	
Contour	A/L1	B/L2
2.40e-4	3.75	2.10
1.08e-4	3.0	2.67
4.89e-5	3.78	3.10
Average	**3.51**	**2.62**

Directionality plots are again shown for $K_xc \approx 15$ and $K_xc \approx 65$ (figures 3.21 and 3.22, respectively). In these plots, the measured directionality curves are compared to the directionality curves based on the adjusted von Kármán spectra and the normal von Kármán spectrum. It is quite clear that the adjusted von Kármán spectra produce directionality curves that much more closely match the measured directionality curves. While these results are specific to the measured flow, they do illustrate the fact that the isotropic turbulence models, which have traditionally been used to make noise predictions, can be improved by taking into consideration the anisotropy inherent in real flows.

Finally, it should be noted that adjusting the length scales of the von Kármán spectrum does not change the fact that it is not the same magnitude as the measured spectra. This means that the adjusted von Kármán spectrum will not properly predict the magnitude of the far field noise levels. Further developments in modeling wave number

frequency spectra are necessary in order to achieve such a level of prediction.

3.5. Conclusions

Four sets of two-point measurements were made in the lifting wake of a NACA 0012 half-wing, from which space-time cross-correlation functions were calculated. These correlation functions produced information concerning turbulence length scales at two locations within the two-dimensional flow region of the wake, and two locations within the tip vortex.

Wave number frequency spectra were then calculated by double Fourier transforming the correlation functions. These spectra were compared to the von Kármán spectrum, and it was concluded that the streamwise and spanwise length scales of the measured spectra were not equal due to the anisotropy of the flow.

Comparisons of aeroacoustic calculations based on the upwash spectra from the two profiles located in the homogeneous flow region of the wake and the von Kármán spectrum showed that the von Kármán spectrum does not produce results matching those based on the measured spectra. However, it was found that Amiet's approximation that the spectra, $\Phi_{ww}(K_x, k_y)$, can be replaced by $\Phi_{ww}(K_x, 0)$, is even more accurate for measured spectra than for the von Kármán spectrum. This is because of the smaller spanwise length scales relative to the streamwise length scales.

The ratios of the length scales were determined from the ratios of the major and minor axes of the elliptical contours on the measured wave number frequency spectra. The von Kármán spectrum was then adjusted so that it’s length scales matched those of the measured spectra. The adjusted von Kármán spectra resulted in broadband noise calculations that matched the measured data much better than the calculations based on the normal von Kármán spectrum. These results indicate that it is necessary to consider the anisotropy in real flows, if accurate broadband noise predictions are desired.

CHAPTER 4. ANALYSIS OF TWO-POINT MEASUREMENT IN THE TIP INTERACTION FLOW

4.1. Nomenclature

C_p – pressure coefficient

c – chord length

x, y, z – coordinates describing location within flow

u, v, w – velocity components

f – frequency

ω - angular frequency

U_∞ – free stream velocity

Δy – spanwise probe separation

τ – time delay

i – index, 1 to 3, indicating velocity component

$R_{ii}()$ – space-time correlation function calculated from the ith velocity component

$\phi_{ii}()$ – the 'pointwise' wave number frequency spectrum calculated from the ith velocity fluctuations

K_x – nominal streamwise wave number calculated from angular frequency using Taylor's hypothesis, $K_x = \omega/U_\infty$

k_y – spanwise wave number

$\overline{u^2}, \overline{v^2}, \overline{w^2}$ – variances for the fluctuations of the three velocity components

Ω_x – mean streamwise vorticity

k – turbulence kinetic energy

P – turbulence kinetic energy production

τ_x – axial shear stress

4.2. Introduction

The rotor flows of helicopters are quite complex, being dominated by blade-wake interactions (BWI) that can have significant affects on the fluid dynamics and, hence, the broadband noise. Wittmer and Devenport (1995) and Wittmer and Devenport (1996)

have previously performed measurements in a flow formed by the interaction of a tip vortex with a blade of infinite span. They found that the vortex core becomes much larger and weaker after impinging on the interacting blade. The core also becomes surrounded by a comparatively intense and extensive turbulent region. In another study, Wittmer *et al.* (1995) examined a flow where the tip vortex impinged on an interacting blade approximately one chord length from the tip. They also observed a similar weakening of the vortex core and an intensification and growth of the surrounding turbulent field. In this case, the tip vortex of the interacting blade also affected the impinging vortex by altering the form of the turbulent field and its intensity between the two vortex cores.

In a related study, Devenport *et al*. (1997) took measurements in a flow formed by the interaction of two tip vortices. A grid of single point measurements were taken, as well as five two-sided profiles of two-point measurements were taken in the region of vortex interaction. The purpose of this work presented in this chapter is to analyze those two-point measurements in the context of aeroacoustic prediction. To this end, space-time cross correlation functions and wave number frequency spectra are calculated from the two-point profiles, and the aeroacoustic implications of the spectra are examined.

4.3. Description of Devenport *et al.*'s (1997) Experiment and Single-Point Results

4.3.1. Experimental Setup

Devenport *et al.*'s (1997) tip interaction measurements were made in the Virginia Tech Stability Wind Tunnel shown in figure 4.1. This tunnel, powered by a 600 horsepower axial fan, is a closed circuit facility with a test section of 1.83 m $\times$ 1.83 m cross section and 7.33 m length. The flow through the test section is closely uniform with turbulence intensity less than 0.05% at flow speeds of 20 m/s. Boundary layer growth at the walls causes a slight pressure gradient of $\partial C_p/\partial x$ = -.003 /m.

Two NACA 0012 airfoils of chord .203 m were used in the setup depicted in figure 4.2. Both were set at a 5° angle of attack. Boundary layer trips made of 0.5 mm glass beads were glued on both blades along the entire span between the 20% and 40% chord locations. The upstream blade was mounted vertically to the upper wall in a half-wing configuration with 0.879 m extending into the flow. The downstream blade was

also mounted to the upper wall 14 chordlengths downstream of the generator blade (upstream blade). Using helium bubble flow visualization to determine the path of the vortex core of the generator tip vortex core, the downstream interaction blade was positioned so that the vortex core passed a distance of 0.3*c* to the suction side of the interaction blade tip. The mutual induction of the two tip vortices caused them to rotate one about each other over the 15*c* distance from the downstream blade to the measurement location.

To perform the two-point measurements, the two probe sting, shown in figure 4.3, was mounted on a computerized y-z traverse. The probe sting itself has another small computerized traverse, which allows the separation of the two probes to be varied. The probe mount closest to the sting is fixed, but the position of the other probe mount may be varied with respect to the sting with an accuracy of about 1.0 mm. The probes were mounted in the holder such that they angled approximately 2° toward each other, so that the probe tips could be positioned as close to each other as possible without experiencing significant interference from each other.

4.3.2. Single-point Results

Single point hot-wire measurements were taken by Devenport *et al.* (1997) 15*c* downstream of the interaction blade in order to document the cross-sectional turbulence structure of the flowfield. This section reviews their main observations and results. The origin of the coordinate system they used is located at the same downstream location as the generator blade leading edge. As shown in figure 4.2, the *x*, *u* direction is pointed downstream, the *y*, *v* direction is pointed away from the tips of the blades, and the *z*, *w* direction is pointed such that it completes the right handed coordinate system.

Figures 4.4 - 4.11 show mean cross flow velocity vectors, mean axial velocity deficit, mean streamwise vorticity, axial normal turbulence stress, summed cross flow normal turbulence stresses, turbulence kinetic energy, turbulence kinetic energy production, and axial shear stress magnitude, respectively. The approximate core edges are shown in some of the figures using circles. Figure 4.6 indicates using labels that the upper core originates from the generator blade and the lower core originates from the interaction blade.

The distance between the two vortex cores, 0.225*c*, is slightly less than the nominal generator vortex/interaction blade tip distance of 0.3*c*, which suggests that the cores are slowly approaching each other. The two cores are surrounded by the merged turbulent spiral wake of the individual vortices, almost forming a single spiral at farther distances from the cores. Interestingly, there is a region of low turbulence to the right of the cores, that seems to be free stream fluid that was trapped between the two wakes.

Between the two vortex cores, there are particularly high levels of turbulence kinetic energy as shown in figure 4.9. In this region, the combined mean velocity fields produce high mean strain rates that tend to organize and intensify turbulent structures with axes roughly parallel to a line joining the core centers. Autospectra, shown in figure 4.12, of the *v* and *w*- velocity fluctuations at point D (figure 4.9) between the cores provides further evidence of such eddy organization. There is a strong peak in the *v* - autospectra at a normalized frequency of $fc/U_\infty = 3$, which implies a streamwise spacing of .33*c*. The corresponding peak in the *w* – autospectra is much weaker, indicating that the turbulent eddies may be organized more with their rotational axes in roughly the *v* - direction, which is closer to the direction of the line between the two cores.

Vortex wandering contributes approximately 30% to $\overline{u^2}$ in the generator vortex. Wandering contributions to the turbulent kinetic energy are significant (>30%) in both vortex cores. Mean velocity profiles measured through the generator vortex core is shown in figure 4.13 and that measured through the interaction vortex core is shown in figure 4.14. Velocity fluctuations in the vortex core may also be inactive motions generated in the core as it is buffeted by the surrounding turbulence (Devenport *et al*., 1997). This effect is subtler compared to wandering, and as such, there is no way of filtering it out. Autospectra of the upwash velocity fluctuations taken along a radial profile at $z/c = 0$ from $y/c = 0.4$ to $y/c = -0.1$ at the locations shown in figure 4.7 are shown in figure 4.15. Far from the core, they have forms typical for turbulent wakes (for example Wygnanski *et al*., 1986). At points nearer to the cores, spectral levels increase at all frequencies. The increases at normalized frequencies less than 20 are the likely effects of wandering and buffeting. However, the spectral levels at higher frequencies are almost certainly due to true small scale turbulence. The high spectral levels at high frequencies suggest that the vortex cores are turbulent. Similar increases in core

turbulence levels downstream of a vortex/infinite span blade interaction were also found by Wittmer and Devenport (1996) and Wittmer (1996).

4.3.3. Two-point Data Acquisition

Devenport *et al*. (1997) took five two-sided, two-point spanwise profiles through the region of core interaction as shown in figure 4.9. These profiles were designed to reveal the flow as seen by a hypothetical blade intersecting it at different elevations. The solid black dots indicate the fixed probe locations. For each profile, the movable probe was used for measurements at positive and negative probe separations along the lines extending to the left and right of the fixed probe locations. Profile C1 is above the generator core, with the fixed probe located in the region of turbulence surrounding it. Profile C2 passes through the generator vortex core, with the fixed probe located at the center of the core. Profile C3 has a fixed probe location in between the two vortex cores. Profile C4 passes through the interaction vortex core, with the fixed probe located at the center of the core. Finally, profile C5 is below the interaction core, with the fixed probe located in the region of intense turbulence surrounding the interaction core. The analysis of these two-point profiles is the subject of this chapter.

The two probes were angled toward each other by about 2° each, which allowed a minimum probe separation of 2.5m (0.0125c) without prohibitive probe interference. The maximum probe separation for each profile was 0.75c for both negative and positive separations. A total of 94 separations were measured in each profile. Each two-point measurement consisted of 100 blocks of 3072 point records taken at a sampling frequency of 50k over a total time of approximately one minute.

4.4. Two-point Results and Discussion

4.4.1. Data Analysis

Because the two-point profiles taken by Devenport *et al*. (1997) are in the spanwise direction, the data analysis techniques used are identical to those used for Miranda's (1996) data in chapter 3, with one exception. The profiles, in this case, are two-sided instead of one-sided, meaning that simultaneous two-point data was taken for both positive and negative probe separations. Therefore, the cross-spectral densities are

not exactly symmetrical about the zero probe separation axis. When the FFT with respect to spanwise probe separation in equation 3.3 is then performed, the results will have non-zero complex components.

4.4.2. Space-time Cross Correlation Functions

The normal components of the correlation function, $R_{ii}(y,\Delta y,z,0,\tau)$, for profile C3 are shown in figure 4.16. The correlation functions are plotted against $\Delta y/c$ and $\tau U_\infty/c$. Assuming Taylor's hypothesis, τU_∞ represents distance in the streamwise direction. As with all correlation plots in this work, these are normalized by the variance of the turbulent fluctuations in the corresponding velocity component at the fixed probe location. The estimated uncertainties for the correlation plots calculated in this flow are ± 0.04 for R_{uu}, R_{vv}, and R_{ww}. All correlation levels with magnitudes less than the uncertainty have been left out of the plots.

For the profile, centered between the vortex cores, the v - component fluctuations show the most significant correlation. Significant correlations extend to $\pm 0.2c$ in $\tau U_\infty/c$ (the streamwise direction) and $\pm 0.1c$ in the spanwise direction. This range of spanwise positions corresponds approximately to the size of the region of intense turbulence formed between the two vortex cores as shown in the figure 4.9. Thus, the fluctuations between the vortices appear not to be correlated with the turbulence in the outer surrounding spiral wake. This is not surprising, considering that regions of relatively low turbulence, thought to be freestream flow (Devenport *et al*., 1997), lie between the vortex cores and the outer spiral turbulence.

As noted earlier, the region between the vortex cores experiences stretching, which tends to organize the turbulent eddies in the direction of a line connecting the two cores. This hypothesis is further supported by the periodicity shown by the v - component correlations in figure 4.16B. The regions of significant negative correlation in the positive and negative streamwise directions suggest the presence of organized quasi-periodic eddies. The regions of negative correlation extend to $\sim 0.2c$, which can be considered to be the eddy spacing, if Talyor's Hypothesis is assumed. This is roughly equal to the distance between the two vortex cores.

Figure 4.17 shows the normal components of the correlation function at the center of the interaction blade vortex core (profile C4). The most significant feature of the correlation function at this location is the long streamwise length scales, which are associated with the low frequency motions of vortex wandering. In the streamwise direction, the correlations extend to ~0.4*c*. In the spanwise direction, the correlations reach to ~0.2*c*, as indicated by the flanking regions of negative correlation seen for the *w* - component fluctuations. This is much larger than the diameter of the vortex core, which suggests that wandering is coherent over a substantial cross section of the surrounding flow as assumed by Devenport *et al*. (1997).

The normal components of the correlation function for profile C5, located below the interaction vortex core, are shown in figure 4.18. The correlation function at this location also shows signs of the wandering, especially in the *v* - component where streamwise length scales reach to ~±0.4*c*. In the *w* - component, there are significant negative correlations suggesting periodicity. This could be a result of roughly *z* - wise aligned eddies, which would be expected at the locations where the spiral wake is cut by profile C5. The streamwise and spanwise length scales of these eddies are roughly the same as those for the turbulent eddies in the region between the two vortex cores.

The correlation function for profile C1, located above the generator vortex core, shown in figure 4.19, is very similar to that for profile C5. The wandering of the generator vortex core is apparent, although less significant, in the *v* - component, and the organized periodicity is also apparent in the *w* - component. All associated length scales correspond to their counterparts in the correlation function for profile C5.

Figure 4.20 shows the correlation function for profile C2, whose fixed probe location is at the generator vortex center. Being located in the vortex core, the correlation function bears close resemblance to that for profile C4, whose fixed probe location is at the interaction vortex center. The correlations are dominated by the low frequency wandering motions of the vortex, as indicated by the large length scales in the streamwise (time delay) direction. As was true for profile C4, the *w* - component correlations show coherent wandering motions over a cross sectional area that extends beyond the boundaries of the vortex core and into the surrounding spiral wake.

Integral length scales, as defined in equations 3.10 and 3.11, were calculated from the space-time correlations. Table 4.1 shows the various values. The length scales were calculated using two different methods. The first method involves taking the integral over the entire possible range of time delays or probe separations. However, as noted in Chapter 3, results using this method are often unreliable due to the regions of negative correlations. Therefore, the second method used here involves setting the limits of integration to the location of the first zero crossing in the correlation function. In general, the integral lengths scales vary widely. This is an indication of the extent of the anisotropy present in the turbulence. The second method usually resulted in slightly higher length scales as would be expected since none of the negative correlations were integrated. However, the length scales produced with this method are no more consistent with each other than those produced using the first method.

Table 4.1 Integral Length scales in mm.

Method One - Full Integral					
Point	A	B	D	E	F
$L_{u,x}$	6.6	14.8	2.8	18.9	8.6
$L_{u,y}$	1.2	1.2	0.73	2.3	9.0
$L_{v,x}$	16.7	34.8	3.3	18.6	25.4
$L_{v,y}$	12.3	12.3	7.3	9.0	9.2
$L_{w,x}$	3.5	44.6	4.4	38.8	4.9
$L_{w,y}$	1.4	1.4	4.0	2.4	9.4
Method Two - Integrate to First Negative Correlation					
$L_{u,x}$	8.2	14.8	2.7	18.9	9.6
$L_{u,y}$	3.3	3.3	1.8	3.5	9.8
$L_{v,x}$	18.9	34.8	3.4	18.6	25.4
$L_{v,y}$	12.3	12.3	7.3	9.0	10.6
$L_{w,x}$	5.2	44.6	3.0	38.8	5.9
$L_{w,y}$	5.0	5.0	4.3	5.4	10.1

4.4.3. Wave Number Frequency Spectra

The wave number frequency spectra, calculated from the correlation functions presented above, are shown in figures 4.21 - 4.35. Because these measurements are double sided, there is a non-zero imaginary component for each wave number frequency spectrum. This imaginary component is also presented along with the real component for each spectrum. The spectra are plotted against frequency expressed as streamwise wave

number, K_xc, by assuming Taylor's hypothesis and spanwise wave number, k_yc. The spectral levels have also been normalized by the mean square fluctuation of the relevant velocity component at the fixed probe location, so that each real spectrum integrates to unity and each imaginary spectrum integrates to zero.

Uncertainty estimates for the wave number frequency spectra calculated in this flow are ±12% for ϕ_{uu} and ±14% for ϕ_{vv} and ϕ_{ww}. Given a sample frequency of 50 kHz, the maximum measurable frequency, expressed as streamwise wave number, is K_xc = 1227. The smallest probe separation, $\Delta y_{min} = .0125c$ in this case, decides the maximum measurable spanwise wave number, which is $k_yc \approx 200$.

The spectra for profile C3, which passes between the two vortex cores are shown in figures 4.21 - 4.23. The real parts of the spectra for the *v* - and *w* - components have the same general form as the spectra presented above for the two-dimensional tip vortex wake. These spectra have peaks at small K_xc and k_yc, and they decay at high wave numbers in both directions. As was noted in the corresponding correlation plots (figure 4.16), the spanwise length scales at this location are smaller than the streamwise length scales. This results in spanwise elongation of the contours in the wave number frequency spectra. The same result was also found in the two-dimensional tip vortex wake.

The peaks in the real *v* - and *w* - component spectra lie at approximately the same wave numbers, $K_xc = 20$ and $k_yc = 0$, as the peaks in the upwash spectra for the two-dimensional tip vortex wake. This peak corresponds to the peak in the autospectra for point D (figure 4.12) at frequency $fc/U_\infty = 3$. This peak is thought to be produced by quasi-periodic, turbulent eddies. Thus, the peak in the *v* - component spectrum is stronger, because, as noted earlier, the stretching in this region organizes the eddies in roughly the *v* direction. The fact that the peaks are centered on $k_yc = 0$ means that on average the velocity fluctuation are impacting on all the points in profile C3 simultaneously. Also, the fact that the imaginary parts of these spectra are relatively small indicates that the *v* - and *w*- component fluctuations are symmetric about point D.

In the real part of the *w* - component spectrum, there are two smaller peaks at the smallest streamwise wave number and $k_yc = \pm 30$. These low frequency peaks are probably caused by vortex wandering, and the spanwise wave numbers, $k_yc = \pm 30$, are

consistent with the conclusion that the wandering motions are coherent over a length scale of ~0.2c.

The real part of the u - component spectrum has a negative region at the same wave numbers where the peaks are located in the v - and w - component spectra. As a result, the energy in this spectrum is spread out into the higher spanwise wave numbers. Thus, the estimated spanwise length scale is much smaller than that for the v - and w - components. This is likely another result of the organization in the v - direction of the turbulent eddies, which would cause the length scales in the v - direction to increase and the other length scales to decrease.

The imaginary part of this spectrum shows two strong antisymmetric lobes centered roughly at $K_x c = 20$, which corresponds to the preferred passage frequency of the turbulent eddies. The fact that the imaginary part is large and antisymmetric indicates that the u - component fluctuations are asymmetric about the point D.

Looking next at the spectra calculated for profiles C4 (figures 4.24 - 4.26) and C2 (figures 4.33 - 4.35), which pass through the vortex cores, it can be seen that both sets of spectra show very similar features. The real components of both sets of spectra display intense elongation in the spanwise wave number direction, with most of the energy located at the smallest streamwise wave numbers (lowest frequencies). This is the result of the low frequency, small spanwise length scale wandering of the vortex cores.

However, evidence of other inactive core motions is also present. There are secondary peaks in the real parts of the u - and v - component spectra, which occur at frequencies, $K_x c = 20$, corresponding to the peaks in the spectra for profile C3. This suggests that some core fluctuations are being caused by buffeting by turbulent structures in the surrounding wake.

Another explanation is that the surrounding turbulent structures are creating axisymmetric core waves (Devenport *et al.*, 1997). This is perhaps more likely considering the form of the correlation function for the u - component (figure 4.17A). In the correlation plot, there are small regions of negative correlation to the left and right of the center at $\Delta y = \pm 0.1c$. This spanwise distance is roughly the same as the core radii. Thus, there are in-phase velocity fluctuations near the core center, and out-of-phase fluctuations around the edges of the core, such as would be expected in the presence of

axisymmetric core waves (Devenport *et al*., 1997). This length scale, 0.1*c*, corresponds to the spanwise wave numbers, $k_y c = \pm 80$, at which the secondary peaks are located in the *u* - component spectrum.

The wave number frequency spectra for profiles C3, C4 and C2 provide information concerning vortex wandering that is not available using single probe methods. Vortex wandering is characterized by low frequency motions of small spanwise extent. In this case the, the amount of energy contributable to wandering is easily determined by looking at the wave number frequency spectra. The energy due to wandering is distinctly seen as elongated peaks at the lowest streamwise wave numbers. Because the effects of wandering can be so easily distinguished in these spectra, the energy of the wandering fluctuations can be filtered out by ignoring the low frequencies associated with wandering. Looking at the spectra, wandering is dominant at frequencies less than about $K_x c = 9$ ($fc/U_\infty = 1.4$), but is absent at higher frequencies. Because the spectra are normalized to integrate to one, the volume under the spectra in the frequencies associated with wandering can be taken as an estimate of the percentage of energy (or turbulence stress) due to wandering. Performing this calculation shows that the percentage of turbulence stress, $\overline{w^2}$, due to wandering at point D, between the vortices, is ~12%. In the vortex cores themselves (points B and E), the percentage is much larger, ~66%.

Considering these percentages, Devenport *et al*. (1997) estimated that wandering motions account for no greater than $0.5\%U_\infty$ and $0.7\%U_\infty$ of the tangential and axial velocity profiles for the generator vortex core and $0.2\%U_\infty$ and $0.3\%U_\infty$ for the interaction vortex core. Using the formulation of Devenport *et al*. (1996), these effects were corrected for. The corrected core parameters for the generator vortex are: core radius of $0.049c$; peak tangential velocity of $0.215U_\infty$; and centerline axial velocity deficit of $0.147U_\infty$. The same corrected parameters for the interaction vortex core are: radius of 0.074c; peak tangential velocity of $0.132U_\infty$; and centerline axial velocity deficit of $0.103U_\infty$. It was found that the interaction vortex core was weaker than the other, because the generator vortex effectively reduces the angle of attack of the interaction blade inboard of its tip, thus reducing the amount of vorticity shed near the tip.

Looking, finally, at the spectra for profile C5 (figures 4.27 - 4.29) and profile C1 (figures 4.30 - 4.32), it can be seen that they are also quite similar to each other. Both upwash (*w* - component) spectra have peaks near $K_x c = 20$ and $k_y c = 0$, and they decay at similar rates. The peaks coincide with the preferred passage frequency of quasi-periodic turbulent eddies as seen earlier in the *v* - component spectrum between the two vortices. The peaks however are not centered about the $k_y c = 0$ axis. The peaks for profile C1 are set slightly to the right, and those for profile C5 are to the left. This indicates that the quasi-periodic turbulence structures are skewed and arrive earlier on the negative side of point A and on the positive side of point F. The skewing could be a result of the clockwise secondary flow field produced by the vortex pair (Devenport, 1997). Interestingly, the spectra for profiles C5 and C1 bear similarities with the two-dimensional wake spectra. This is rather surprising, since the spiral wake at these locations is highly curved and strained.

4.4.4. Aeroacoustic Implications

Due to the inhomogenous nature of the flow in the tip interaction region, it is not possible to regard the point-wise wave number frequency spectra calculated here as representative of the full wave number frequency spectra. Therefore, specific aeroacoustic calculations cannot be made using these spectra, as was done with the spectra from the two-dimensional tip vortex wake. However, some general conclusions of aeroacoustic value can still be made concerning these spectra.

Most significantly, none of the spectra presented here resemble the von Kármán spectrum (figure 3.6), which is often used generically in aeroacoustic calculations. The spectra shown here are dominated by inhomogeneity and anisotropy. However, the spectra for profiles C3, C5 and C1 do bear resemblance to the spectra from the two-dimensional tip vortex wake, even though the conditions in the two flows are quite different. This suggests that the spectra are somewhat insensitive to local conditions, which could be valuable information to future modelers.

Also, the spectra presented in this section have spanwise length scales, which are smaller than the streamwise length scales, as was also true for the spectra from the two-dimensional wake. The resulting elongation of the spectra in the spanwise wave number

direction means that Amiet's simplification, in which the wave number frequency spectrum may be replaced by the correlation length scale, is applicable. The upwash correlation length scales for profiles C1 - C5 are presented in figure 4.36. The correlation length scales are equivalent to the $k_y c = 0$ axis of the wave number frequency spectra. For profiles C1 and C5, which are located in similar regions in the flow, two peaks can be seen, one at $K_x c = 6$ and the other at $K_x c = 20$. The second peak is associated with the preferred passage frequency of the coherent turbulence structures. The correlation length scale for profile C3 shows one peak at $K_x c = 6$. The other to profiles C2 and C4, located in the vortex cores, are dominated by wandering, and as such, the correlation scales show the most energy at the lowest streamwise wave numbers.

4.5. Conclusions

Five sets of two-point four-sensor hot-wire measurements taken by Devenport *et al*. (1997) downstream of an interaction between a tip vortex and the tip of a lifting blade were analyzed in the context of aeroacoustics to provide information useful for noise prediction in helicopter rotor flows and other vortex dominated turbulent flows. Devenport *et al*. (1997) took two-point measurements in spanwise profiles with both positive and negative probe separations, in order to examine the turbulence as it would be seen by a hypothetical noise producing airfoil passing through the flow. Two of the profiles were located with the fixed probe in the vortex core centers, one was located with the fixed probe between the two cores, and the other two were located above and below the cores in the surrounding spiral wake. To analyze these two-point measurements, the cross correlation function and wave number frequency spectra were calculated at the five locations in the region of vortex interaction.

The correlation functions and wave number frequency spectra provide information concerning the length scales of the turbulence in the interaction region of the flow. Wandering significantly influences the measurements taken in the vortex cores. Because of the low frequencies and small spanwise length scales of the wandering motions, their influence can be clearly distinguished in the wave number frequency spectra. In the region of intense turbulence between the vortices and in the surrounding

spiral wake, there is strong evidence of coherent turbulent structures with an average eddy spacing of 0.2c, which is approximately the distance between the two vortices.

The coherent turbulent eddies are highly anisotropic, and hence, the wave number frequency spectra are very dissimilar to the isotropic von Kármán wave number frequency spectrum, which has been commonly used in aeroacoustic calculations. However, the spectra from the regions outside of the vortex cores, do bear some resemblance to the spectra calculated from two-point measurements taken in the two-dimensional region of the tip vortex wake. There are peaks at the average frequency of eddy passage with decaying spectral levels at higher wave numbers. Also, the spanwise length scales are smaller than the streamwise length scales, resulting in spectra that are elongated in the spanwise wave number direction. Because the spectra vary slowly in the spanwise direction compared to the streamwise direction, Amiet's simplification holds, and the wave number frequency spectra can be reasonably represented by the correlation length scale calculated according to equation 3.9, which is the $k_y c = 0$ axis of the wave number frequency spectra.

CHAPTER 5. ANALYSIS OF TWO-POINT MEASUREMENTS IN THE FAN CASCADE FLOW

5.1. Nomenclature

x, y, z – coordinates describing location within flow

u, v, w – velocity components

c_a – projection of the chord length in the axial direction

ω - angular frequency

U_∞ – flow velocity upstream of cascade

U_e - free stream velocity downstream of cascade, $0.71U_\infty$

y' – radial probe separation

z' - tangential probe separation

τ – time delay

i and k – indices, 1 to 3, indicating velocity component

$G_{ik}()$ – the cross-spectrum tensor between two time dependent velocity signals

T – the duration of a velocity measurement

E[] – the expected value operation

v_i - the velocity component in the ith direction

$R_{ik}()$ – space-time correlation function tensor

$\phi_{ik}()$ – the 'pointwise' wave number frequency spectrum tensor

s – spanwise distance

K_x – nominal streamwise wave number calculated from angular frequency using Taylor's hypothesis, $K_x = \omega/U_\infty$

k_s – spanwise wave number

$j = \sqrt{-1}$

$\overline{u^2}, \overline{v^2}, \overline{w^2}$ – variances for the fluctuations of the three velocity components

$w_r()$ – stator upwash velocity field downstream of the cascade

$w_s()$ – stator upwash velocity at the stator leading edge plane in the stator frame of reference

x_s, y_s, z_s – coordinates describing location within flow using the stator frame of reference

V_s – speed of stators relative to the rotor cascade

x_0 – downstream location of two-point measurements

η - angle of mean flow velocity downstream of the cascade

5.2. Introduction

Tip leakage flow produced by fan blades in large aspect ratio jet engines is a significant source of broadband noise. Noise is produced when the turbulence in the tip leakage vortices and blade wakes impacts upon the stators behind the fan stage. Efforts to reduce this broadband noise have focused largely on developing prediction capabilities, which take into consideration engine configuration and turbulence characteristics. The turbulence characteristics needed include space-time cross correlation functions or wave number frequency spectra. Just as in Chapter 3 and 4, the wave number frequency spectra are unknown for this flow.

To provide information of use to aeroacoustic modelers and designers, a model of a fan wake flow using a linear compressor cascade wind tunnel was built by Muthanna (1998). Two-point measurements taken by Wenger *et al*. (1998) in this flow are here analyzed in a form useful for aeroacoustic purposes. Along with two-point profiles, Wenger *et al*. also took data in a two-point grid, which allows the space-time delay correlations seen in different frames of reference to be estimated. From Wenger *et al*.'s two-point data, pointwise space time correlation functions and wave number frequency spectra were calculated for a wide range of stator configurations.

5.3. Description of Wenger *et al*.'s (1998) Measurements and Single-Point Results

5.3.1. Experimental Setup

Wenger *et al*. (1998) performed single-point and two-point measurements in the Virginia Tech Low Speed Cascade Wind Tunnel shown in figure 5.1. This facility is described in detail by Muthanna *et al*. (1998) and Muthanna (1998). However, the main characteristics will be outlined here to provide a context for the data analysis. The Cascade Wind Tunnel is powered by a 15 hp centrifugal blower, which is connected to

the test section via a settling chamber and a 3.88:1 two-dimensional contraction. The rectangular (12" x 30") test section has a closely uniform flow upstream of the cascade with a 1% cross-sectional variation in velocity and a turbulence intensity of 0.5%. The flow speed before the cascade is 26.4 m/s, which results in a Reynolds number (based on the chord length of .254 m) of 400,000.

The linear compressor cascade is a row of 8 blades with adjustable tip gap. The blades are mounted diagonally across the test section such that the cascade inlet angle is 65.1°. The cascade inlet angle simulates the operating point of the fan stage by producing a velocity component tangential to the fan cascade. In the experimental setup used to produce the data here analyzed the inlet angle of 65.1° produces a simulated fan tip rotation speed of 11.1 m/s.

The test section boundary layers are removed 9.20" (3.88" in the axial[1] or *x* - direction) upstream of the cascade by 1" deep suction slots on the upper and lower endwalls. After the suction slots, the test section height is 10". The new endwall boundary layers are then tripped using 0.38" wide strips of 0.02" diameter glass beads positioned 5.34" (2.25" axially) upstream from the cascade. These boundary layer trips serve to organize the formation of the new endwall boundary layers. The boundary layers in the blade passages were measured and found to be approximately 0.25" thick midway between the blades in the passages between blades 3 - 6. The other passages showed some end effects.

The blades are 10" chord GE rotor B section blades cantilevered from a single welded aluminum superstructure. The tip gaps, set to 0.165", were all adjusted simultaneously by shimming the superstructure. The blades were made from aluminum, milled using a numerically controlled machine and supplied section data. They have a circular arc camber with a metal angle of 30.7° and a maximum thickness of 0.044 chord lengths near the mid chord. According to GE compressor design, they were mounted with a stagger angle of 56.9°, a solidity of 1.076 and an inlet angle of 65.1°. Boundary

[1] The directions referred to as axial, radial, and tangential correspond to the geometry and motion of a rotating fan stage in a high bypass ratio jet engine. The axial direction is perpendicular to the cascade. The radial direction points away from the tips of the blades. The tangential direction completes the right handed system and points in the direction of simulated fan motion.

layer trips made of 0.25" wide strips of 0.02" diameter glass beads are situated on both sides of each blade 1" from the leading edge.

The cascade turns the flow by an angle of 12.6°. Downstream of the cascade, the side tailboards were adjusted to remove any net tangential pressure gradient across the cascade. The flow 10" downstream of the cascade was then measured using single hot-wire anemometry. The flow was found to be closely periodic across the passages between blades 3 - 6. The test section exit is 39" axially downstream of the cascade. Across the exit are screens, which control the back pressure to ensure that the suction slots operate properly.

To take the two-point measurements, Wenger *et al*. (1998) held the fixed probe using a small strut attached to the tunnel floor. The other probe was moved to various locations using a computer controlled traverse, which was situated atop the tunnel with a probe stem reaching down through a slot in the tunnel roof. A diagram of this setup is shown in figure 5.2.

5.3.2. Single-point Results

The single-point measurements taken by Muthanna (1998) in the Cascade Tunnel are here summarized to provide context for the two-point data analysis. The origin of the coordinate system used by Muthanna is located in the plane of the leading edges of the cascade blades. As shown in figures 5.1 and 5.3, the *x* direction corresponds to the axial direction (perpendicular to the cascade), the *y* direction corresponds to the radial direction (away from the tips of the blades), and the *z* direction corresponds to the tangential direction (parallel to the cascade). The *u* direction corresponds to the mean flow direction after the flow is turned by the cascade. The *v* direction corresponds to the radial direction, and the *w* direction completes the right handed system.

Muthanna measured all components of velocity, Reynolds stresses, triple products, and velocity spectra at the 5 downstream locations shown in figure 5.3 (x/c_a = 1.366, 2.062, 2.831, 3.770, and 4.640). The symbol c_a denotes the projection of the chord length of the cascade blades in the axial direction (c_a = 5.46"). For these measurements, the tip gap was set at 0.165".

The mean velocity U/U_∞, mean cross-flow velocity vectors and turbulence kinetic energy for the location x/c_a = 2.831 with a tip gap of 0.165" are shown in figures 5.4 - 5.6. The symbol, U_∞, is used to denote the speed of the flow upstream of the cascade. In these figures, the wakes of blades 4 and 5 and the tip leakage vortex shed by blade 4 can be seen. Away from the endwall, the blade wakes are almost two dimensional, and they grow in a roughly self-similar fashion with distance downstream (Muthanna, 1998). Their axial velocity profiles are near-Gaussian, u^2 profiles are double peaked, and uw profiles are antisymmetric, similar to general two-dimensional wakes (Muthanna, 1998).

Near the endwall (y/c_a = 0), the flow is dominated by the tip leakage vortex. From the mean cross-flow velocity vectors (figure 5.5), the vortex center is seen to be at y/c_a = 0.2, z/c_a = -4.32. Because of the relatively light loading on the blades, the swirling flowfield generated by the tip leakage vortex is fairly weak as can be seen in figure 5.5. However, the streamwise (u) mean velocity deficit is quite large as can be seen in figure 5.4. Peak tangential velocities produced by the vortex are about 4%U_∞, and the peak axial velocity deficit is about 0.24U_∞. Studies done on free vortices by Sreedhar and Ragab (1994) and Ragab (1995) have shown that such a large ratio of axial velocity deficit to peak tangential velocity renders a vortex highly unstable to helical disturbances. The instability results in helical turbulent structures and mixing that act to diffuse the axial velocity deficit.

Contours of turbulence kinetic energy shown in figure 5.6 show that the tip leakage vortex contains high levels of turbulence. The turbulence levels in the vortex are much higher than in the blade wakes. According to the single-point results of Muthanna *et al*. (1998), the vortex turbulence also decays slower, and eventually becomes the dominant source of turbulence. TKE production, shown in figure 5.7, is high in an arc-shaped region above and to the right of the core region. Almost all of this TKE production is a result of mean streamwise velocity gradients (see Muthanna, 1998). The swirling motions cause very little TKE production, which is consistent with the mean velocity measurements and the free vortex analogy.

Autospectra of all three velocity components measured in the wake of blade 4 and in the tip leakage vortex are shown in figure 5.8. The spectra locations are shown by the black dots in figure 5.4. The spectra are normalized by $2\pi U_e c_a$ and plotted against

angular frequency, which is normalized by $\omega c_a/U_e$. The symbol U_e is used to denote the velocity of the flow in the potential core downstream of the cascade which is $0.71U_\infty$. Generally speaking, the spectra have broadband characteristics common to fully turbulent flows. At higher frequencies, the spectra decay with the -5/3 slope of the inertial subrange. In the wake, the spectra are similar to those measured by Antonia and Britz (1989) in a plane two-dimensional wake. In the tip leakage vortex, the spectra show no outstanding features. The spectral levels are higher due to higher turbulence levels. However, there are no distinct peaks that would indicate a preferred passage frequency of quasi-periodic turbulence structures. Also, the spectra in the vortex do not have particularly high levels at the lowest frequencies, which is evidence that the tip leakage vortices are not subject to wandering.

5.3.3. Two-point Data Acquisition

For each two-point measurement, 150 records of 3072 samples were recorded at a sampling rate of 50 kHz over a total sampling time of about two minutes. Two-point measurements were taken in several profiles as well as in a grid configuration. The profile measurement locations are shown in figure 5.9, where the red diamonds indicate the fixed probe locations and the circles indicate the movable probe locations. The grid of measurements are shown in figure 5.10, where the red diamond indicates the fixed probe location and the black dots indicate movable probe locations. The density of movable probe locations is higher near the fixed probe location in order to properly determine the space-time correlation function at small probe separations. Because the grid measurements are so dense near the fixed probe location, figure 5.11 shows an enlarged view of those measurements.

Wenger *et al*. (1998) measured two-point profiles 1 - 4 in the radial (y) direction through the endwall region to investigate the structure of the turbulence there and its tangential (z - direction) uniformity. Profile 1 has a fixed probe location of z/c_a = -4.65, y/c_a = 0.07, where the tip leakage vortex is lifting flow off of the endwall, and extends radially to a maximum separation of $1.25c_a$. Profile 2 has a fixed probe location of z/c_a = -4.32, y/c_a = 0.07, and extending radially passes through the center of the tip leakage vortex to a maximum separation of $0.6c_a$. Profile 3 has a fixed probe location of z/c_a = -

4.1, y/c_a = 0.07, and passing to the left of the vortex center extends to a maximum separation of 1.25c_a. Profile 4 has a fixed probe location of z/c_a = -3.3, y/c_a = 0.07, and extends radially along the blade wake to a maximum separation of 1.25c_a. Profile 5 was designed to reveal the radial correlation length scales in the blade wake. It lies along the same line as profile 4, but the fixed probe location is higher at y/c_a = 0.65. Profiles 1 - 5 consisted of 20 - 30 measurements each with minimum probe separations of 0.15" (0.027c_a) and a minimum resolution of 0.05" (0.069c_a) at the smallest separations increasing to 0.40" (0.073c_a) at the largest separations. Profile 6 was designed to check for correlated fluctuations in adjacent blade wakes. Profile 6 was taken in the tangential direction (z - direction) with the fixed probe at the same location as the fixed probe location of Profile 5. The movable probe was moved to 20 separations between 1.0c_a and 1.9c_a, which put the movable probe in the adjacent blade wake.

The grid measurements consist of roughly 600 two-point measurements. The fixed probe location (z/c_a = -4.32, y/c_a = 0.07) lies underneath the center of the tip leakage vortex. A minimum probe separation of 0.15" (0.027c_a) was used in the radial and tangential directions. A minimum resolution of 0.05" (0.069c_a) was used at the smallest probe separations increasing to 0.4" (0.069c_a) at the largest separations.

5.4. Two-point Results and Discussion

5.4.1. Data analysis

Several of the two-point profiles were taken with probe separations in the z - direction. Also, the grid measurements include probe separations with both y and z components. Therefore, the data analysis was handled slightly differently from that in the previous chapters. In this case, the nine-component cross-spectrum tensor for every probe separation was first computed by taking the Fast Fourier Transform of the velocity time signals. The cross-spectrum tensor is defined as

$$G_{ik}(y, y', z, z', \omega) = \lim_{T \to \infty} (\pi / T) E[v_i^*(y, z, \omega) v_k(y + y', z + z', \omega)] \qquad (5.1)$$

where v_i and v_j denote the velocity fluctuations in the generalized directions, x_i and x_j.

To calculate a pointwise wave number frequency spectrum, the second Fourier transform is then taken with respect to distance, denoted by the symbol *s*.

$$\phi_{ik}(y,z,k_s K_x) = \frac{U_e}{2\pi}\int_{-\infty}^{\infty} G_{ik}(y,y',z,z',\omega)e^{-jk_s s}ds \tag{5.2}$$

where $s = \sqrt{y'^2 + z'^2}$. Also, in this case, the circular space-time correlation function is defined as

$$R_{ik}(y,y',z,z',\tau) = \int_{-\infty}^{\infty} G_{ik}(y,y',z,z',\omega)e^{j\omega\tau}dy' \tag{5.3}$$

The grid measurements allow analysis that is unique in several ways from that in previous chapters. Previously, the correlation functions have all been two-dimensional functions dependent on spanwise probe separation and time delay. In this case, the correlation function is three dimensional and depends on the *z* - component of probe separation as well. The three dimensional nature of the correlation function allows wave number frequency spectra to be calculated from profiles in arbitrary directions. Data at probe separations that were not measured directly could simply be interpolated using the data from the measured probe separations. Also, the grid measurements allow calculations to be made in different frames of reference.

5.4.2. Profiles

The two-point profiles mainly provide information of fluid dynamic interest, therefore only the correlation functions (as opposed to the wave number frequency spectra) corresponding to each profile are presented. The correlation functions for Profile 1 are shown in figure 5.12. The correlations are normalized by the variance of the turbulent fluctuations in the corresponding velocity component at the fixed probe location, and they are plotted against y'/c_a and $\tau U_e/c_a$. Assuming Taylor's hypothesis, τU_e represents distance in the mean flow direction. The estimated uncertainties for the correlation plots in this flow are ±0.04 for R_{uu}, R_{vv}, and R_{ww}.

The correlation functions for Profile 1 suggest the presence of large scale, turbulence structure within the tip leakage vortex. All components of the velocity fluctuations are correlated over a significant portion of the vortex. The large differences

in the forms of the correlation functions of the different velocity components indicate that the turbulence structure is highly anisotropic. Anisotropy is also evident in the non-circular contours of the individual correlation functions. The correlation function for the *u* - component shows correlations that extend to $\pm 0.4c_a$ in the streamwise (time delay) direction, and correlations that extend to $0.3c_a$ in the radial direction. The *v* - component shows correlations in the streamwise direction lasting to only about $\pm 0.2c_a$, while the correlations in the radial direction reach to almost $0.5c_a$. The *w* - component also shows correlations extending to about $\pm 0.2c_a$ in the streamwise direction, and to $0.5c_a$ in the radial direction. However, there are also regions of negative correlation flanking the main region of positive correlation in the center that extend to $\pm 0.5c_a$ in the streamwise direction. At even larger streamwise distances of $\pm 0.7c_a$ there are small regions of positive correlation. These alternating regions of correlation in the *w* - component suggest that the turbulence structures in the tip leakage vortex have an average structure spacing of about $\pm 0.7c_a$.

Figure 5.13 shows the correlation functions for Profile 2. Again, the differences in the correlation functions for the three velocity components point to a high degree of anisotropy in the turbulence structures. The irregular forms of the correlation functions are also signs of significant anisotropy. The *u* - component correlation function differs significantly from that of Profile 1. At small probe separations the correlations extend to $\pm 0.3c_a$ in the streamwise direction. However, at separations greater than about $0.1c_a$, there is evidence of some periodicity with a region of positive correlation at $-0.7c_a$ followed by a region of negative correlation at about $-0.2c_a$ and then another region of positive correlation at about $0.2c_a$. The *v* - component correlations again show faster decay with correlation only up to $\pm 0.2c_a$ in the streamwise direction. However, there is significant correlation all the way to $0.5c_a$ in the radial direction, which coincides with the upper edge of the turbulent region formed by the vortex. The *w* - component correlations only reach to $0.25c_a$ in the radial direction, but they extend to $\pm 0.2c_a$ in the streamwise direction.

The correlation functions for Profile 3 are shown in figure 5.14. Here too significant anisotropy is seen in the differences between the correlation functions for the three velocity components and in the forms of the individual correlation functions. The *u*

- component correlations are similar to those for Profile 2 in that they show roughly the same correlation at small separations. Quasi-periodicity is also suggested by the regions of negative correlation at separations greater than $0.1c_a$. The v - component correlations are also similar to those for Profile2, except that here there is also evidence of periodicity apparent in the flanking lobes of negative and positive correlation. The w - component is lopsided, extending to $-0.5c_a$ in the negative streamwise direction and only to $0.2c_a$ in the positive streamwise direction. It also reaches to almost $0.5c_a$ in the radial direction.

Profiles 4 and 5 (figures 5.15 and 5.16), which lie in the blade wake, show somewhat lower correlation length scales. In the u - component correlations for both profiles, the main regions of correlation extend to $\pm 0.3c_a$ in the streamwise direction and to only about $0.1c_a$ in the radial direction. The v - and w - component correlations have roughly semicircular contours suggesting that the turbulence is more isotropic in the blade wakes. The alternating lobes of negative and positive correlation in the w - component correlations for Profile 5 show evidence of quasi-periodic turbulence structures with an average passage spacing of $0.4c_a$.

Profile 6, which was designed to check for correlated fluctuations in adjacent blade wakes, showed no significant correlation. Therefore, the correlation functions are not presented.

5.4.3. Two-point Grid Results

5.4.3.1. Rotor Frame of Reference

The three-dimensional space-time correlation space computed from the grid measurements can be functionally expressed as $R(0.07c_a, y', -4.32c_a, z', \tau)$, which corresponds to the definition give in equation 5.3. As the functional representation indicates the fixed probe location for the two-point grid measurements is $z/c_a = -4.32$ and $y/c_a = 0.07$. The data in this correlation space is considered to be in the rotor frame of reference, because the probe locations are constant relative to the cascade blades. To examine this three-dimensional correlation space, the two-dimensional slices depicted in figure 5.17 are plotted. The vertical slice, $R(0.07c_a, y', -4.32c_a, 0, \tau)$, has already been presented in figure 5.13. This slice coincides with Profile 2.

Another slice, the front face of the correlation space (as depicted in figure 5.17B), is shown in figure 5.18. The functional representation of this slice is $R(0.07c_a, y', -4.32c_a, z', 0)$, because it corresponds to the $\tau = 0$ plane of the three-dimensional space-time correlation space. This slice shows correlations that are consistent with those for the radial correlation (Profile 2), namely that velocity fluctuations are correlated over the lower half of the tip leakage vortex. The *u* - component fluctuations are well correlated to about $0.1c_a$ in the radial direction with patches of small negative and positive correlation at larger radial separations. In the tangential (z') direction, the fluctuations correlate to about $\pm 0.2c_a$. The *v* correlations extend to a greater radial distance of $0.3c_a$. However, the region of significant positive correlation only reaches to $\pm 0.2c_a$ in the tangential direction. There is also a lobe of negative correlation to the left at $-0.2c_a$. The *w* correlations extend to $\pm 0.2c_a$ in the tangential direction and to about $0.2c_a$ in the radial direction. It should be noted that none of the components showed correlations at the adjacent tip leakage vortices shed from blades 4 and 5.

The slice that most clearly reveals the nature of the turbulence in the tip leakage vortex is the bottom ($y' = 0$) plane of the correlation space, $R(0.07c_a, 0, -4.32c_a, z', \tau)$, shown in figure 5.19. It can be seen that the correlations actually extend much farther than was seen in the previous slices. In all components, the main region of correlation lies in a thin, diagonal ellipse. The ratio of the lengths of the major axes to the minor axes in each component is approximately 5.

In order to explain the form of the correlations, it might be hypothesized that such long correlation lengths are caused by wandering of the tip leakage vortex. However, this cannot be the case because wandering would produce a region of correlation elongated in the time delay direction. An explanation can be developed by more closely considering the implications of Taylor's hypothesis, which relates time and mean flow velocity to distance in the mean flow direction. The mean flow direction is not perpendicular to the *y* - *z* plane in which the measurements were taken. Therefore, the actual three-dimensional space-time correlation space should have the time delay axis at an angle of with the y' and z' axes. The *u* - component of the bottom slice of the correlation space is

shown with the proper skewing of the time delay axis in figure 5.20. It can be seen that the correlations are most likely caused by elongated turbulent eddies with axes at angles of about 17° to the flow direction and about 20° to the axis of the tip leakage vortex. Since, this turbulence structure is thought to be produced by the large velocity deficit at the center of the vortex, it is natural to hypothesize that the structure is like that seen in the free-vortex simulations, shown in figure 5.21, of Sreedhar and Ragab (1994) and Ragab (1995). Specifically, the turbulent eddies are likely parts of larger helical structures wrapped around the tip leakage vortex.

5.4.3.2. Stator Frame of Reference

The correlation space examined in the rotor frame of reference provides much information that is valuable for understanding the flow structure. However, from an aeroacoustic point of view the stator frame of reference is of more interest, since noise is created by the impact of the turbulence on the stators. In an aircraft engine, the rotor blades are moving relative to the stators at a tangential velocity equal to the fan tip speed. In the Cascade Tunnel used to take these two-point measurements, the simulated rotor blades are stationary. Thus, to simulate the stator frame of reference, we examine the correlation space as it would be seen by the leading edge of a blade moving relative to the rotor cascade in the negative z direction (depicted in figure 5.22) at a velocity equal to the fan tip speed, which is determined by the approach freestream velocity (26.2 m/s) multiplied by the cosine of the cascade inlet angle (65.1°).

The correlation data can be transformed from the rotor frame of reference to the stator frame of reference the using the following process. The upwash velocity field of the flow behind the rotor cascade is denoted by $w_r = w_r(x,y,z,t)$, and the upwash velocity at the stator leading edge plane in the stator frame of reference is $w_s = w_s(x_s,y_s,z_s,t)$, where y_s and z_s are the stator fixed radial and tangential coordinates. At time $t = 0$ all three of the stator fixed coordinates (x_s,y_s,z_s) are coincident with the rotor fixed coordinates (x,y,z). As time progresses the stators move in the negative z direction at a velocity V_s. Thus w_s is related to w_r by the expression

$$w_s(x_s, y_s, z_s, t) = w_r(x, y, z - V_s t, t). \tag{5.4}$$

The time delay correlation between two points in the stator frame of reference, (x_s,y_s,z_s) and $(x_s + x_s', y_s + y_s', z_s + z_s')$, is defined as

$$\lim_{T\to\infty}\frac{1}{2T}\int_{-T}^{T} w_s(x_s, y_s, z_s, t)\, w_s(x_s + x_s', y_s + y_s', z_s + z_s', t + \tau)\, dt \tag{5.5}$$

Substituting in w_r for w_s gives

$$\lim_{T\to\infty}\frac{1}{2T}\int_{-T}^{T} w_r(x, y, z - V_s t, t)\, w_r(x + x, y + y', z + z' - V_s(t+\tau), t + \tau)\, dt \tag{5.6}$$

Because the flow is ergodic and periodic in the z direction, the above integral is independent of z and t. Therefore, averaging with respect to z does not change its value, and the expression becomes

$$\lim_{Z\to\infty}\frac{1}{2Z}\int_{-Z}^{Z}\ \lim_{T\to\infty}\frac{1}{2T}\int_{-T}^{T} w_r(x, y, z - V_s t, t)\, w_r(x + x', y + y', z + z' - V_s(t+\tau), t + \tau)\, dt\, dz \tag{5.7}$$

Reversing the order of integration gives

$$\lim_{T\to\infty}\frac{1}{2T}\int_{-T}^{T}\ \lim_{Z\to\infty}\frac{1}{2Z}\int_{-Z}^{Z} w_r(x, y, z - V_s t, t)\, w_r(x + x', y + y', z + z' - V_s(t+\tau), t + \tau)\, dz\, dt \tag{5.8}$$

The inner integration is done over all z. Therefore, z can be substituted in for $z - V_s t$. Performing this substitution and reversing the order of integration again gives

$$\lim_{Z\to\infty}\frac{1}{2Z}\int_{-Z}^{Z}\ \lim_{T\to\infty}\frac{1}{2T}\int_{-T}^{T} w_r(x, y, z, t)\, w_r(x + x', y + y', z + z' - V_s\tau, t + \tau)\, dt\, dz \tag{5.9}$$

This last expression shows that the two-point correlation in the stator frame of reference is simply the tangential average of the two-point correlation in the rotor frame of reference with z' replaced by $z' - V_s\tau$.

It should be made clear that the present correlation data only includes one fixed probe location, which means that the data cannot be tangentially averaged. Therefore, it is not possible to determine completely the correlation data in the stator frame of reference. However, the process for transforming frames of reference can be demonstrated, and some of the effects of such transformations can be examined.

Thus, the two-dimensional radial (y' direction) time-delay (τ) slice in the stator frame of reference would cut diagonally, with a slope V_s, in the negative z' direction through the rotor frame of reference correlation space. The path of this diagonal slice

through the bottom plane of the correlation space, $R(0.07c_a,0,-4.32c_a,z',\tau)$, is shown by line A in figure 5.19A. The radial time-delay slice in the stator frame of reference is shown in figure 5.23A. Only the correlations for the stator upwash component are shown since only this component affects noise production.

The radial time-delay correlation in the stator frame of reference is roughly similar to that in the rotor frame of reference shown in figure 5.24. Looking at line A in figure 5.19A, it can be seen that the similarity results because the two slices lie at roughly equal and opposite angles to the major axis of the elliptical correlation function of the tip leakage vortex turbulence. Thus, the similarity between the radial cuts for the two frames of reference occurs by chance. The engine operating point being simulated by the Cascade Tunnel could have just as easily been such that the slope of the cut for the stator frame of reference would have lain roughly along the major axis of the elliptical correlation function. If this had been the case, the results for the stator frame of reference would have been drastically different from those for the rotor frame of reference. Therefore, it is reasonable to conclude that the correlation function seen by a stator leading edge is strongly dependent on the operating point of the engine. Also, assuming the turbulence in a real engine tip leakage vortex is as anisotropic as seen here, the correlation function seen by the stator will be strongly dependent on engine geometry. This implies that the development of accurate prediction schemes for broadband noise generated by such rotor/stator interactions may be very difficult.

From the radial upwash correlation function in the stator frame of reference the corresponding wave number frequency spectrum is calculated and shown in figure 5.23B. Uncertainty estimates for the wave number frequency spectra calculated in this flow are ±10% for ϕ_{uu} and ±12% for ϕ_{vv} and ϕ_{ww}. It can be seen that the streamwise length scales are larger than the radial length scales at lower streamwise wave numbers. This is similar to other wave number frequency spectra presented for the lifting wake (Chapter 3) and the tip interaction (Chapter 4). This feature also suggests that Amiet's approximation could suitably used with this wave number frequency spectrum, as well.

In comparison, the radial stator upwash wave number frequency spectrum for the rotor frame of reference is shown in figure 5.24A. Coincidentally, the stator upwash velocity component is the same as the u - velocity component as shown in figure 5.25.

Thus, the stator upwash correlation function for the rotor frame of reference is the same as the *u* - component of the radial slice presented earlier in figure 5.13A. Again it can be seen that the streamwise length scales are longer than the radial length scales.

The two-point grid measurements also allow stator frame of reference calculations to be performed for a variety of stator configurations. Specifically, the correlation function and the upwash wave number frequency spectrum seen by the leading edge of leaned and swept stators may be calculated. Calculations corresponding to leaned stators simply involve taking a leaned cut through the three dimensional space-time correlation space. However, to perform calculations corresponding to stators with sweep, Taylor's hypothesis must be invoked. This is the only instance in this work, in which aeroacoustic results depend directly on the application of Taylor's hypothesis. However, any inaccuracy associated with Taylor's hypothesis, in this case, has little affect, since these results are already approximate due to the assumption that the turbulence is homogenous in the tangential direction. According to Taylor's hypothesis, as shown in figure 5.26, if two-point measurements are only taken at a downstream location of x_0, then w_r at any downstream location can be estimated by the relation,

$$w_r(x,y,z,t) = w_r\left(x_0, y, z + (x - x_0)\tan\eta, t - \frac{x - x_0}{U_e \cos\eta}\right) \tag{5.10}$$

where η is the angle of the mean flow velocity downstream of the compressor cascade, $\overrightarrow{U_e}$, relative to the *x* direction. Adding this result to that derived for the change to the stator frame of reference gives the following expression for the tangentially averaged two-point correlation function in the stator frame of reference

$$R(x,x',y,y',z',\tau) = R\left(x_0, 0, y, y', z' - x'\tan\eta - V_s\tau, \tau - \frac{x'}{U_e \cos\eta}\right). \tag{5.11}$$

In practice, this involves the interpolation of data from the grid measurements corresponding to the path of the stator leading edge through the correlation space. In this manner, the effects of curved or twisted stator leading edges may also investigated. However, only results for leaned and swept leading edges are presented here.

For a stator leaned by 30° (positive lean means a right-hand rotation of the stator about the negative *x* axis), the cross correlation function is presented in figure 5.27A.

Interestingly, the contours of positive correlation have a roughly isotropic (semicircular) form. Correspondingly, the wave number frequency spectrum shown in figure 5.27B also has roughly isotropic contours. When the stator is leaned by -30°, the isotropic effect is not present (figures 5.28A and 5.28B).

The correlation function for a stator with 30° sweep (positive sweep means a rotation of the stator about the *z'* axis) is shown in figure 5.29A. The form is fairly similar to that of the unleant/unswept stator. The corresponding wave number frequency spectrum is shown in figure 5.298B. The correlation function for -30° sweep is shown in figure 5.30A. Interestingly, this stator configuration also increases the isotropic form of the correlation function. The same can be said for the wave number frequency spectrum (figure 5.30B), however, there is a dip at the lowest streamwise wave numbers and $k_s c_a = 0$.

Combinations of sweep and lean can also be investigated. The correlation function for a stator with 30° lean and -30° sweep is shown in figure 5.31A. The sweep gives a slant to the semicircular contours seen in figure 5.27A. The corresponding wave number frequency spectrum (figure 5.27B) is unique in that it has two side lobes at streamwise wave numbers between 20 and 40.

The wave number frequency spectra for all the various stator configurations can be compared by plotting the correlation length scale as a function of frequency for each configuration. Figure 5.32 shows the correlation length scales for all stator configurations and also for the wave number frequency spectrum for the rotor frame of reference. From this figure, it can be seen that the peak along the $k_s c_a = 0$ axis is reduced in the transformation from the rotor frame of reference to the stator frame of reference. However, when lean is added, the peak increases and is maximum for the -30° lean configuration. In fact, all of the variations from the straight stator result in increased spectral levels along the $k_s c_a = 0$ axis. This indicates how sensitive the wave number frequency spectra are to the exact stator configuration. Because the correlation space is so anisotropic, certain configurations can cause higher levels of correlation to be encountered by the leading edge of the stator. Thus, the amount of broadband noise produced by the stators in a real engine will be highly dependent on the configuration and the operating point.

5.5. Conclusions

Analysis of the two-point profiles showed that the tip leakage vortices are not subject to low frequency wandering motions. Nor are the velocity fluctuations correlated in adjacent vortices or blade wakes. Analysis of the two-point grid measurements revealed significant information concerning the turbulence structure of the tip leakage vortices. Namely, the cross correlation space was found to be highly anisotropic. The form of the correlation space suggests that the turbulent eddies in the vortex are aligned along an axis that lies at an angle of 20° with the axis of the vortex. The eddies are thought to have a helical shape produced by the large axial velocity deficit at the vortex core.

Using the grid measurements and treating the flow as if it were tangentially homogeneous, correlation data and wave number frequency spectra were calculated as seen from the perspective of a stator leading edge. It was shown that the level of correlated turbulence seen by the stator leading edge is highly dependent on the engine operating point. By further assuming Taylor's hypothesis, the effects of stator lean and sweep were examined. These variations in stator configuration had significant effects on the correlation function and wave number frequency spectrum. Therefore, it was concluded that the amount of noise produced by a stator is also likely to be highly dependent on the stator configuration.

CHAPTER 6. CONCLUSIONS

Simultaneous three-component two-point hot-wire measurements made in three flows of aeroacoustic interest were analyzed to provide fundamental information concerning the turbulence structure. This information is designed to aid future aeroacoustic researchers in developing noise prediction/reduction methods for helicopter rotors and high bypass ratio fans.

6.1. Lifting Wake Conclusions

The first set of two-point measurements to be analyzed were taken in the lifting wake of a rectangular NACA 0012 half wing set at 5° angle of attack. 'Pointwise' wave number frequency spectra and space-time cross correlation functions were calculated at four locations in the wake. The upwash wave number frequency spectra were found to differ greatly from the von Kármán isotropic spectrum, which has traditionally been used to make aeroacoustic computations. The differences between the measured and theoretical spectra are a result of significant anisotropy in the large scale coherent turbulence structures present in the wake.

Two upwash wave number frequency spectra that were taken in the roughly spanwise homogenous region of the wake served as estimations of the 'full' wave number frequency spectra in that region. These spectra, therefore, could be used in place of the von Kármán isotropic spectrum for aeroacoustic calculations. As such, calculations of directionality, $\Phi_{ww}(K_x, K_x)$, and $\Phi_{ww}(K_x, 0)$ were performed using the measured spectra and compared with those calculations based on the von Kármán spectrum. Large differences were found in the results, which indicates that the von Kármán spectrum does not produce accurate aeroacoustic results.

The von Kármán spectrum was adjusted by applying streamwise and spanwise length scales that differ by the amounts estimated for the measured spectra. The directionality calculations were repeated using the adjusted von Kármán spectrum, and the results were found to much more closely match the directionality obtained using the measured spectra. This illustrates that it is necessary to account for the anisotropy present in 'real' turbulence, if aeroacoustic calculations are to produce accurate results.

Amiet's approximation, where the full upwash wave number frequency spectrum, $\Phi_{ww}(K_x, k_y)$, is replaced by $\Phi_{ww}(K_x, 0)$, was also investigated. By comparing $\Phi_{ww}(K_x, K_x)$ and $\Phi_{ww}(K_x, 0)$, it was found that the variation of $\Phi_{ww}(K_x, k_y)$ with respect to k_y was small enough that $\Phi_{ww}(K_x, 0)$ could reasonably represent $\Phi_{ww}(K_x, k_y)$.

6.2. Tip Interaction Conclusions

Five sets of two sided two-point measurements taken in the region of interaction between two tip vortices were analyzed to reveal information concerning the turbulence structure that would be encountered by a hypothetical blade passing through the region of interaction. The interaction flow was generated by two cantilevered, rectangular NACA 0012 half wings. The airfoils were arranged so that the tip vortex from the first airfoil passed just to the suction side of the downstream airfoil. Downstream of the second airfoil, the two tip vortices rolled up around each other. This flow was designed to model a type of interaction between rotor wakes that has been identified as a source of blade-wake interaction (BWI) noise in helicopter rotors.

The 'pointwise' wave number frequency spectra and the space-time correlation functions were calculated for each of the five two-point profiles measured in the interaction region. The results for the two profiles with fixed probe locations in the vortex cores were dominated by vortex wandering. In the wave number frequency spectra for these two profiles, the spanwise and streamwise wave numbers associated with vortex wandering were clearly distinguishable from those associated with the coherent turbulence structures. Therefore, numerical estimates of the proportions of energy associated with vortex wandering were made.

The wave number frequency spectra for the other profiles (one between the two vortex cores, and the other two in the surrounding wake above and below the two cores) showed strong evidence that the turbulence is dominated by highly anisotropic coherent turbulence structures. As such, these spectra differed significantly from the von Kármán isotropic spectrum. However, the upwash spectra do bear remarkable likeness to the two upwash spectra calculated in the spanwise homogenous region of the lifting wake. This suggests that the wave number frequency spectra may be fairly insensitive to local flow

conditions. This also implies that Amiet's approximation may reasonably be applied even for this complex flow.

6.3. Fan Cascade Conclusions

Two-point measurements taken in several profiles in the blade wakes and in the tip leakage vortex of a rotor cascade were analyzed. The most significant findings of these profile measurements is that the tip leakage vortices are not subject to wanderings, and that there are no correlated fluctuations between adjacent blade wakes or between adjacent tip leakage vortices.

Two-point measurements taken in a grid were also analyzed to provide more complete information concerning the turbulence structure of the tip leakage vortex . By calculating the cross-correlation for all of the two-point grid measurements, a three dimensional space-time correlation space was created. Information concerning the turbulence structure of the tip leakage vortex was revealed by examined two dimensional planes of the three dimensional space-time correlation space. The space-time correlations suggest that the turbulence in the tip leakage vortex is highly anisotropic with turbulent eddies aligned along an axis that lies at an angle of 20° to the axis of the vortex. Based on direct numerical simulations performed by Ragab (1995) and Sreedhar and Ragab (1994), the turbulent eddies are thought to have a helical shape produced as a result of the large axial velocity gradients in the tip leakage vortex.

The two-point grid measurements allow the space-time correlations to be examined from various frames of reference. In particular, the turbulence structure that would be encountered by the leading edge of a hypothetical stator blade moving relative to the rotor cascade was estimated. It was demonstrated that due to the anisotropic nature of the turbulence in the tip leakage vortex the level of correlation seen by the stator leading edge is likely to depend heavily on the engine operating speed and the stator configuration.

REFERENCES

Amiet, R. K., "Acoustic Radiation from an Airfoil in a Turbulent Stream," *Journal of Sound and Vibration*, Vol. 41, No. 4, 1975, pp. 407-420.

Antonia, R. A., and Britz, D., "Phase-Averaging in the Turbulent Far Wake," *Experiments in Fluids*, Vol. 7, No. 1, 1989, pp. 138-142.

Barsoum, M. L., Kawall, J. G., and Keffer, J. F., "Spanwise Structure of the Plane Turbulent Wake," *Physics of Fluids*, Vol. 21, Feb. 1978, pp. 157-161.

Bearman, P. W., "Corrections for the Effect of Ambient Temperature Drift on Hot-wire Measurements in Incompressible Flow," *DISA Information*, Vol. 11, pp. 25-30.

Bracewell, Ronald N., *The Fourier Transform and Its Applications*, 2nd ed, Revised, McGraw-Hill, Inc., 1986.

Brezillon, J., Prieur, J., and Rahier, G., "Investigation On Broadband Helicopter Noise," *Proceedings of the AHS Specialists Meeting for Rotorcraft Acoustics and Aerodynamics*, Williamsburg, VA, October 28-30, 1997.

Brooks, T. F., Marcolini, M. A., and Pope, D. S., "Main Rotor Broadband Noise Study in the DNW," *Proceedings of the AHS Specialists Meeting for Rotorcraft Acoustics and Aerodynamics*, Arlington, TX, February 25-37, 1987.

Burley, C. L., Brooks, T. F., Splettstoesser, W. R., Shultz, K. J., Bucholtz, H., Wagner, W., and Weitemeyer, W., "Blade Wake Interaction Noise for a B0-105 Main Rotor," *Proceedings of the AHS Specialists Meeting for Rotorcraft Acoustics and Aerodynamics*, Williamsburg, VA, October 28-30, 1997.

Devenport, W. J., Rife, M. C., Liapis, S. I., and Follin, G. J., "The Structure and Development of a Wing-Tip Vortex," *Journal of Fluid Mechanics*, Vol. 312, 1996, pp. 67-106.

Devenport, W. J., Wittmer, K. S., and Wenger, C. W., "The Spectral and Statistical Properties of Turbulence Generated by a Vortex/Blade-Tip Interaction," AOE Dept. Report, Virginia Tech, Blacksburg VA 24061, 1997.

Devenport, W. J., Wenger, C. W., Glegg, S. A., and Miranda, J. A., "Wave Number Frequency Spectra of a Lifting Wake for Broadband Noise Prediction," *AIAA Journal*, Vol. 36, No. 6, 1998, pp. 881-887.

Engel, M. A., "A Wind Tunnel Investigation of a Wing-tip Trailing Vortex," M. S. Thesis, Aerospace and Ocean Engineering Dept., Virginia Polytechnical Inst. and State Univ., Blacksburg, VA, May 1995.

Glegg, S. A. L., "Prediction of Blade-wake Interaction Noise Based on a Turbulent Vortex Model," *AIAA Journal*, Vol. 29, No. 10, October 1991, pp. 1545-1551.

Glegg, S. A. L., and Devenport, W. J., "The Application of Experimental Data to Blade Wake Interaction Noise Prediction," in *Unsteady Aerodynamics, Aeroacoustics and Aeroelasticity of Turbomachines and Propellers*, Ed. by H. M. Atassi, Springer Verlag, New York, 1992.

Glegg, S. A. L., and Jochault, C., "Broadband Self Noise from a Ducted Fan," 3rd AIAA/CEAS Aeroacoustic Conference, Atlanta, GA, May 12-14, 1997, AIAA Paper 97-1612.

Glegg, S. A. L., Wittmer, K. S., Devenport, W. J., and Pope, D. S., "Broadband Noise Generated by Blade Wake Interactions", *Proceedings of the AHS Specialists Meeting for Rotorcraft Acoustics and Aerodynamics*, Williamsburg, VA, October 28-30, 1997. Submitted to Journal of the American Helicopter Society.

Keffer, J. F., "The Uniform Distortion of a Turbulent Wake," *Journal of Fluid Mechanics*, Vol. 22, 1965, pp. 135-159.

Maxwell, L. and Evans, G., "Schools raise ruckus to reduce airport noise," *CNN Online*, http://www.cnn.com/TECH/9802/05/t_t/airplane.noise/index.html, February, 1998.

Miranda, J. A., "The Structure of a Trailing Vortex Wake," M. S. Thesis, Aerospace and Ocean Engineering Dept., Virginia Polytechnical Inst. and State Univ., Blacksburg, VA, May 1996.

Miranda, J. A. and Devenport, W. J., "Two Point Measurements in Trailing Vortices," AIAA Paper 96-0804, Jan. 1996.

Miranda, J. A. and Devenport, W. J., "Turbulence Structure in the Spiral Wake Shed by a Lifting Wake," *AIAA Journal*, Vol. 36, No. 4, 1998, pp. 658-660.

Muthanna, C., "Flowfield Downstream of a Linear Compressor Cascade with Tip-leakage," Masters Thesis, AOE Dept. Virginia Tech, December 1998.

Muthanna, C., Wittmer, K. S., and Devenport, W. J., "Turbulence Structure of the Flow Downstream of a Compressor Cascade with Tip Leakage", AIAA 36th Aerospace Sciences Meeting and Exhibit, Reno, Nevada, January 9-12, 1998, AIAA Paper 98-0420.

Hinze, J. O., *Turbulence*, McGraw-Hill, Inc., New York, 1975.

Ragab, S., "Direct Numerical Simulation of Instability Waves in a Trailing Vortex", AIAA 33rd Aerospace Sciences Meeting and Exhibit, Reno, Nevada, January 9-12, 1995, AIAA Paper 95-0591.

Sreedhar, M. K. and Ragab, S. A., "Large Eddy Simulations of a Longitudinal Vortex", AIAA 32nd Aerospace Sciences Meeting and Exhibit, Reno, Nevada, January 10-13, 1994, AIAA Paper 94-0529.

Sutliff, D. L., Bridges, J., and Envia, E., "Comparison of Predicted Low Speed Fan Rotor/Stator Interaction Modes to Measured," 3rd AIAA/CEAS Aeroacoustic Conference, Atlanta, GA, May 12-14, 1997, AIAA Paper 97-1609.

Townsend, A. A., *The Structure of Turbulent Shear Flow*, Cambridge Univ. Press, London, 1956, pp. 131-170.

Wenger, C. W., Devenport, W. J., Wittmer, K. S., and Muthanna, C., "Two-point Measurements in the Wake of a Compressor Cascade," AIAA Paper 98-2556, June 1998.

Wittmer, K. S. and Devenport, W. J., "Interaction of a streamwise vortex with a full-span blade," AIAA Paper 95-2214, June 1995.

Wittmer, K. S., Devenport, W. J., and Rife, M. C., "Perpendicular blade vortex interaction," *AIAA Journal*, Vol. 33, No. 9, 1995, pp. 1667-1674.

Wittmer, K. S., "Turbulent Flowfield Downstream of a Perpendicular Airfoil-Vortex Interaction," Ph. D. Dissertation, AOE Dept., Virginia Tech, November, 1996.

Wittmer, K. S. and Devenport, W. J., "Turbulence structure resulting from a perpendicular airfoil-vortex interaction," AIAA Paper 96-2014, June 1996.

Wittmer, K. S., Devenport, W. J., and Zsoldos, J. S., "A Four-sensor Hot-wire Probe System for Three-component Velocity Measurement," *Experiments in Fluids*, to be published in 1998.

Wittmer, K. S., Devenport, W. J., and Wenger, C. W., "Turbulence Structure Resulting from a Vortex/Wing-tip Encounter," *Journal of the American Helicopter Society*, *t*o be published in the 1999.

Wygnanski, I., Champagne, F., and Marasli, B., "On the Large Scale Structures in Two-Dimensional Small-Deficit Turbulent Wakes," *Journal of Fluid Mechanics*, Vol. 168, 1986, pp. 31-71.

FIGURES

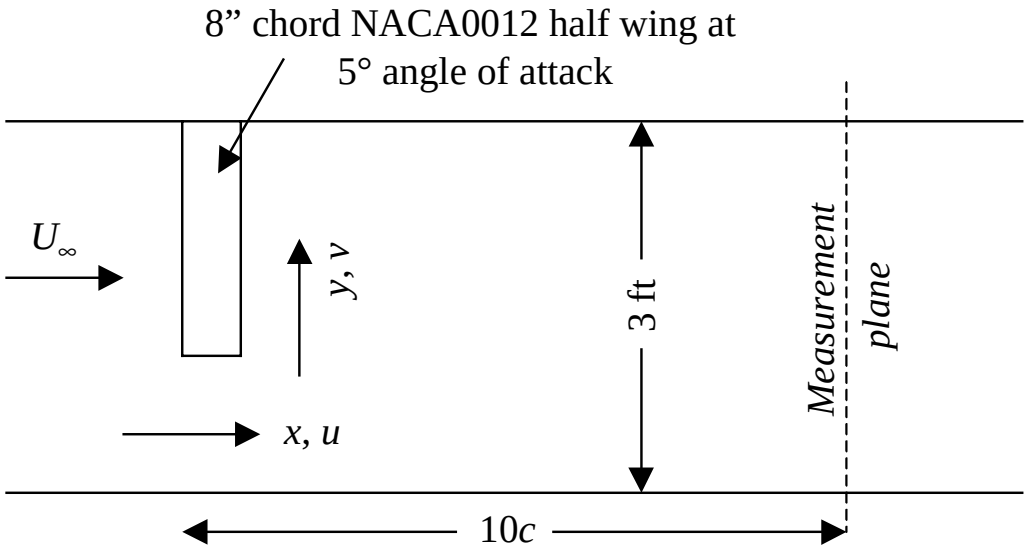

Figure 3.1

Schematic of the Virginia Tech Subsonic Wind Tunnel showing the coordinate definitions and the measurement plane for Miranda’s (1996) measurements. The *z* coordinate and the corresponding upwash velocity component, *w*, are directed out of the paper.

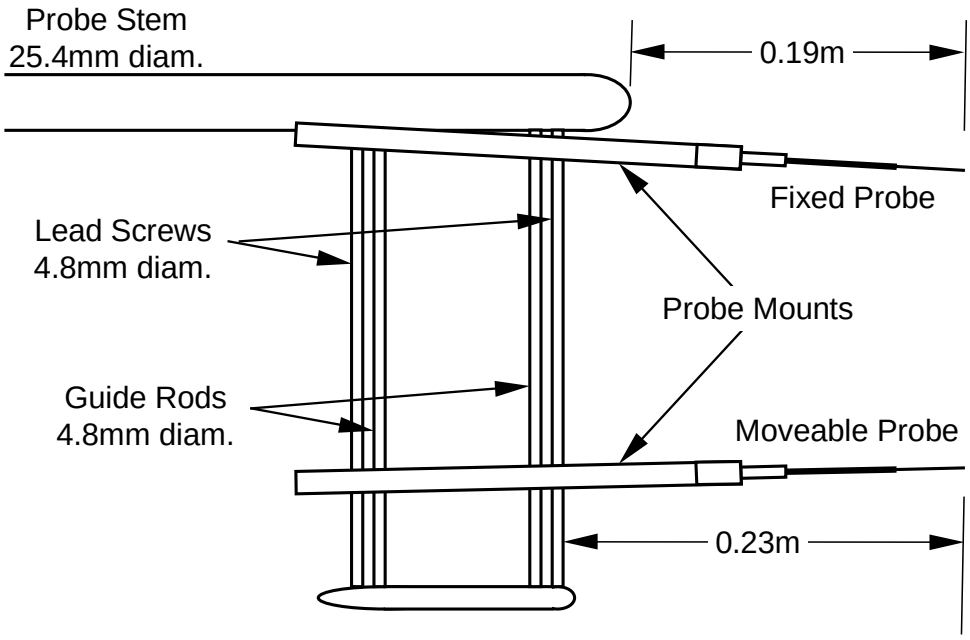

Figure 3.2

A diagram depicting the two-probe holder used for taking two-point profiles. The upper probe holder holds one probe fixed, while the other probe holder can be traversed to different probe separations.

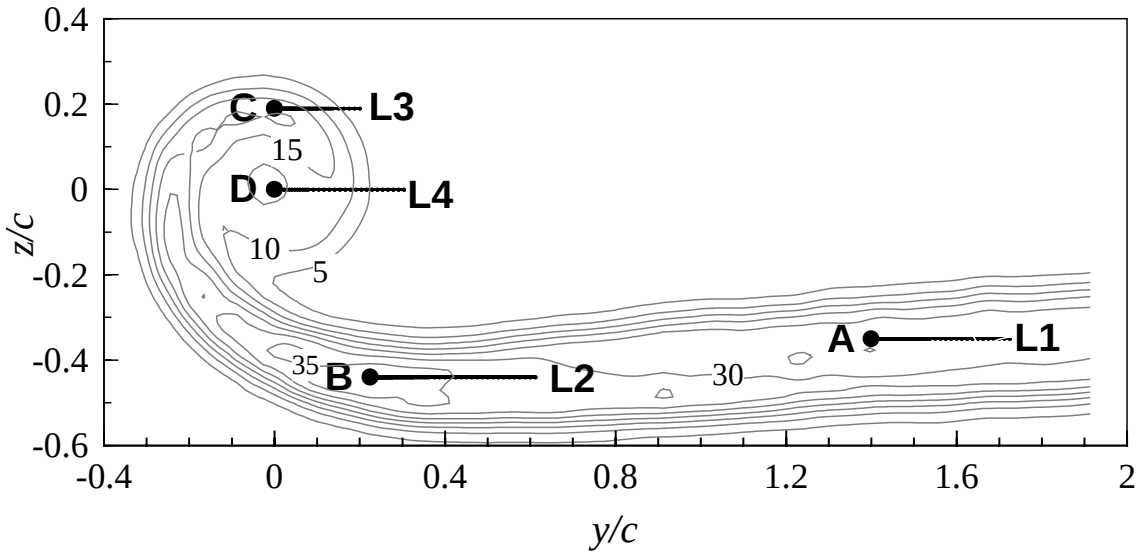

Figure 3.3

Contours of axial turbulence normal stress $\overline{u^2}/U_\infty^2 \times 10^5$ measured 10 chordlengths downstream of the wing leading edge. The two-point profiles are indicated with the black dots, A-D, indicated the fixed probe locations, and the lines L1-L4 indicating the corresponding ranges of probe separations.

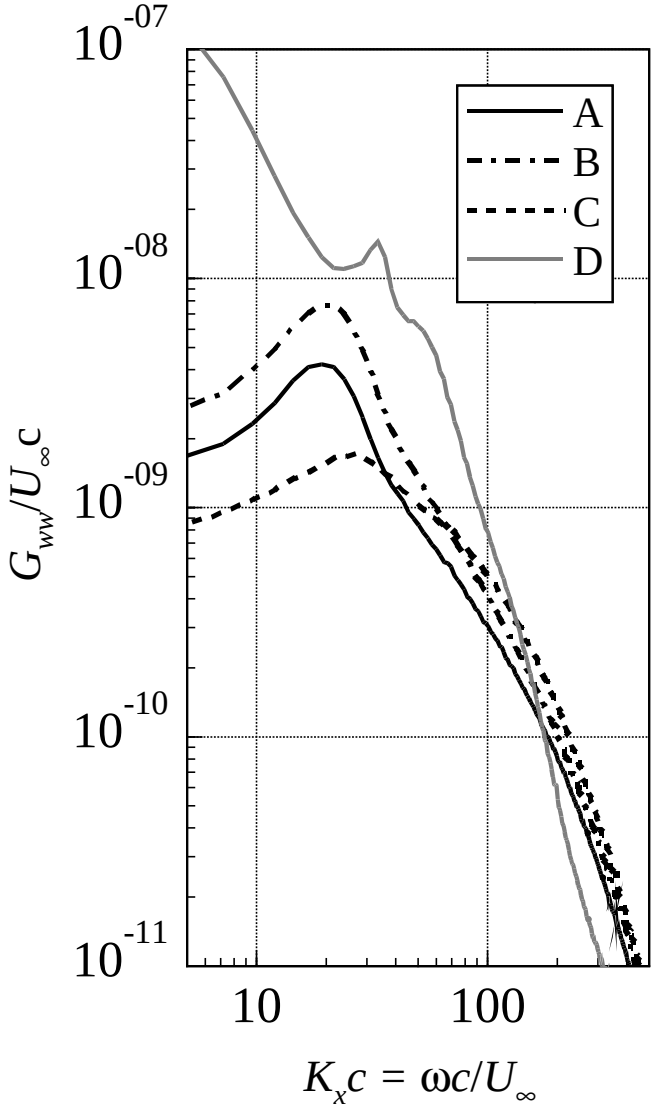

Figure 3.4

Autospectra of the upwash velocity fluctuations at the fixed probe locations A-D shown in figure 3.3.

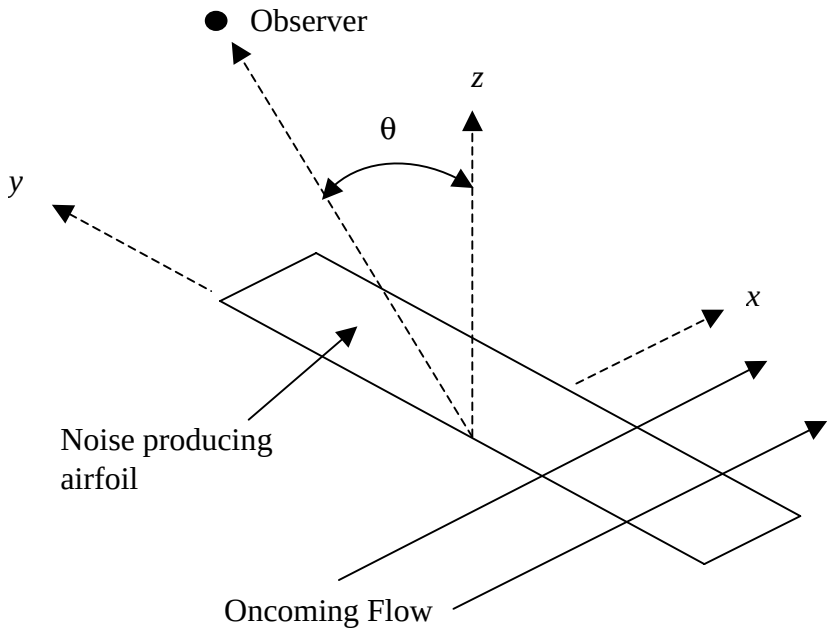

Figure 3.5

A schematic showing the coordinate definitions which describe an observer's location relative to a noise producing airfoil in a turbulent flow. The angle θ lies in the *y* - *z* plane.

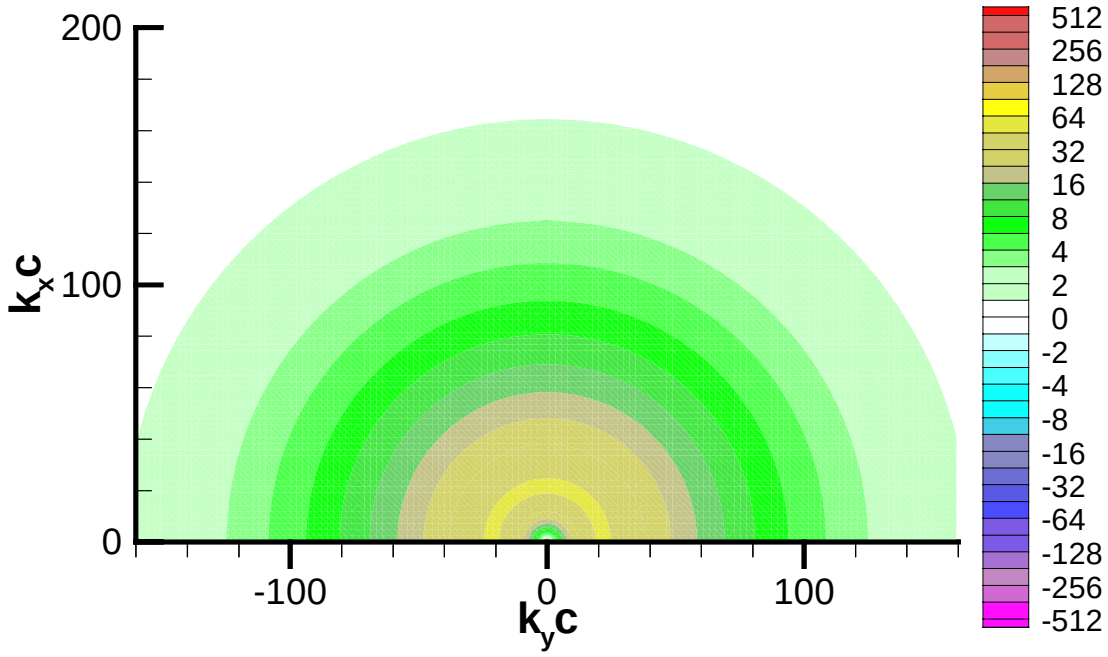

Figure 3.6

The wave number frequency spectrum based on the von Kármán model of isotropic turbulence. The length scale used to calculate this spectrum and nondimensionalize the wave numbers is the chord length, c = .203 m.

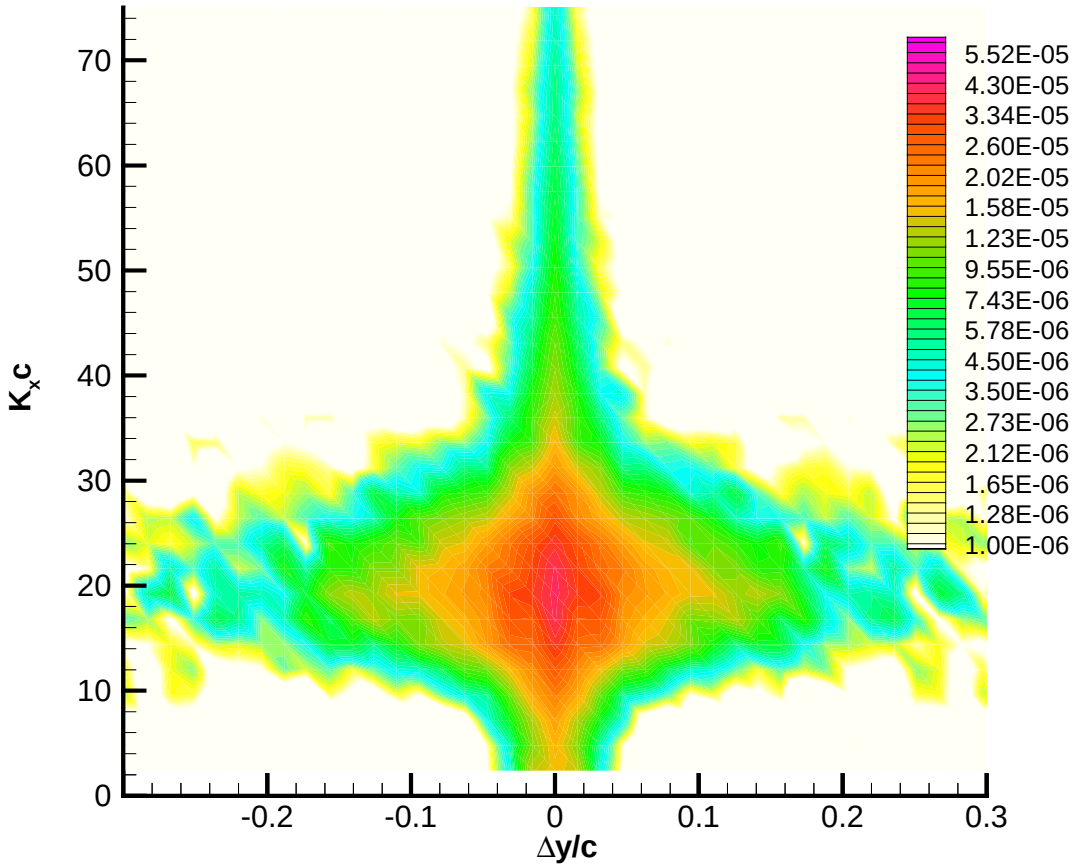

Figure 3.7

The cross-spectral density for the two-point profile A/L1 shown in figure 3.3. Contours are $\frac{G_{ww}}{cU_\infty}$.

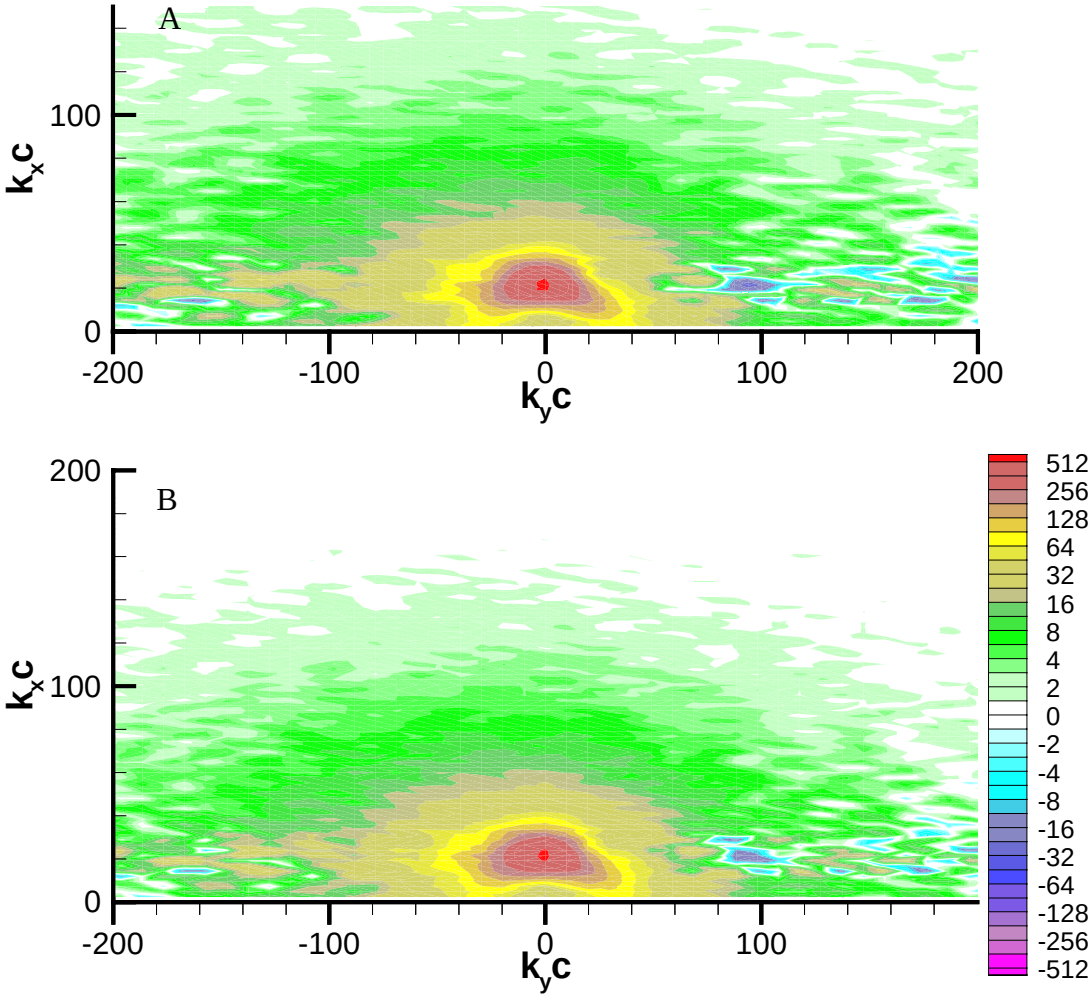

Figure 3.8

Comparison of the upwash wave number frequency spectrum for profile B/L2 (figure 3.3) calculated using A) only the measured data and B) supplemental data at small probe separations based on the Liepmann model of isotropic turbulence. Contours are $\frac{\phi_{ww} U_\infty}{\left(c^2 \overline{w^2}\right)} \times 10^6$.

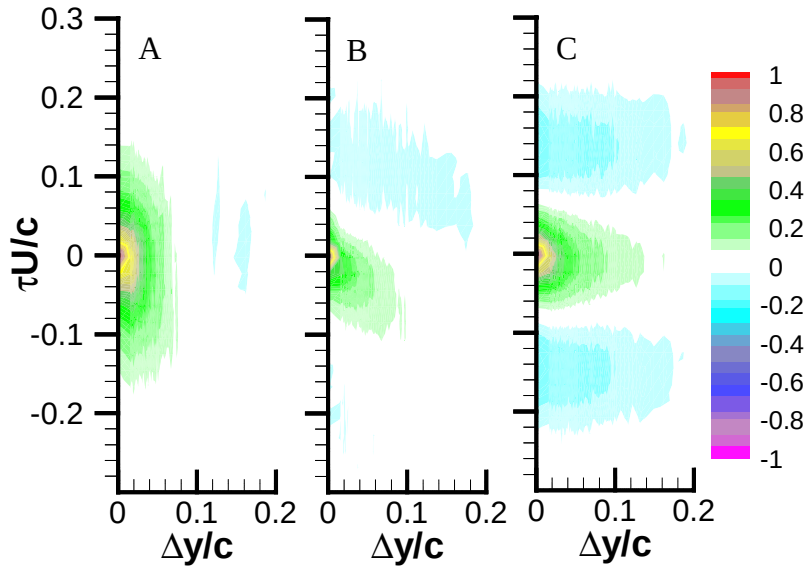

Figure 3.9

The cross-correlation functions for two-point profile A/L1 (figure 3.3). Plot A is $\frac{R_{uu}}{\overline{u^2}}$, plot B is $\frac{R_{vv}}{\overline{v^2}}$, and plot C is $\frac{R_{ww}}{\overline{w^2}}$.

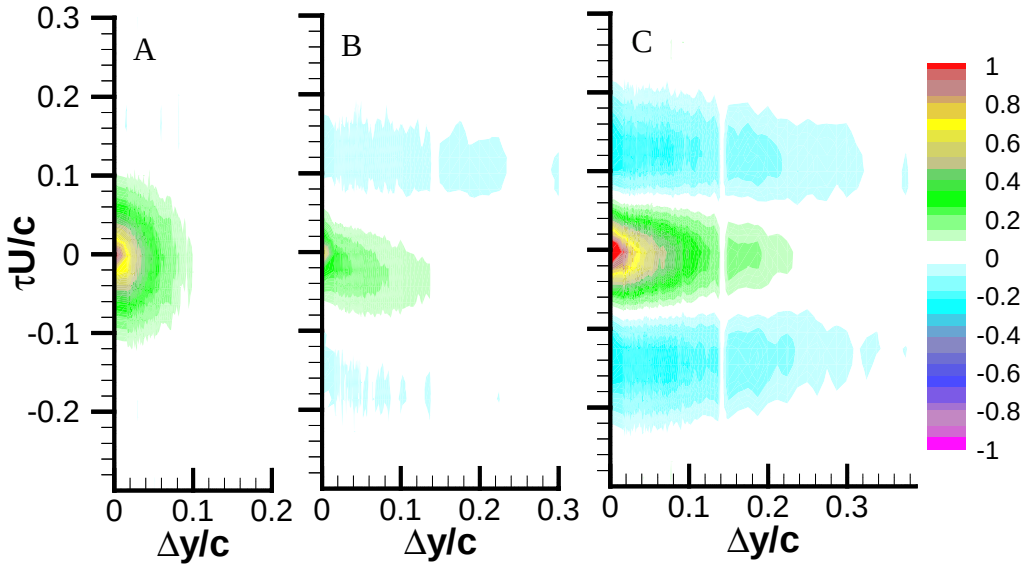

Figure 3.10

The cross-correlation functions for two-point profile B/L2 (figure 3.3). Plot A is $\frac{R_{uu}}{\overline{u^2}}$, plot B is $\frac{R_{vv}}{\overline{v^2}}$, and plot C is $\frac{R_{ww}}{\overline{w^2}}$.

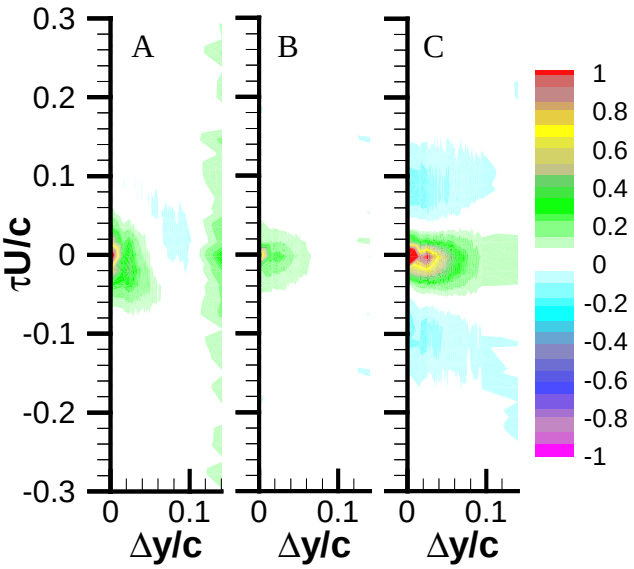

Figure 3.11

The cross-correlation functions for two-point profile C/L3 (figure 3.3). Plot A is $\frac{R_{uu}}{\overline{u^2}}$, plot B is $\frac{R_{vv}}{\overline{v^2}}$, and plot C is $\frac{R_{ww}}{\overline{w^2}}$.

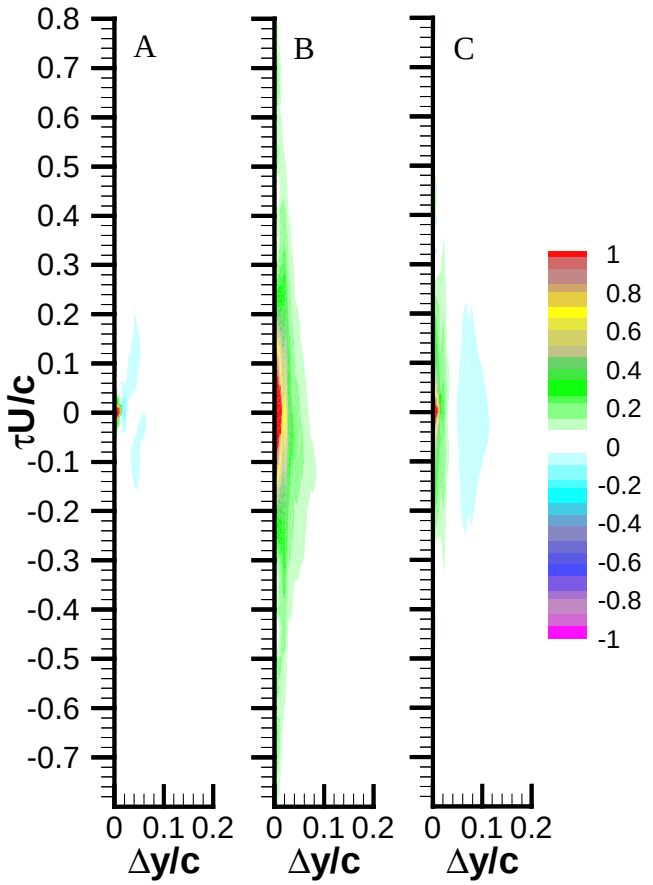

Figure 3.12

The cross-correlation functions for two-point profile D/L4 (figure 3.3). Plot A is $\frac{R_{uu}}{\overline{u^2}}$, plot B is $\frac{R_{vv}}{\overline{v^2}}$, and plot C is $\frac{R_{ww}}{\overline{w^2}}$.

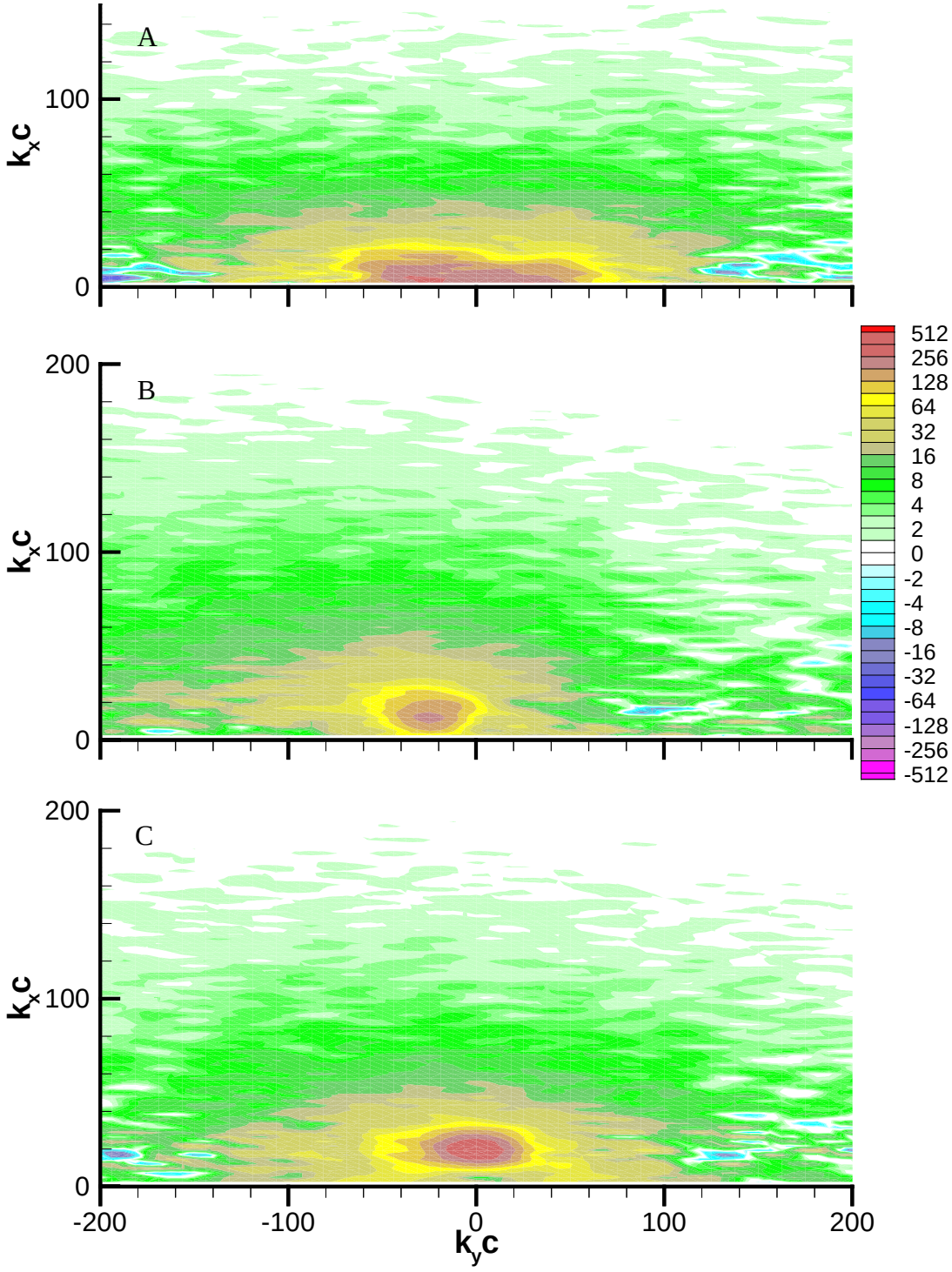

Figure 3.13

Wave number frequency spectra calculated for two-point profile A/L1. Contours are A) $\frac{\phi_{uu}}{\overline{u^2}\overline{c^2}}\times 10^6$, B) $\frac{\phi_{vv}}{\overline{v^2}\overline{c^2}}\times 10^6$, C) $\frac{\phi_{ww}}{\overline{w^2}\overline{c^2}}\times 10^6$.

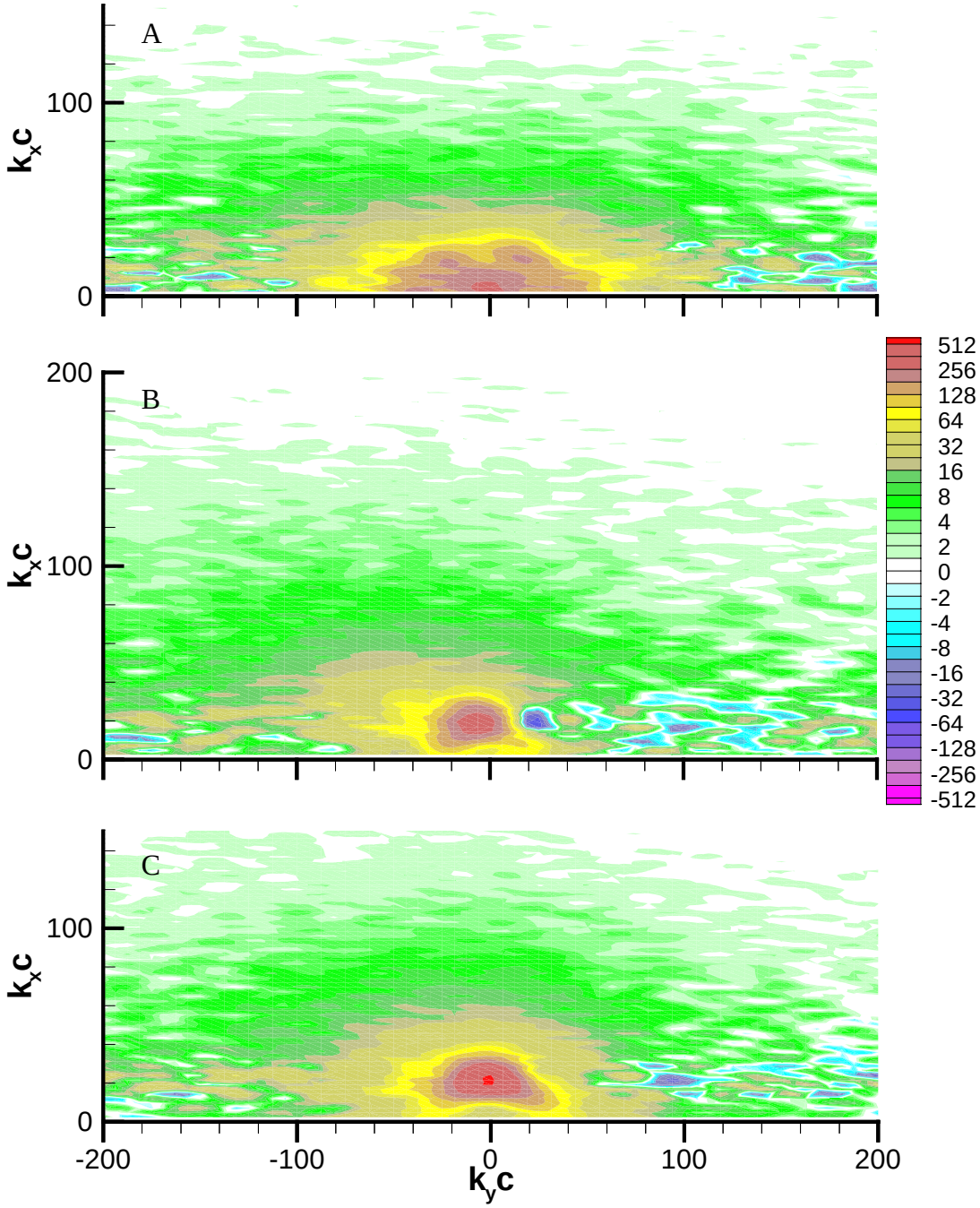

Figure 3.14

Wave number frequency spectra calculated for two-point profile B/L2. Contours are A) $\frac{\phi_{uu}}{\overline{u^2}\overline{c^2}}\times 10^6$, B) $\frac{\phi_{vv}}{\overline{v^2}\overline{c^2}}\times 10^6$, C) $\frac{\phi_{ww}}{\overline{w^2}\overline{c^2}}\times 10^6$.

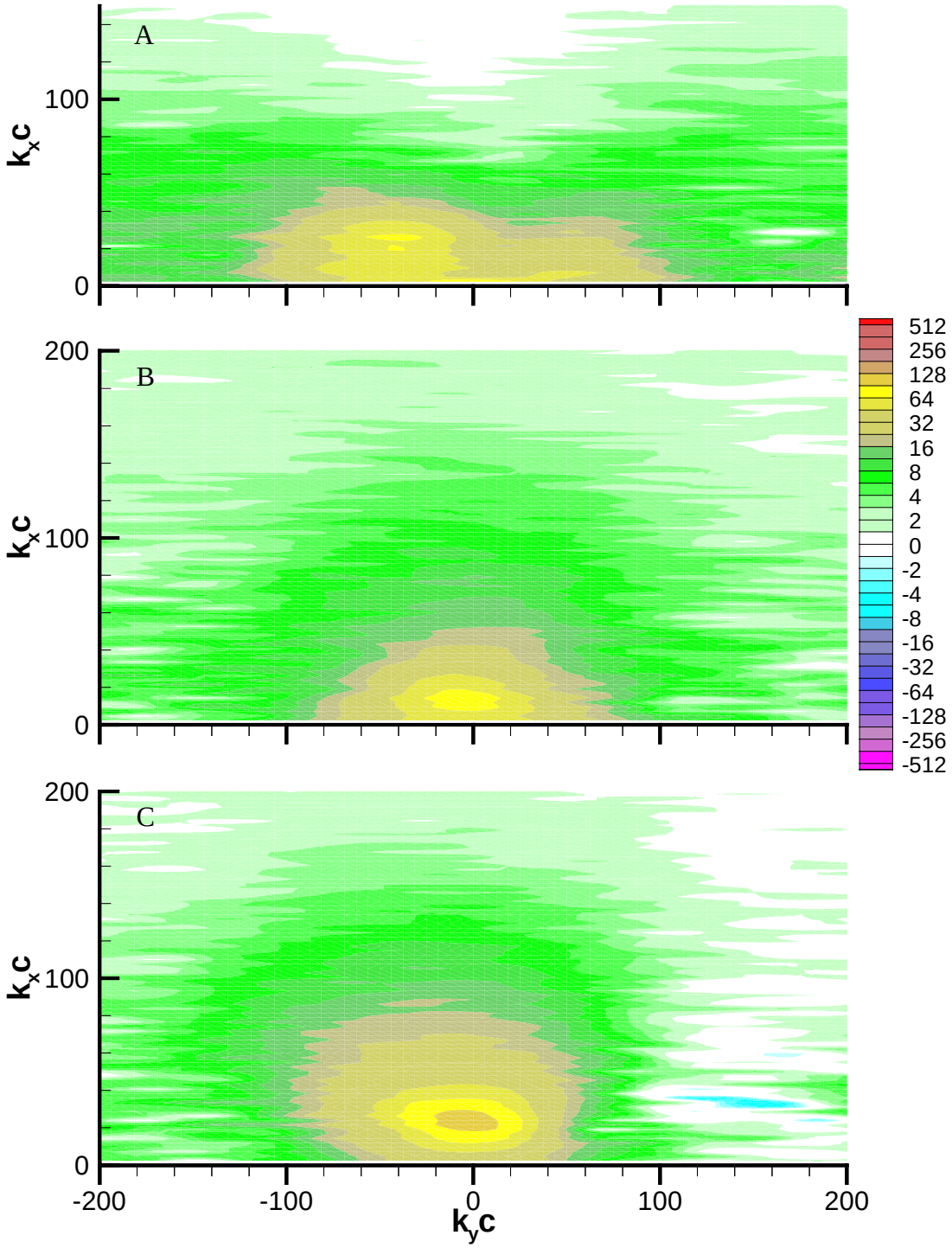

Figure 3.15

Wave number frequency spectra calculated for two-point profile C/L3. Contours are A) $\frac{\phi_{uu}}{\overline{u^2}\overline{c^2}}\times 10^6$, B) $\frac{\phi_{vv}}{\overline{v^2}\overline{c^2}}\times 10^6$, C) $\frac{\phi_{ww}}{\overline{w^2}\overline{c^2}}\times 10^6$.

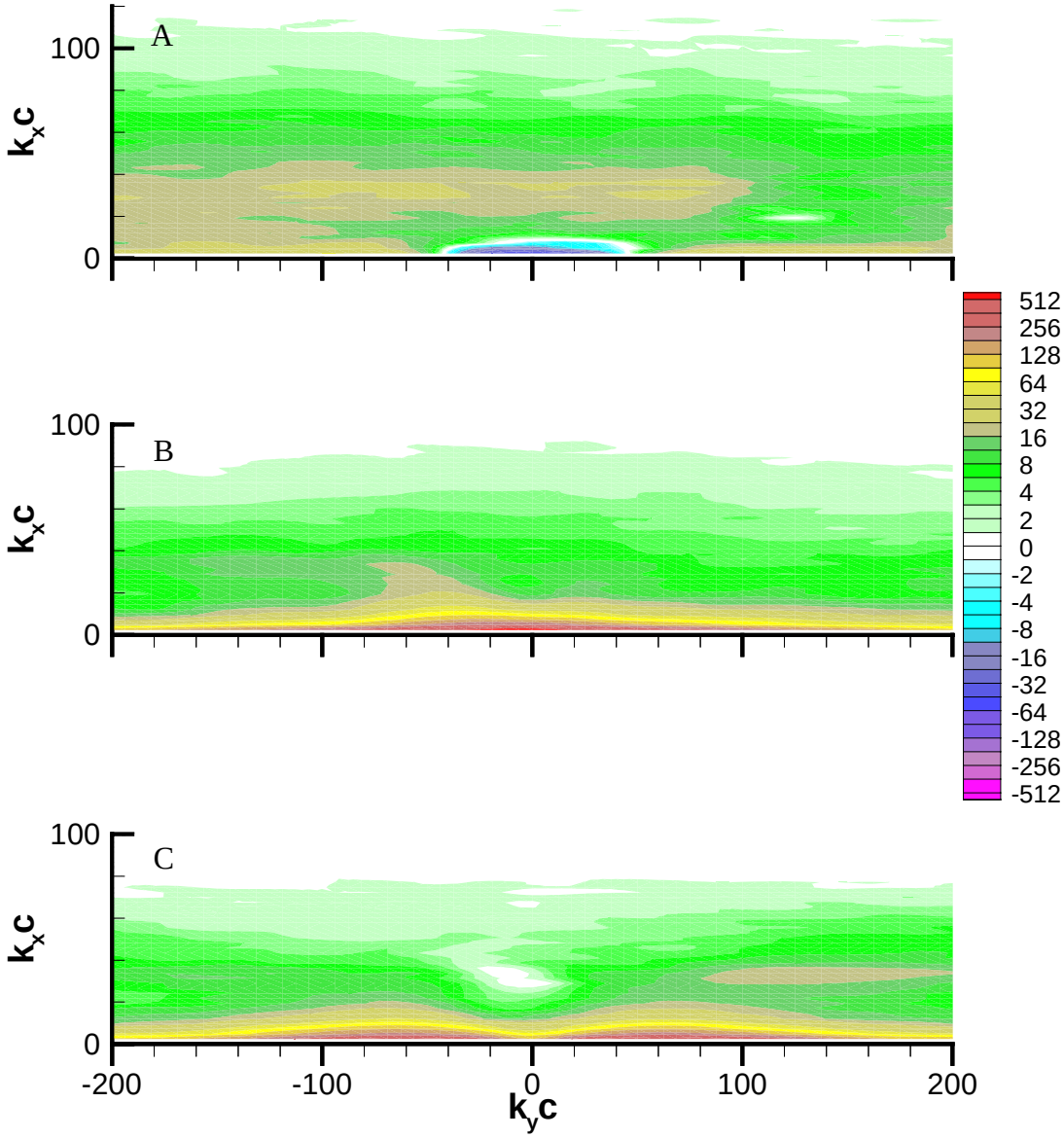

Figure 3.16

Wave number frequency spectra calculated for two-point profile D/L4. Contours are A) $\frac{\phi_{uu}}{\overline{u^2}\overline{c^2}}\times 10^6$, B) $\frac{\phi_{vv}}{\overline{v^2}\overline{c^2}}\times 10^6$, C) $\frac{\phi_{ww}}{\overline{w^2}\overline{c^2}}\times 10^6$.

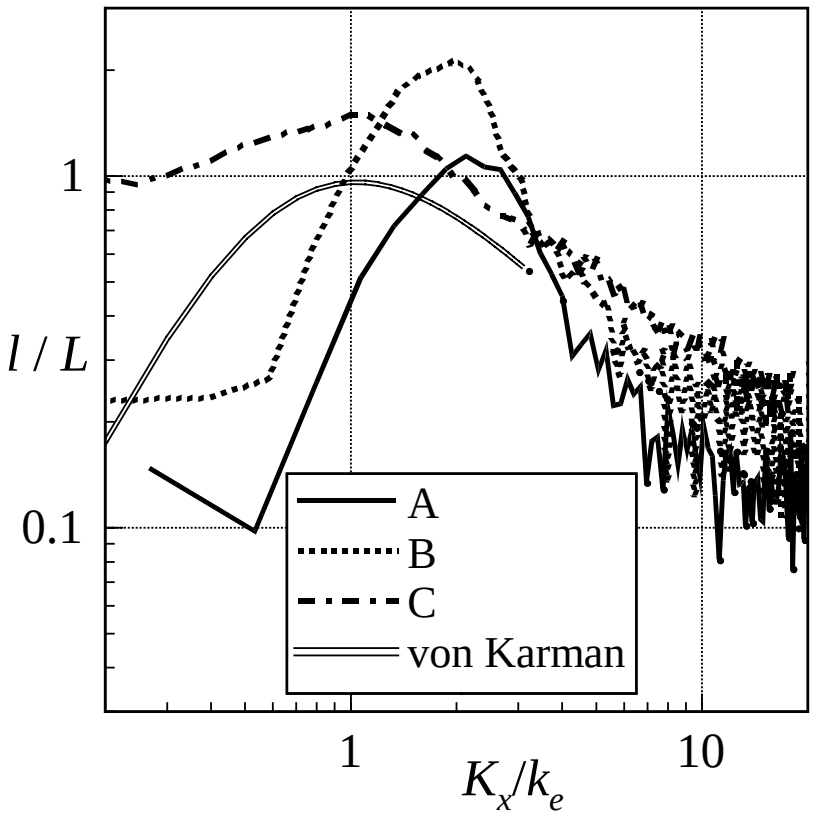

Figure 3.17

Correlation length scales as a functions of normalized frequency for locations A, B, and C compared with the correlation length scale based on the von Kármán isotropic spectrum.

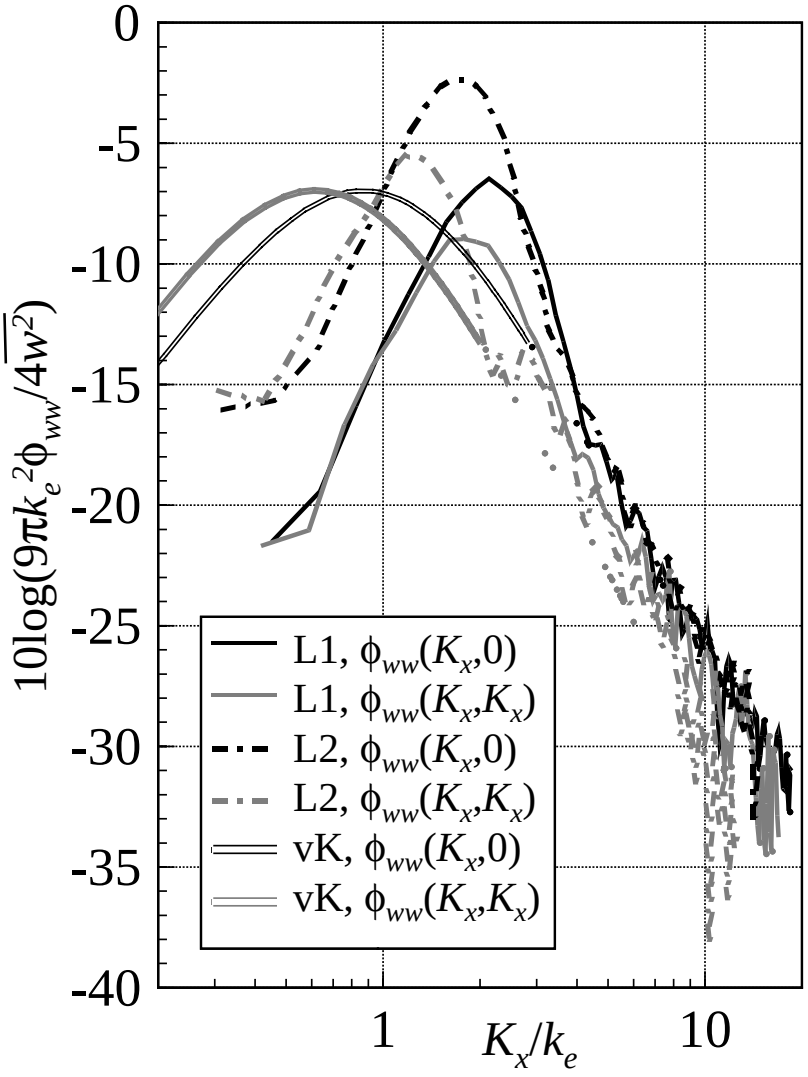

Figure 3.18

Plots of $\phi_{ww}(K_x,0)$ and $\phi_{ww}(K_x,K_x)$ for two-point profiles A/L1 and B/L2 and for the von Kármán isotropic spectrum. At location A, $k_e c = 9.0$, and at location B, $k_e c = 12.4$.

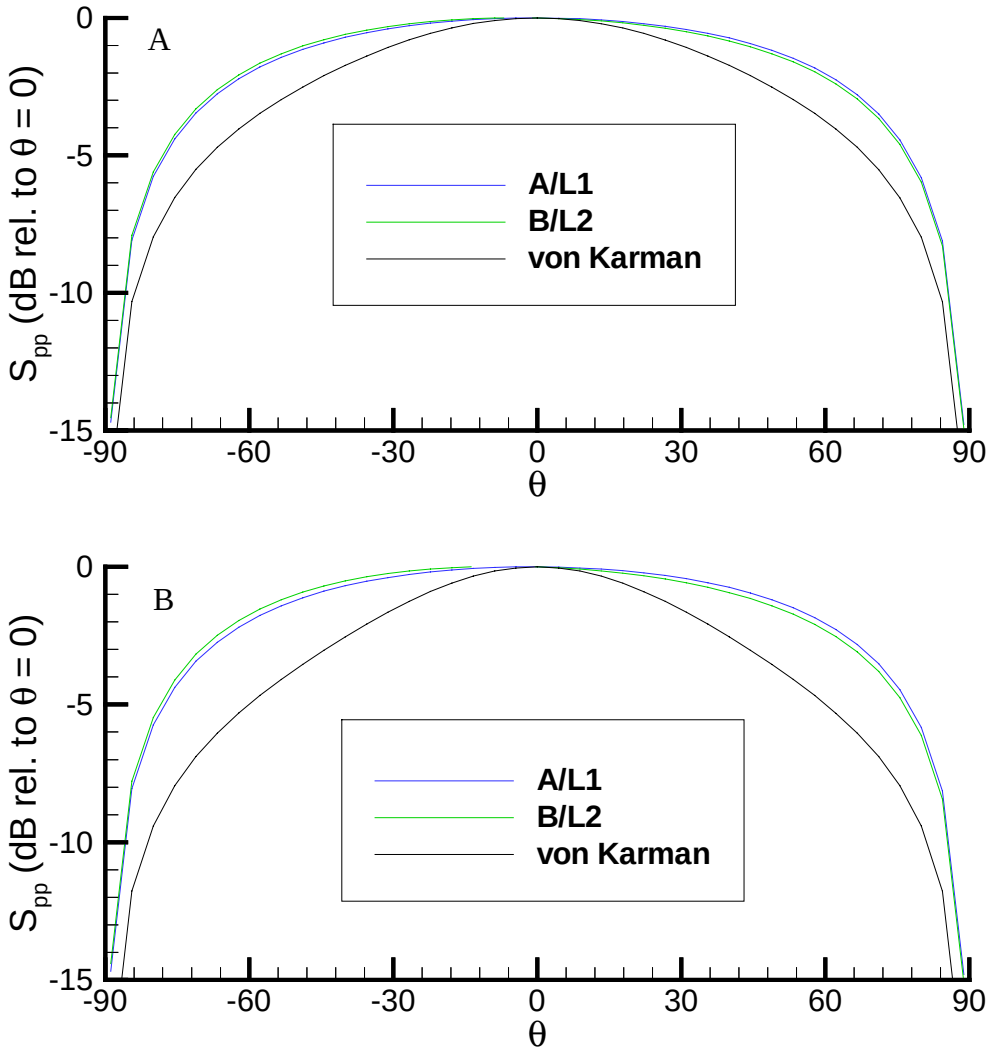

Figure 3.19

The directionality calculated from the upwash wave number frequency spectra of the two-point profiles A/L1 and B/L2 compared with the directionality calculated using the von Kármán isotropic turbulence spectrum. For A) K_x/k_e = 1.5 and for B) K_x/k_e = 6.0.

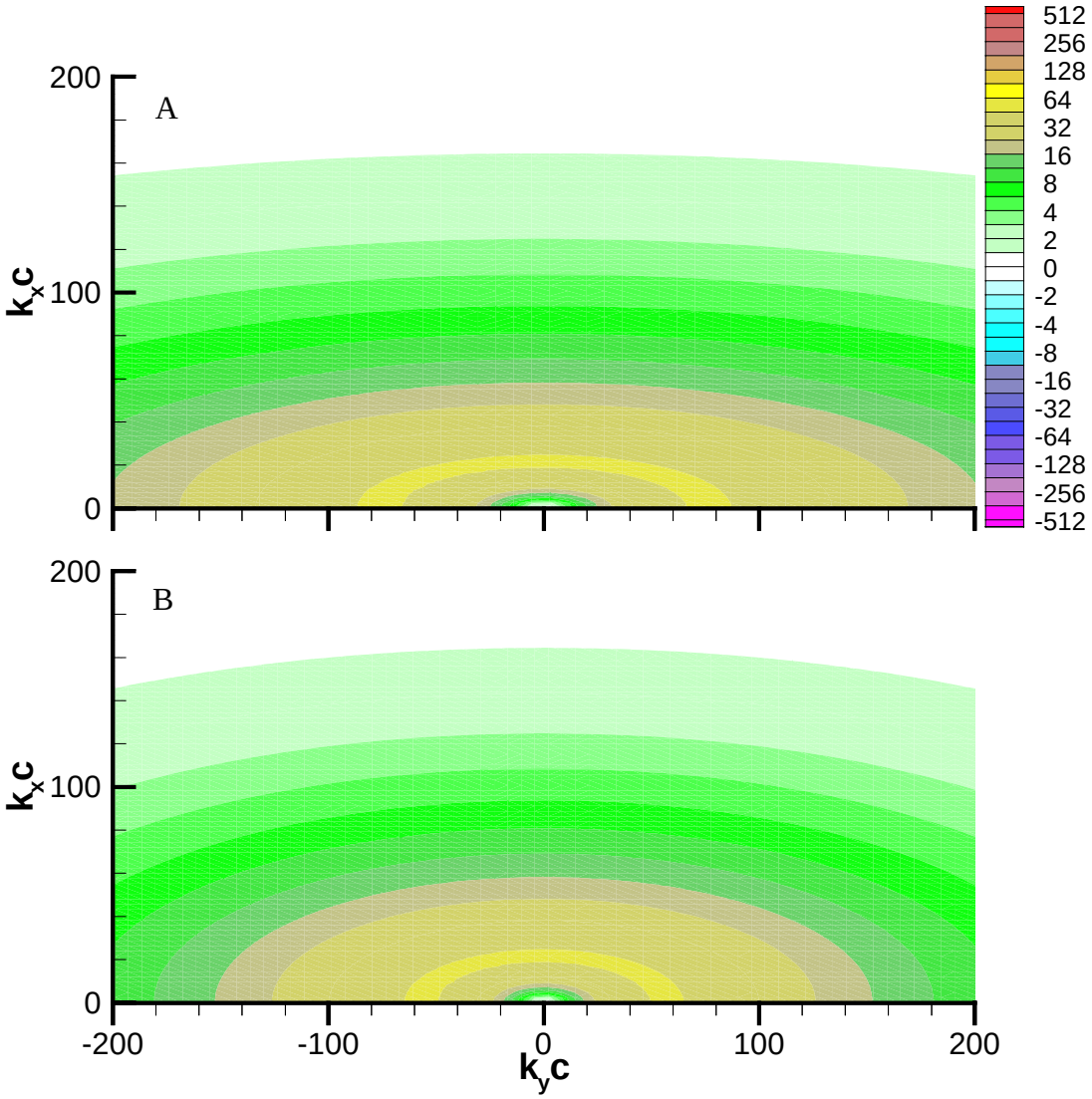

Figure 3.20

The von Kármán spectrum adjusted so that the ratio of streamwise and spanwise length scales more closely match those of A) the upwash spectrum of profile A/L1 (figure 3.9C) and B) the upwash spectrum of profile B/L2 (figure 3.13C).

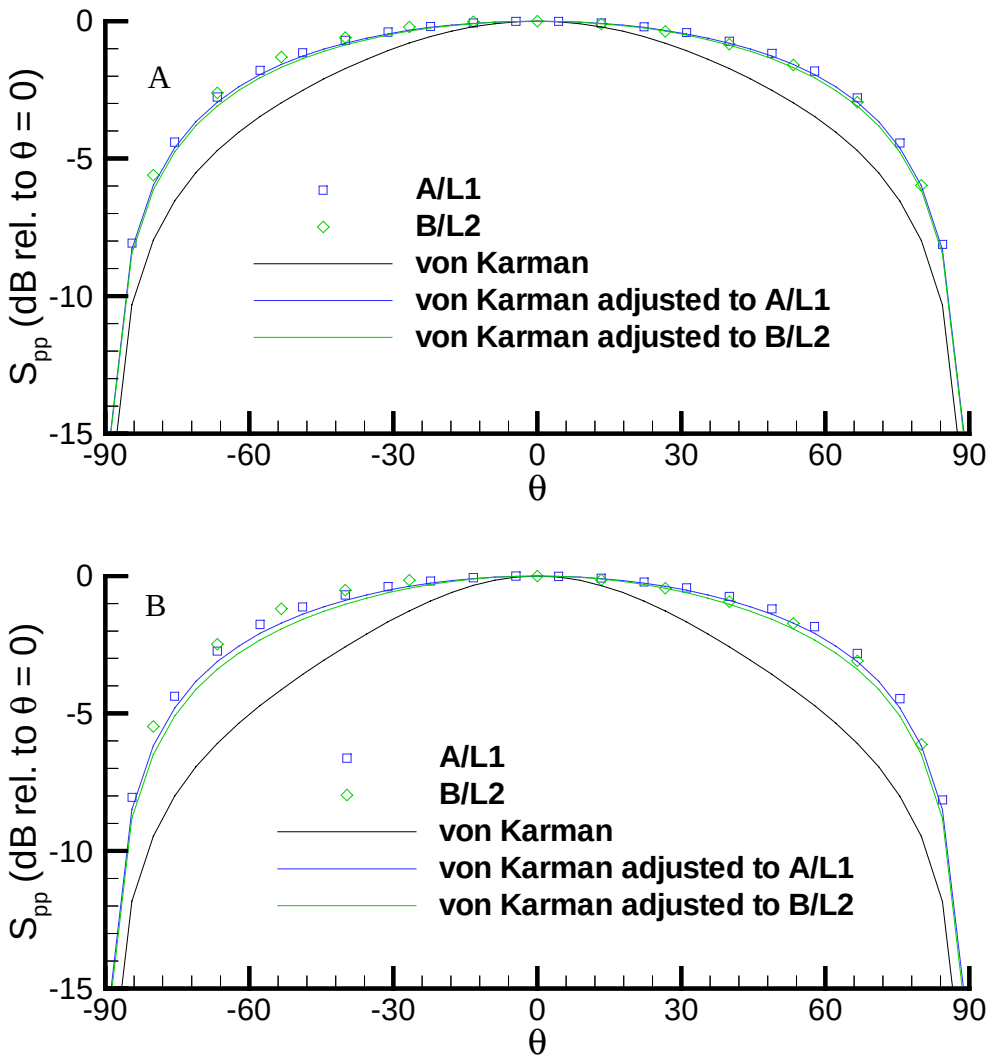

Figure 3.21

Comparisons of directionality calculated from von Karman spectra that were adjusted to produce results more closely matching the results from the measured spectra. For A) $K_x/k_e = 1.5$ and for B) $K_x/k_e = 6.0$.

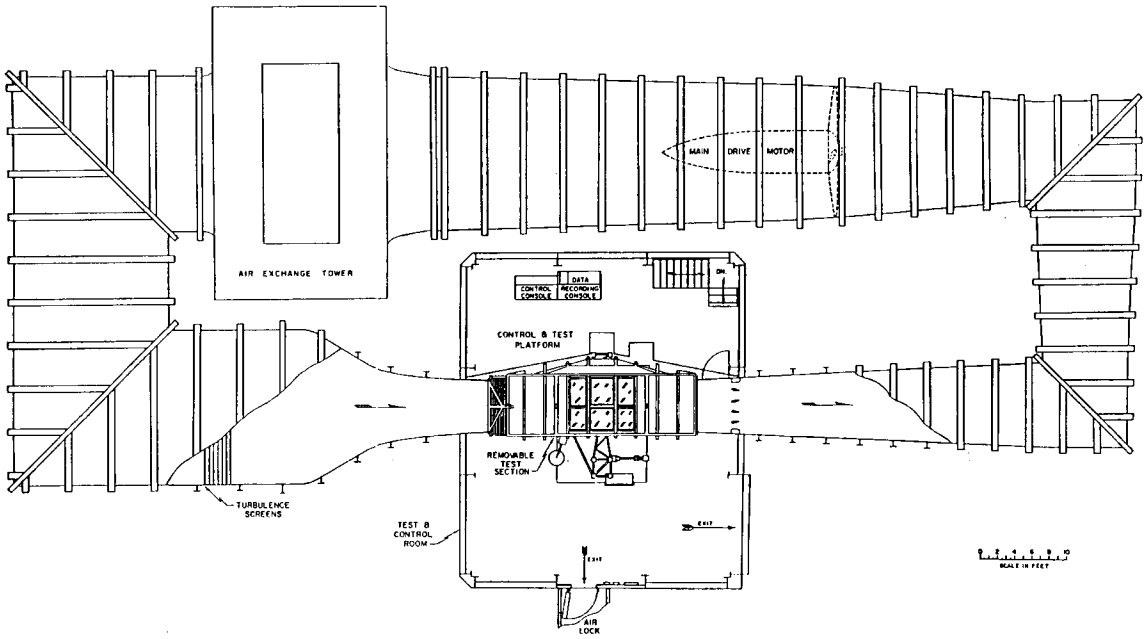

Figure 4.1

A diagram of the Virginia Tech Stability Wind Tunnel.

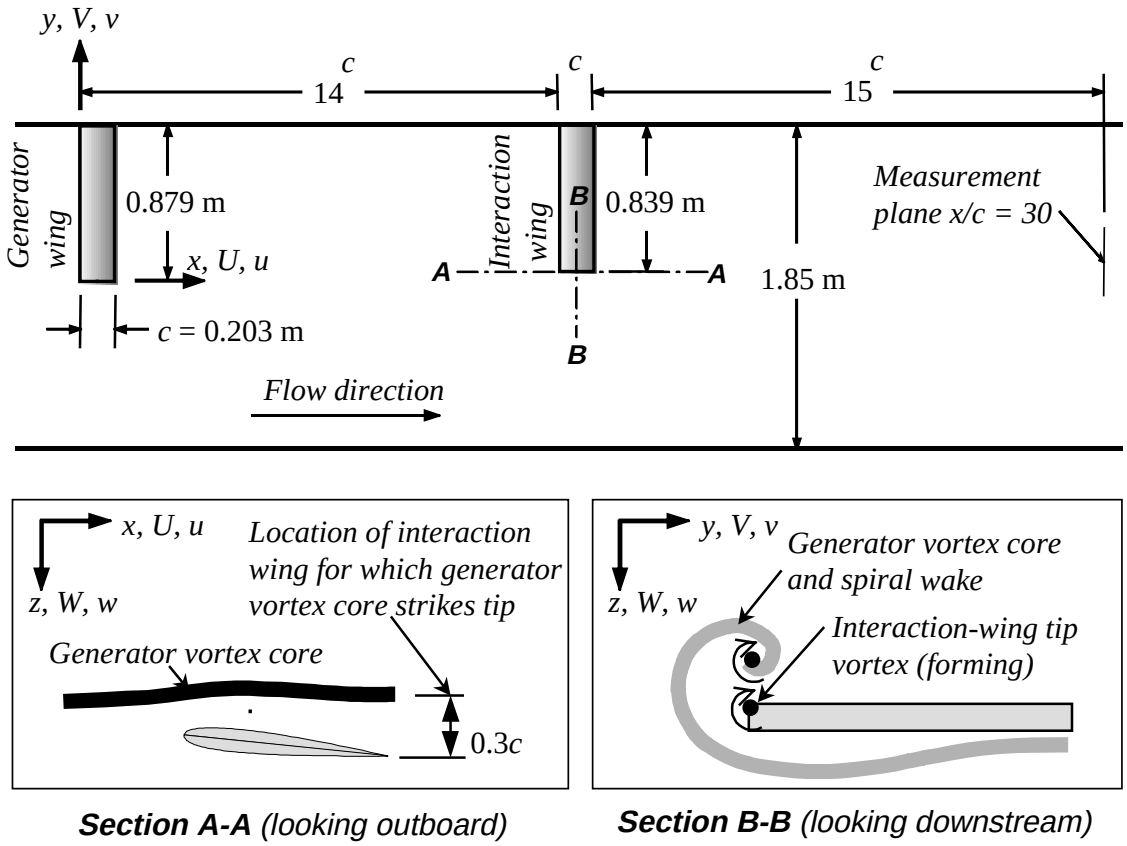

Figure 4.2

A diagram of the experimental test setup. Taken from Wittmer *et al*. (1998).

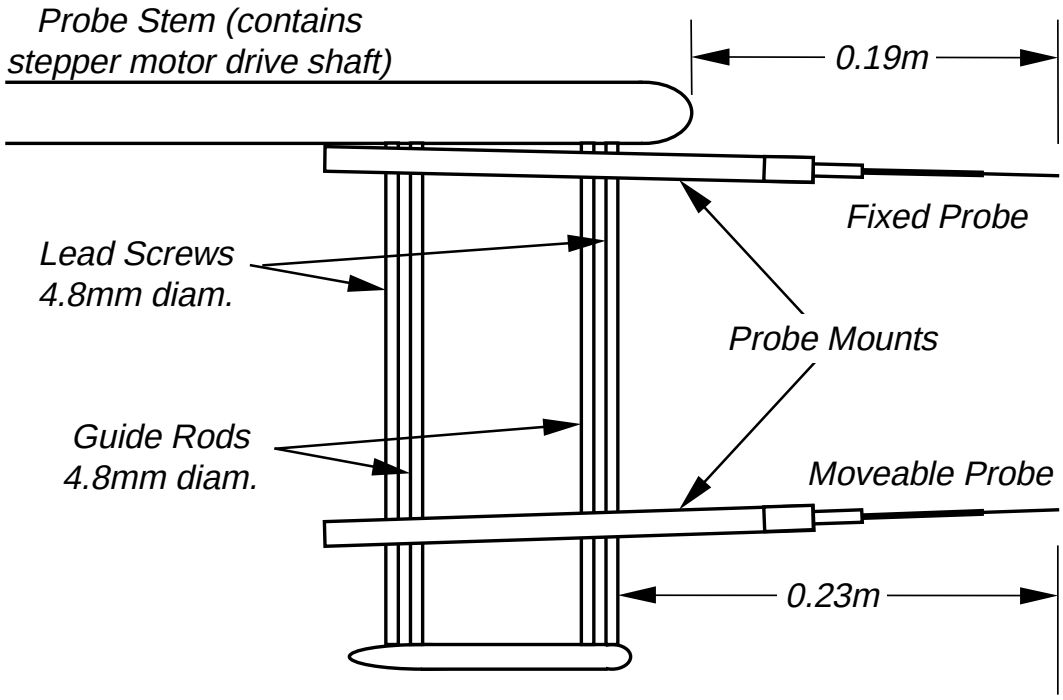

Figure 4.3

A diagram of the two-probe holder used to take two-point profiles. The upper probe is kept fixed, while the lower probe can be moved using a computerized traverse. Taken from Wittmer *et al*. (1998)

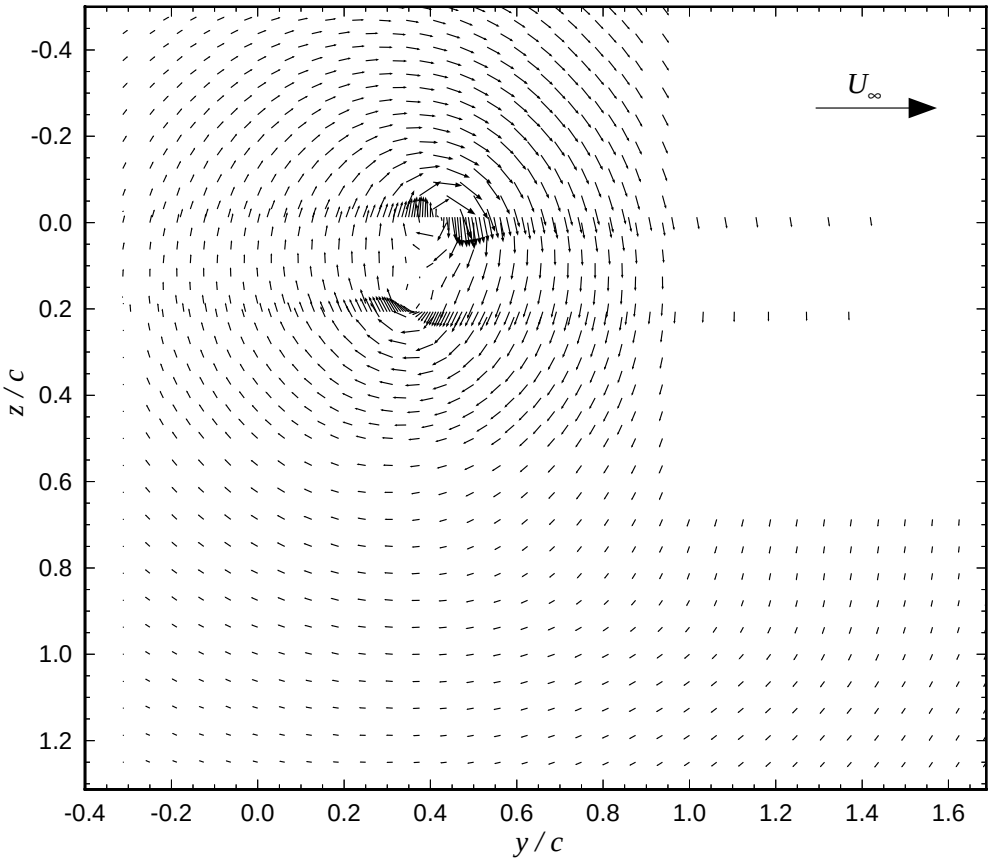

Figure 4.4

Mean cross flow velocity vectors. Taken from Devenport *et al*. (1997).

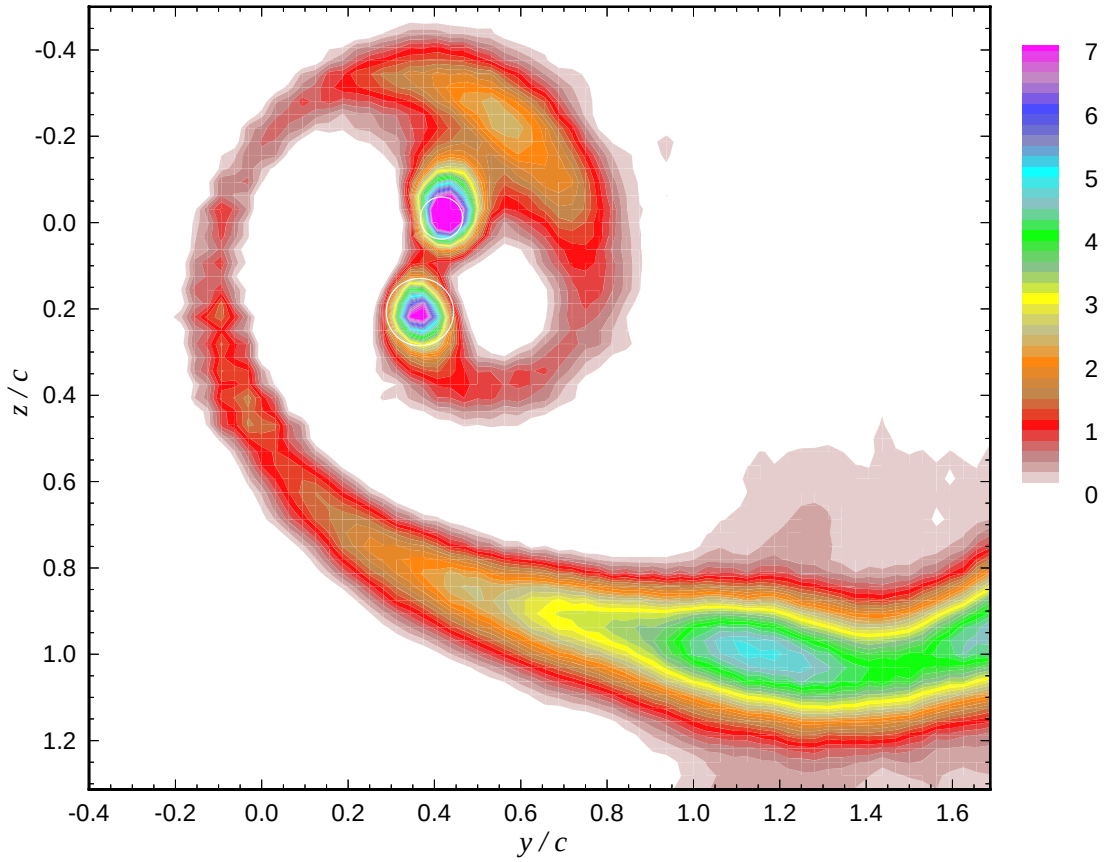

Figure 4.5

Contours of mean axial velocity deficit, $(1 - U/U_\infty) \times 100$. The white circles estimate the edges of the vortex cores. Taken from Devenport *et al*. (1997).

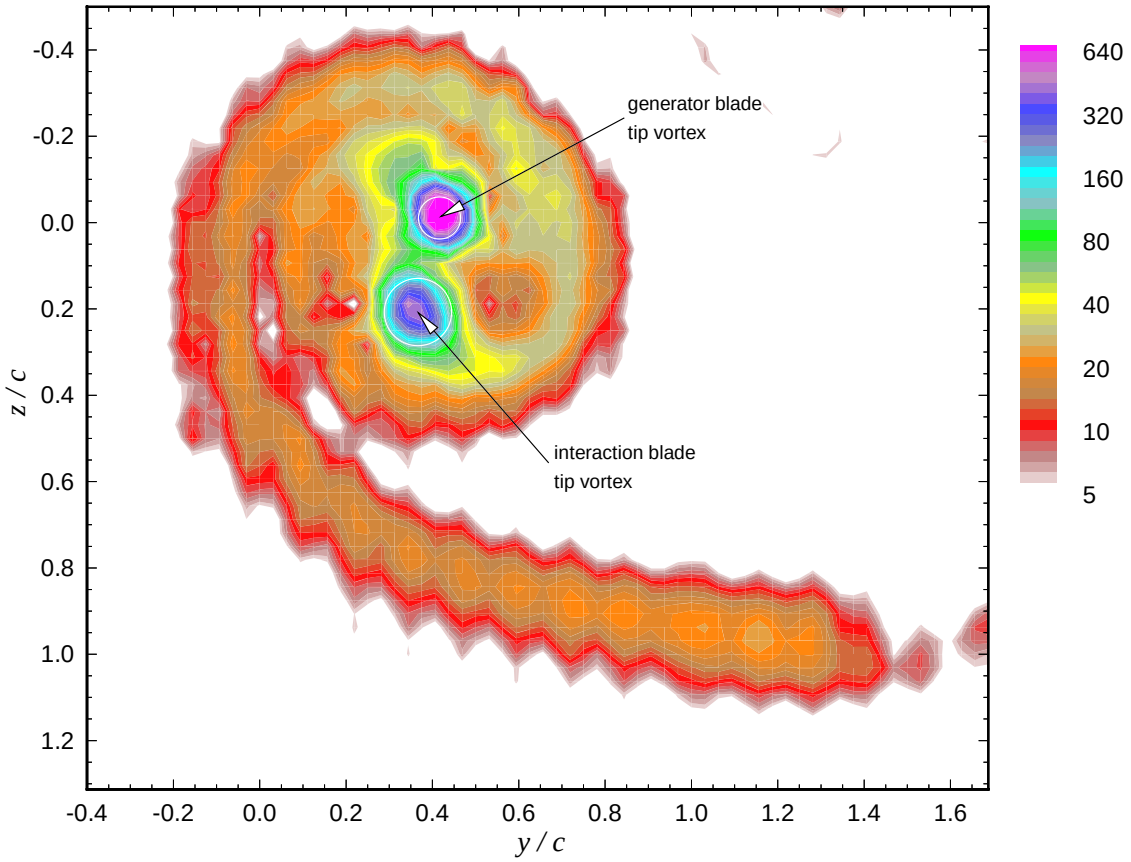

Figure 4.6

Contours of mean streamwise vorticity, $\Omega_x c/U_\infty \times 100$. The white circles estimate the edges of the vortex cores. Taken from Devenport *et al*. (1997).

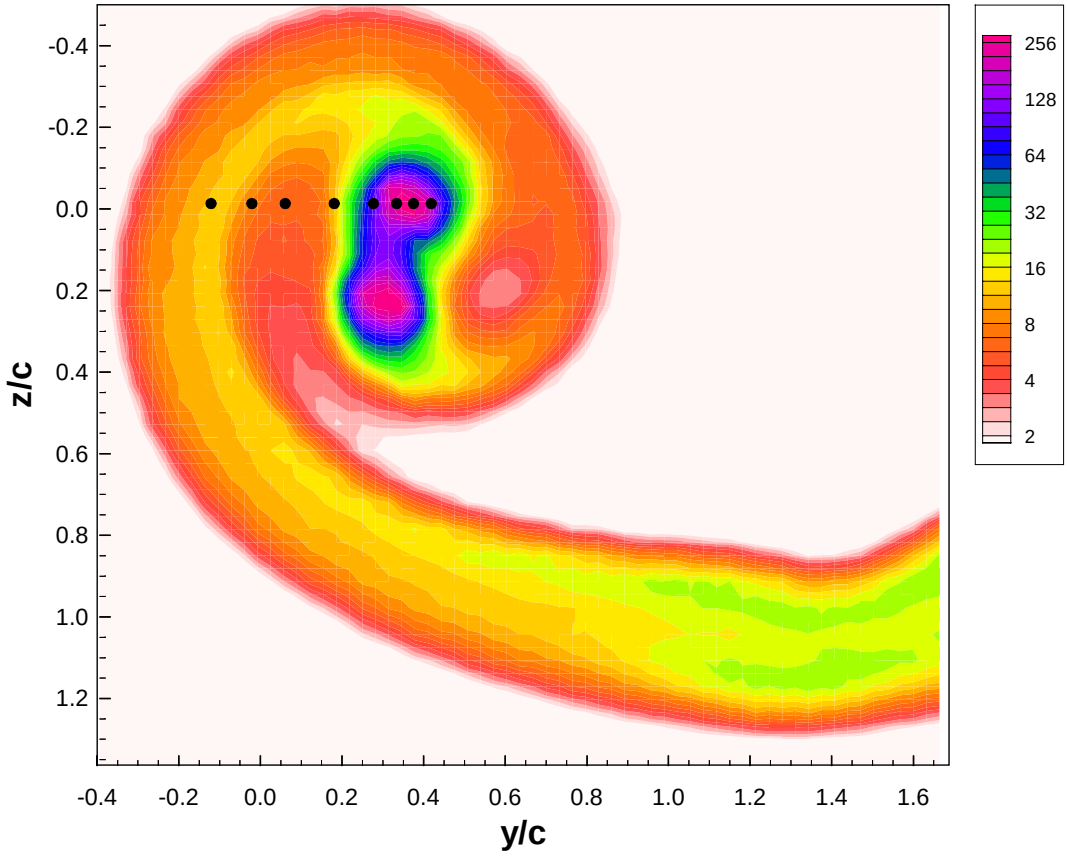

Figure 4.7

Contours of axial turbulence stress, $\overline{u^2}/U_\infty^2 \times 10^5$. The black dots indicate the locations of the autospectra plotted in figure 4.15.

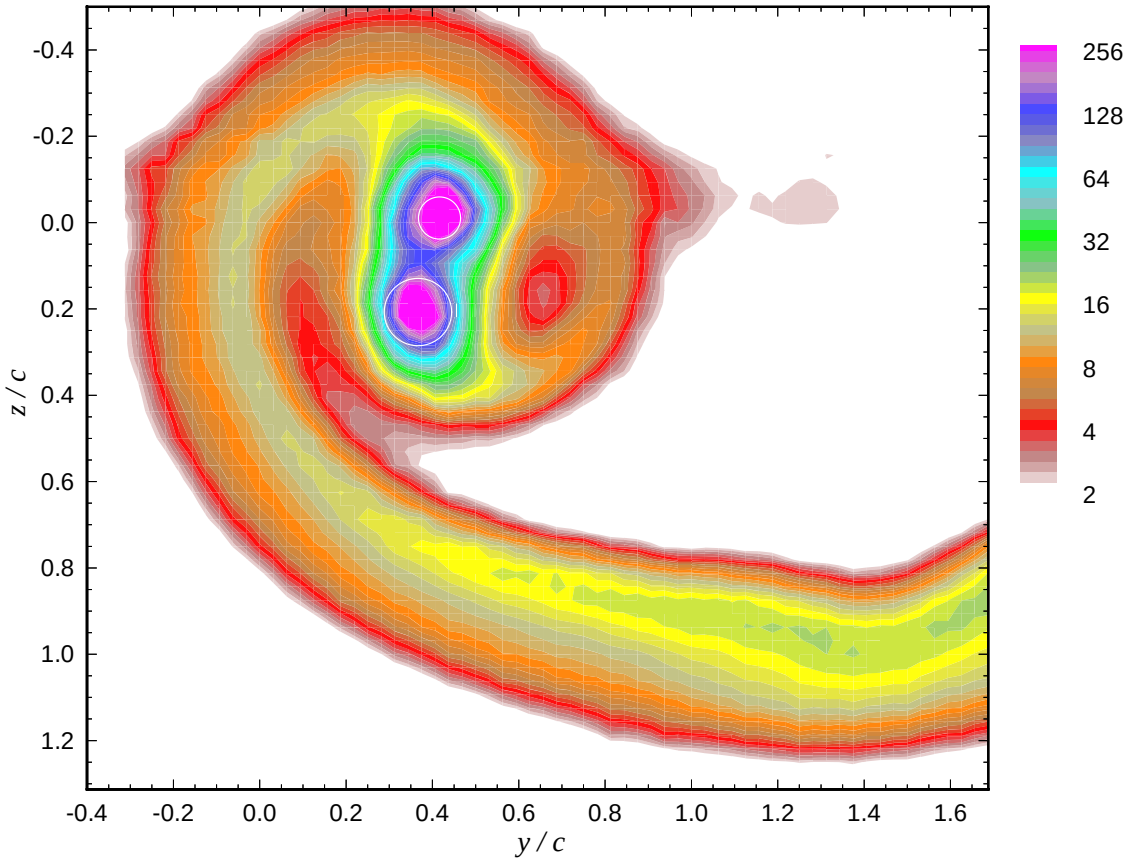

Figure 4.8

Contours of summed cross flow normal turbulence stresses, $\frac{1}{2}\left(\overline{v^2}+\overline{w^2}\right)/U_\infty^2 \times 10^5$. The white circles estimate the edges of the vortex cores. Taken from Devenport *et al*. (1997).

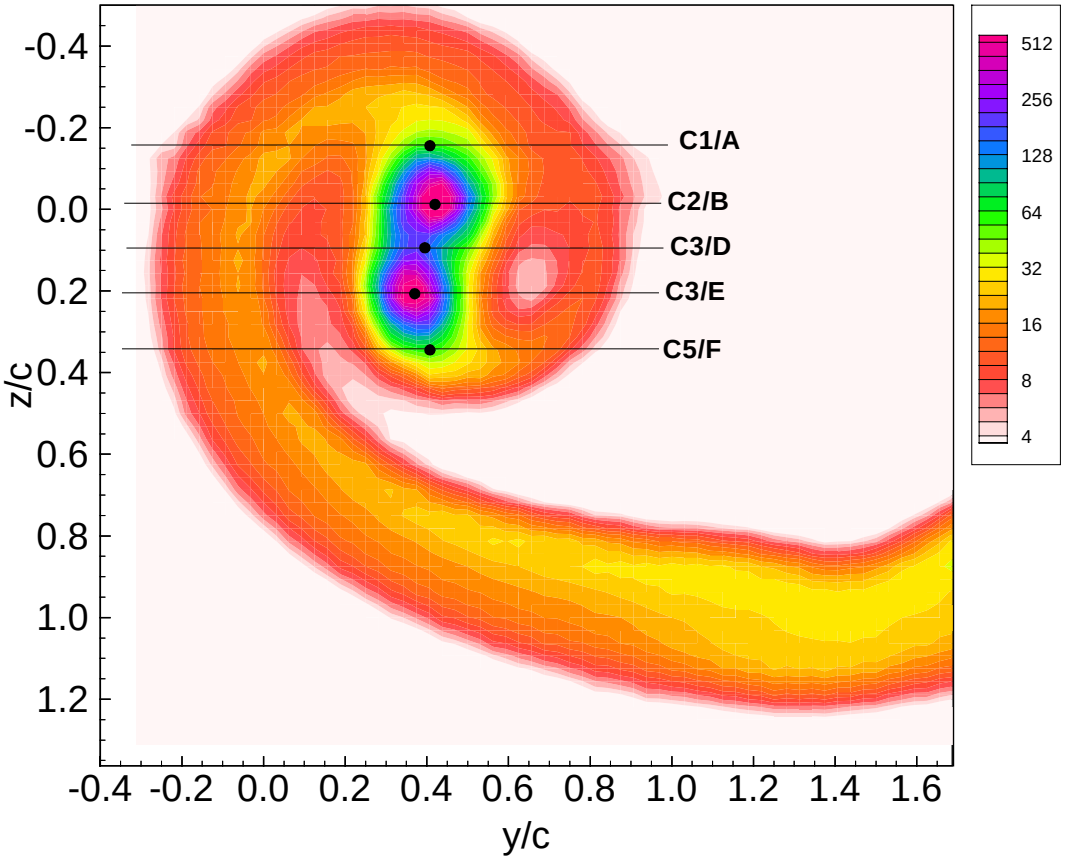

Figure 4.9

Contours of turbulence kinetic energy, $k/U_\infty{}^2 \times 10^5$. The lines show the two sides two-point profiles (C1 - C5). The black dots (A, B, D, E, F) indicate the fixed probe locations.

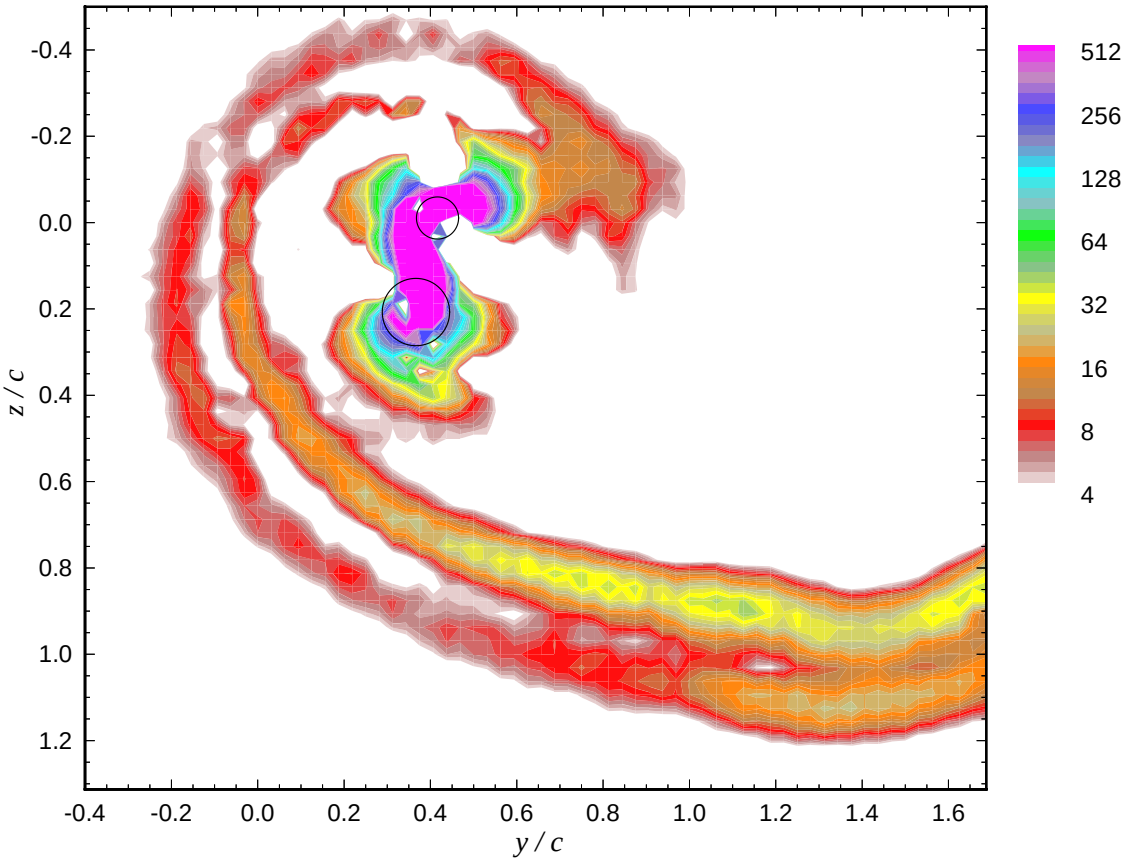

Figure 4.10

Contours of turbulence kinetic energy production, $Pc/U_\infty{}^3 \times 10^6$. The black circles estimate the edges of the vortex cores. Taken from Devenport *et al*. (1997).

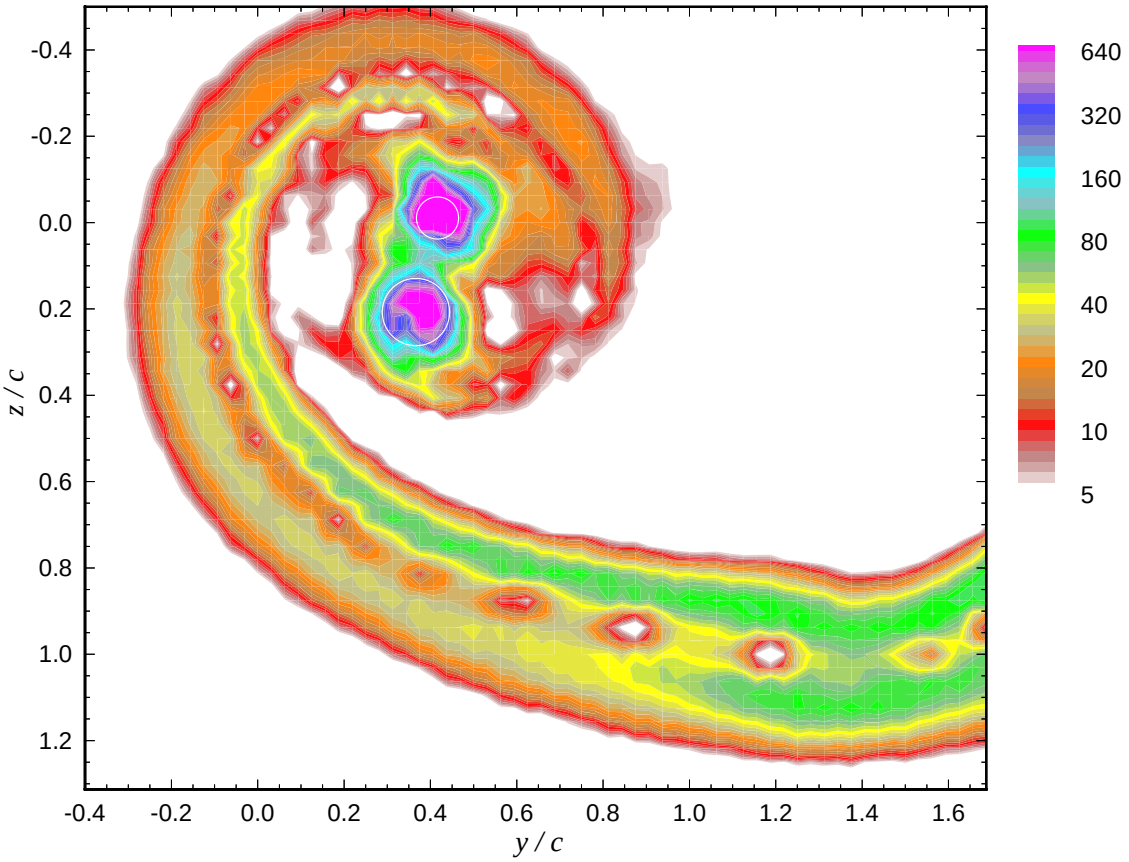

Figure 4.11

Contours of axial shear stress magnitude, $\tau_x/U_\infty^2 \times 10^6$. Taken from Devenport *et al*. (1997).

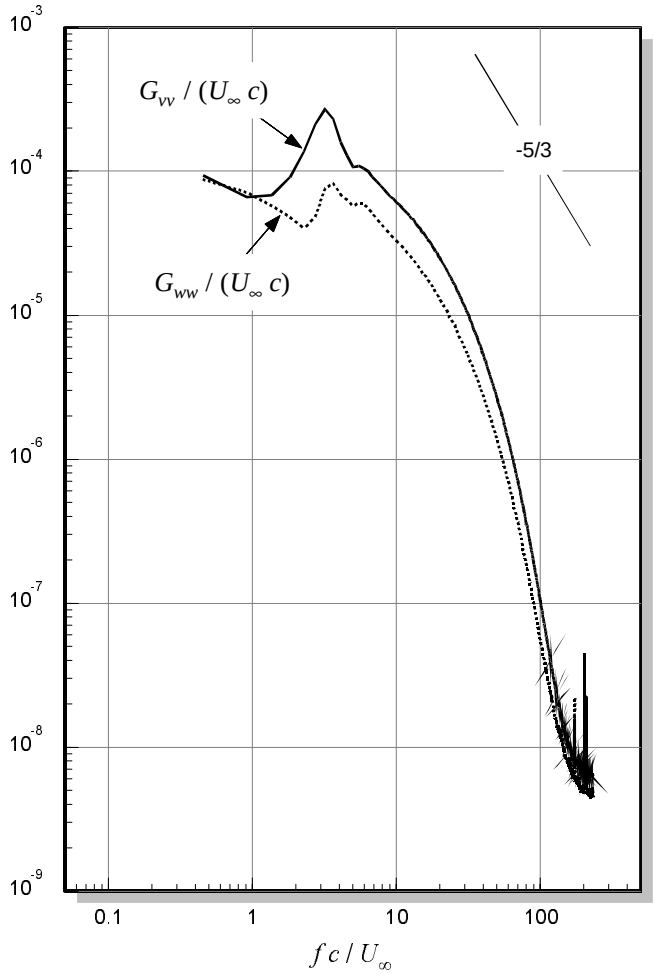

Figure 4.12

Velocity autospectra at location D (see figure 4.9) between the vortex cores. Taken from Devenport *et al*. (1997).

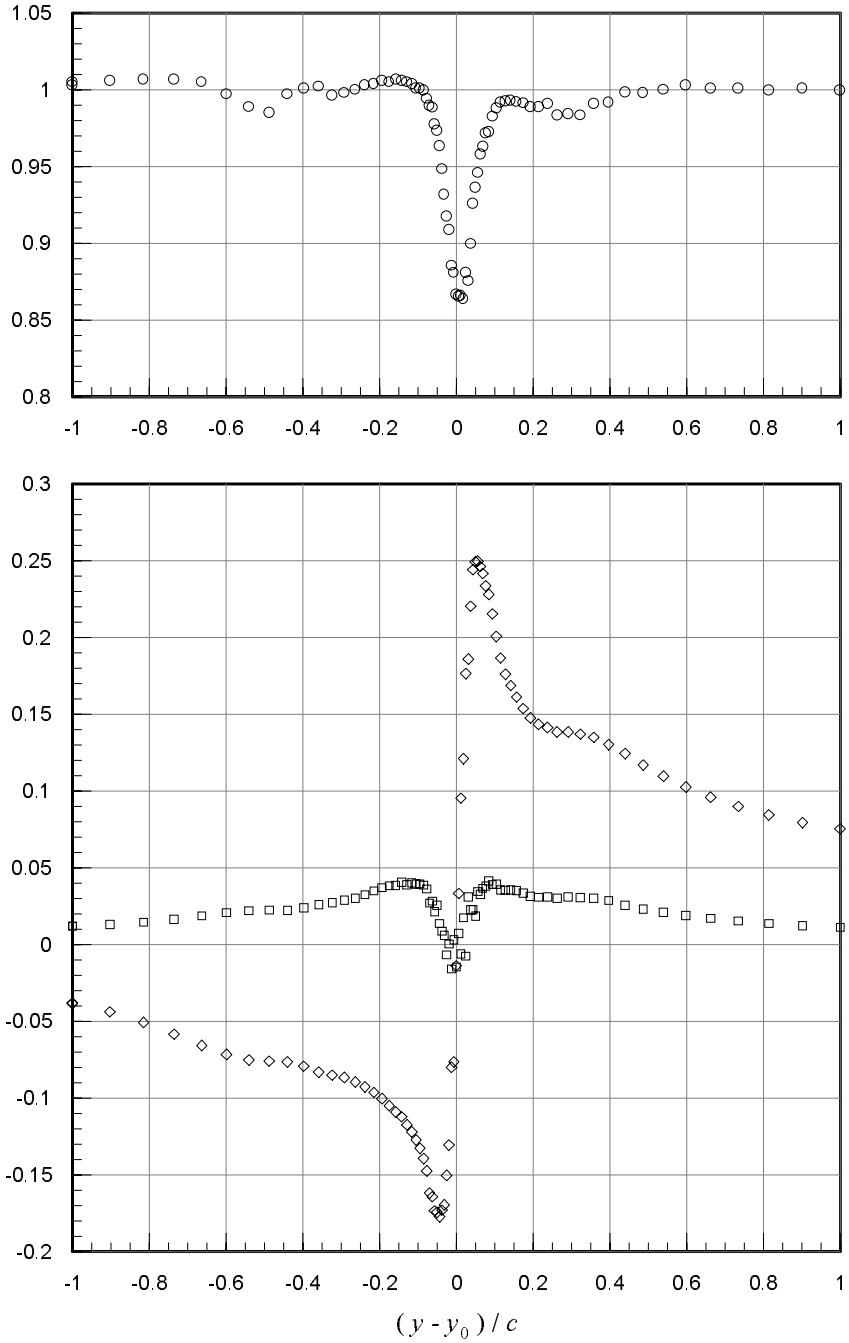

Figure 4.13

Mean velocities (U/U_∞ = O, V/U_∞ = □, W/U_∞ = ◊) measured through the generator vortex core. Taken from Devenport *et al*. (1997).

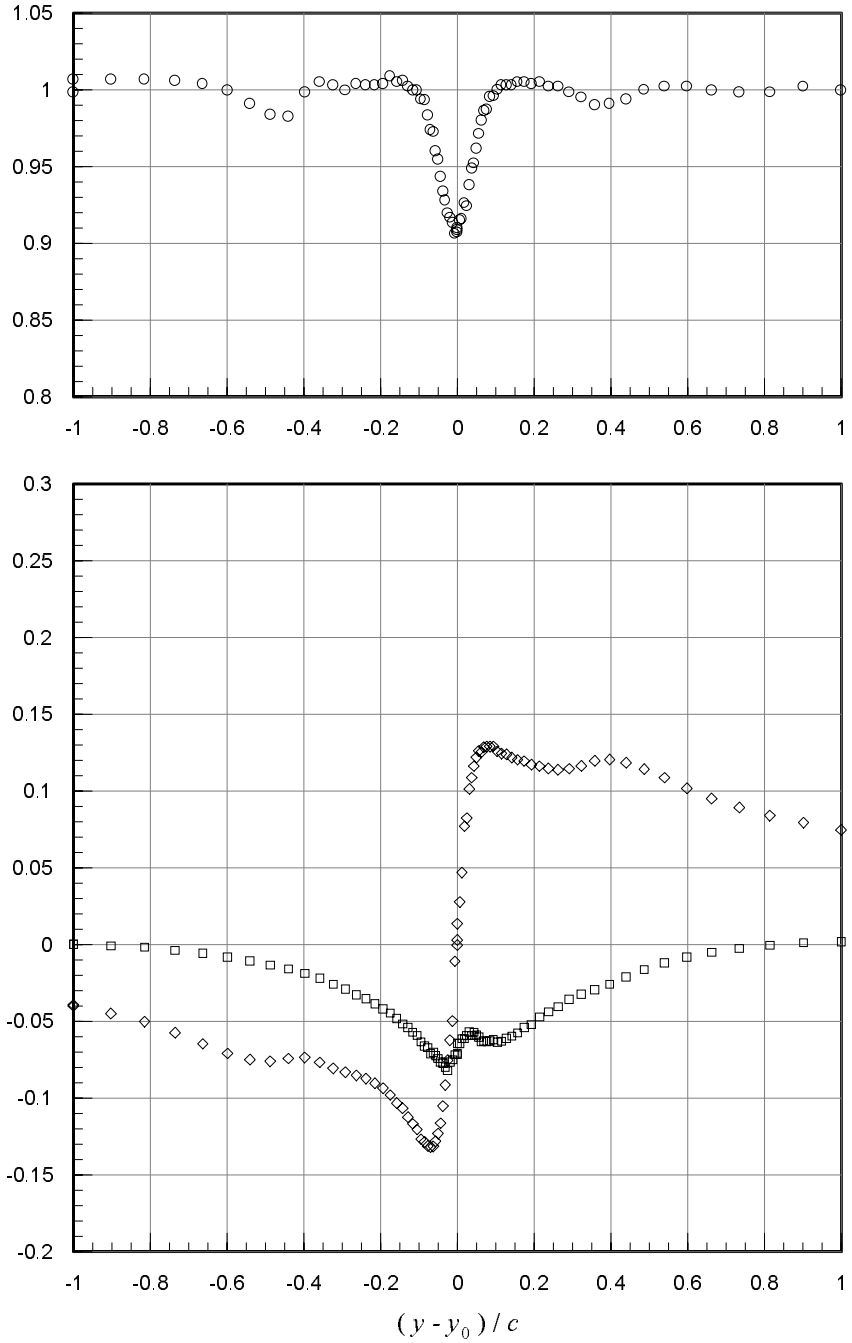

Figure 4.14

Mean velocities (U/U_∞ = O, V/U_∞ = □, W/U_∞ = ◊) measured through the interaction vortex core. Taken from Devenport *et al*. (1997).

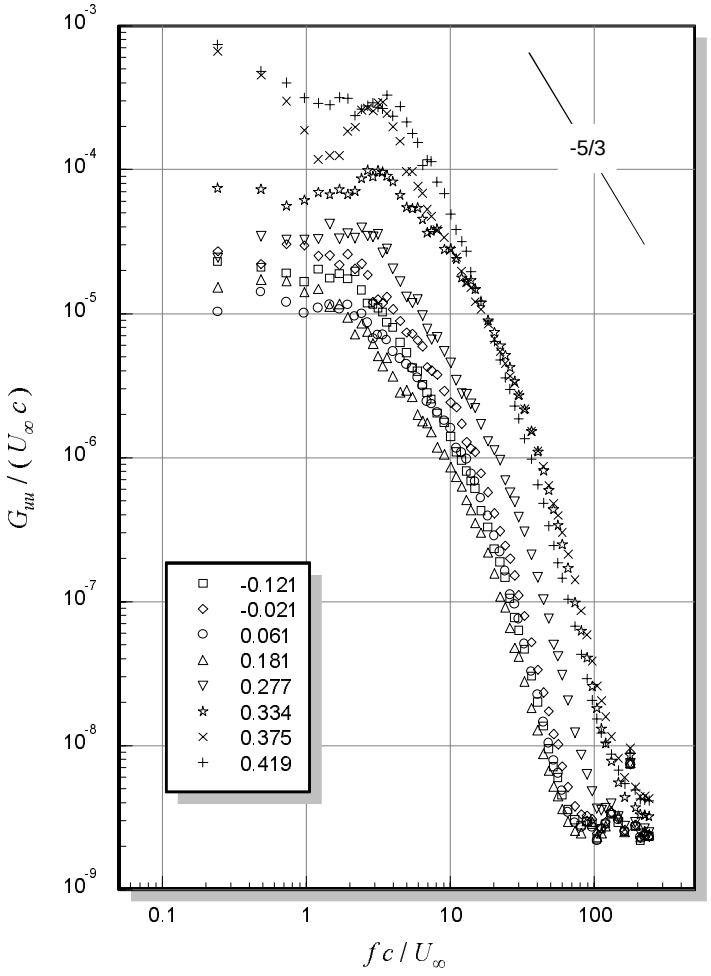

Figue 4.15

Axial component velocity autospectra at locations shown in figure 4.7. The numbers in the legend indicate the *y*/*c* values.

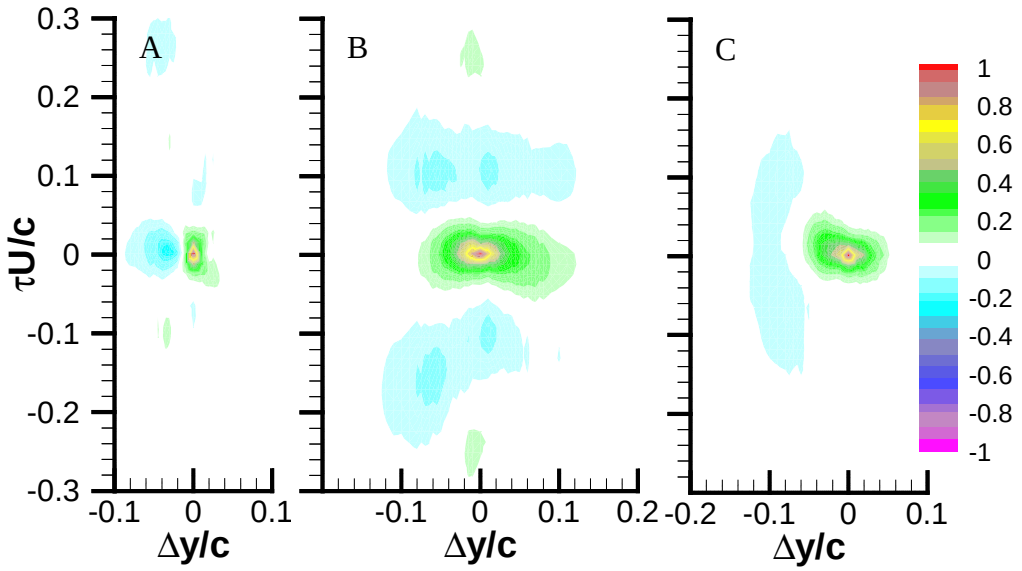

Figure 4.16

The cross-correlation functions for two-point profile C3 (figure 4.9). Plot A is $\frac{R_{uu}}{\overline{u^2}}$, plot B is $\frac{R_{vv}}{\overline{v^2}}$, and plot C is $\frac{R_{ww}}{\overline{w^2}}$.

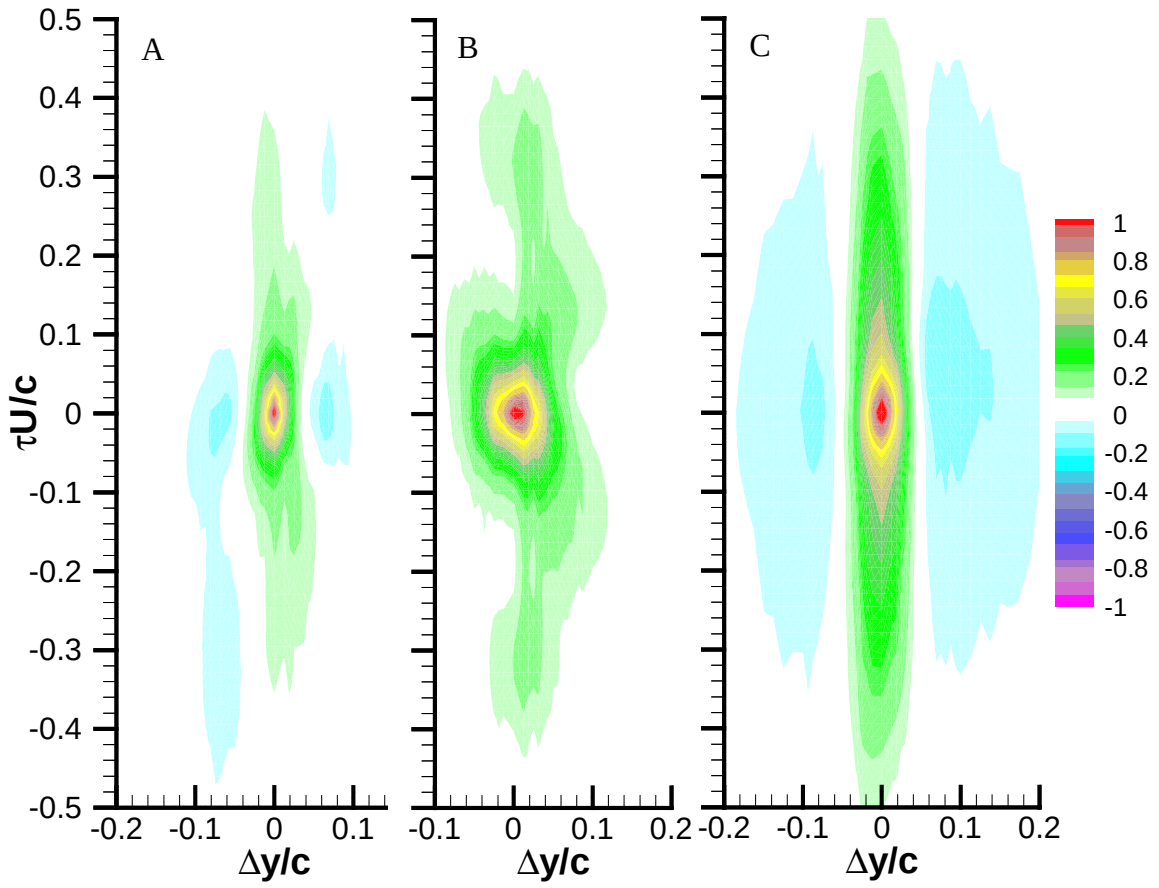

Figure 4.17

The cross-correlation functions for two-point profile C4 (figure 4.9). Plot A is $\frac{R_{uu}}{\overline{u^2}}$, plot B is $\frac{R_{vv}}{\overline{v^2}}$, and plot C is $\frac{R_{ww}}{\overline{w^2}}$.

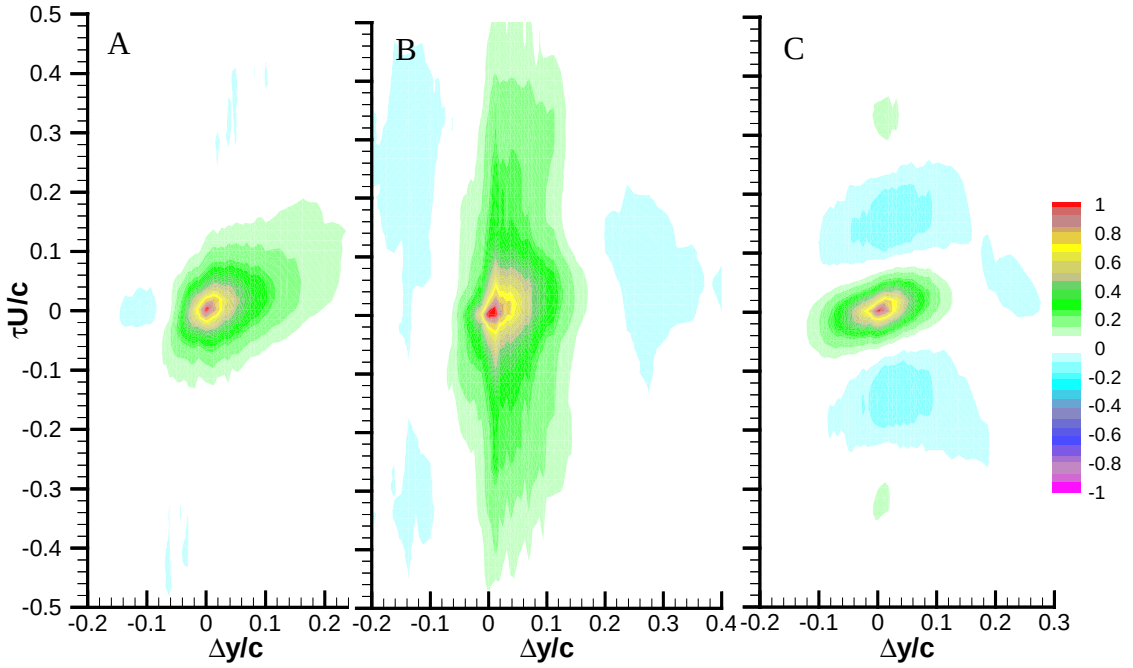

Figure 4.18

The cross-correlation functions for two-point profile C5 (figure 4.9). Plot A is $\frac{R_{uu}}{\overline{u^2}}$, plot B is $\frac{R_{vv}}{\overline{v^2}}$, and plot C is $\frac{R_{ww}}{\overline{w^2}}$.

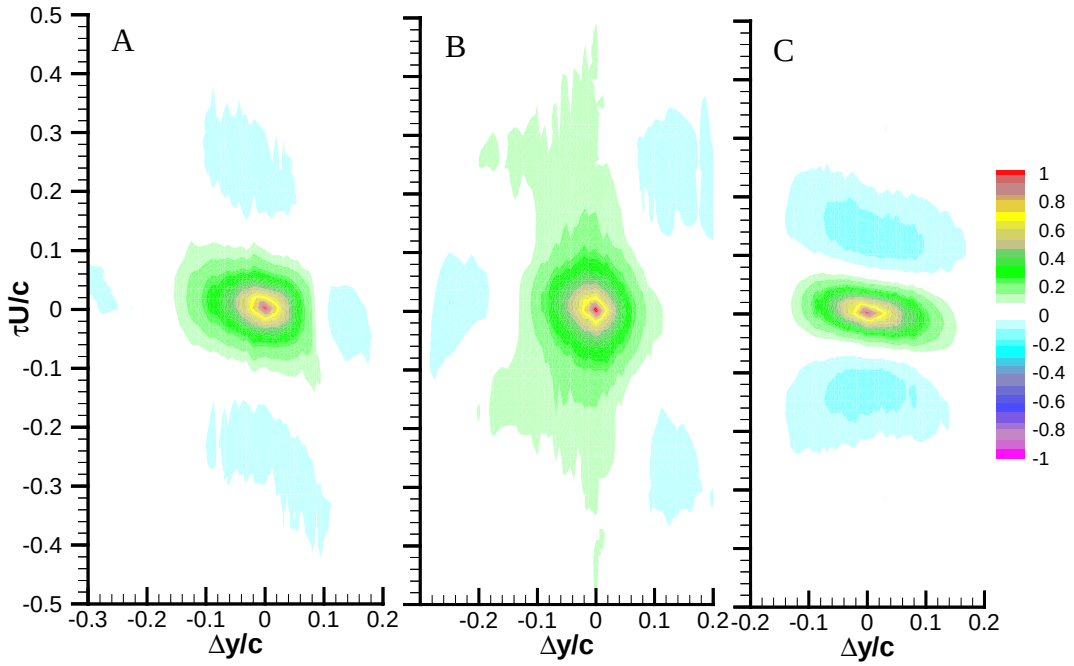

Figure 4.19

The cross-correlation functions for two-point profile C1 (figure 4.9). Plot A is $\frac{R_{uu}}{\overline{u^2}}$, plot B is $\frac{R_{vv}}{\overline{v^2}}$, and plot C is $\frac{R_{ww}}{\overline{w^2}}$.

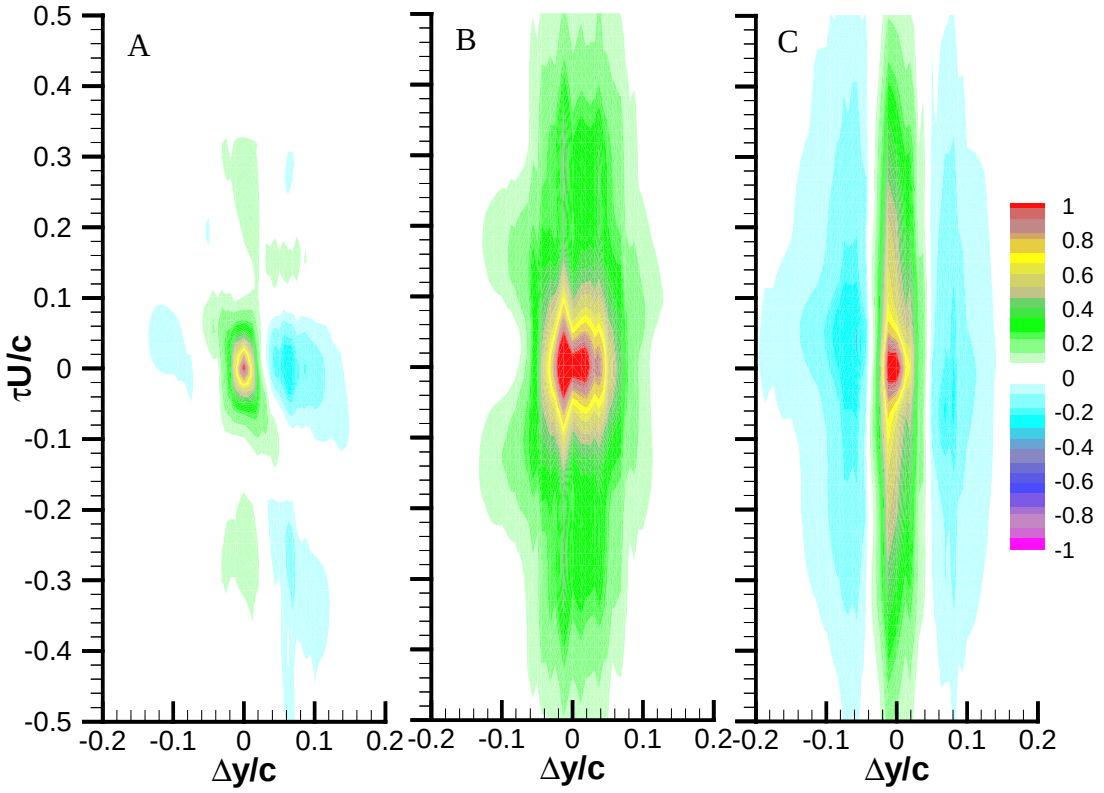

Figure 4.20

The cross-correlation functions for two-point profile C2 (figure 4.9). Plot A is $\frac{R_{uu}}{\overline{u^2}}$, plot B is $\frac{R_{vv}}{\overline{v^2}}$, and plot C is $\frac{R_{ww}}{\overline{w^2}}$.

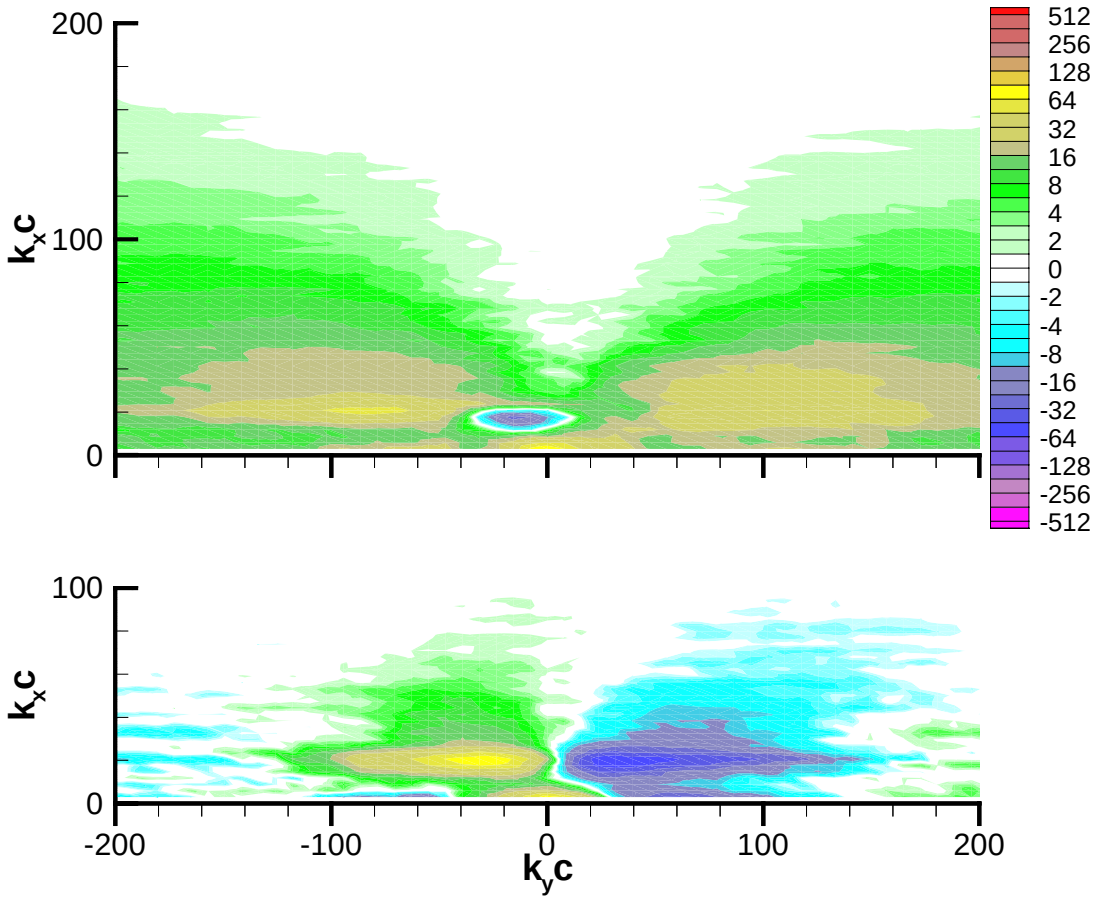

Figure 4.21

Wave number frequency spectrum of the axial (u) velocity component calculated for two-point profile C3 (see figure 4.9). Contours of the real component of $\frac{\phi_{uu}}{\overline{u^2}\,\overline{c^2}} \times 10^6$ are shown on top and the imaginary part on bottom.

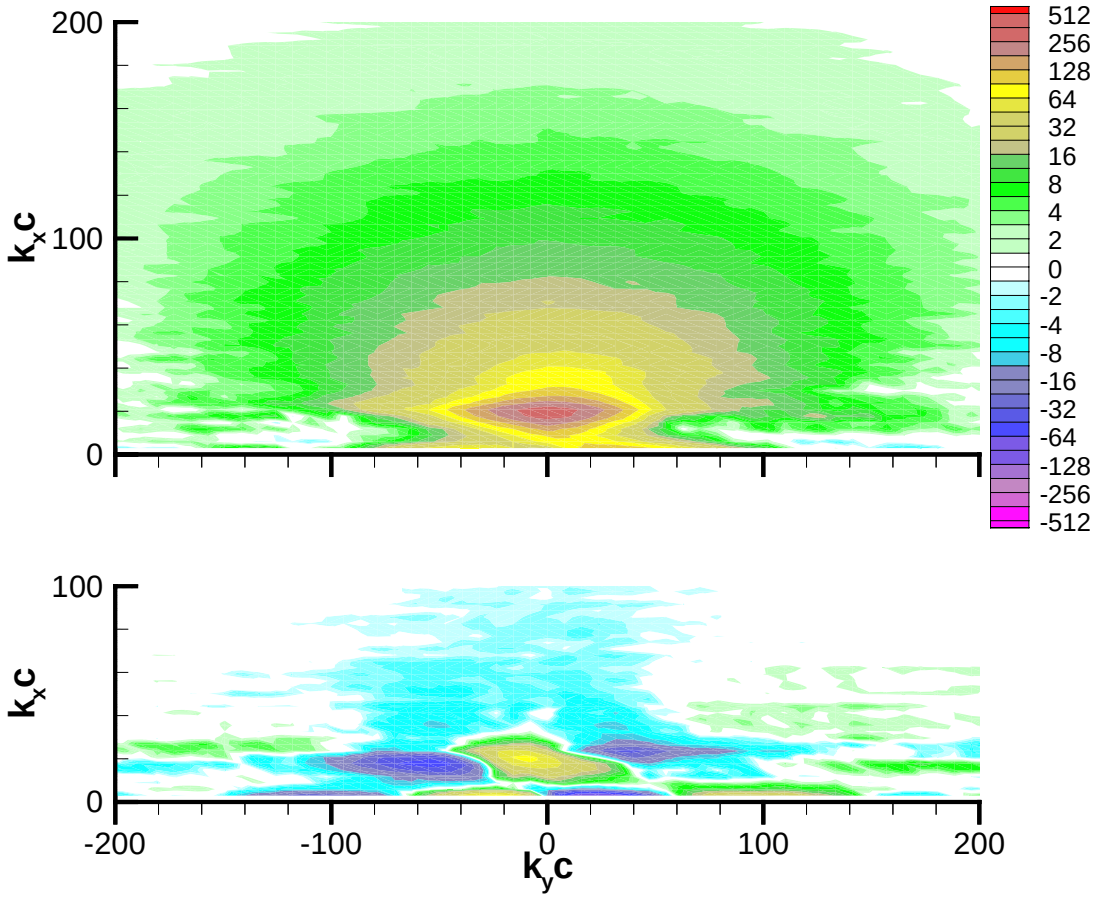

Figure 4.22

Wave number frequency spectrum of the spanwise (v) velocity component calculated for two-point profile C3 (see figure 4.9). Contours of the real component of $\frac{\phi_{vv}}{\overline{v^2}\,\overline{c^2}} \times 10^6$ are shown on top and the imaginary part on bottom.

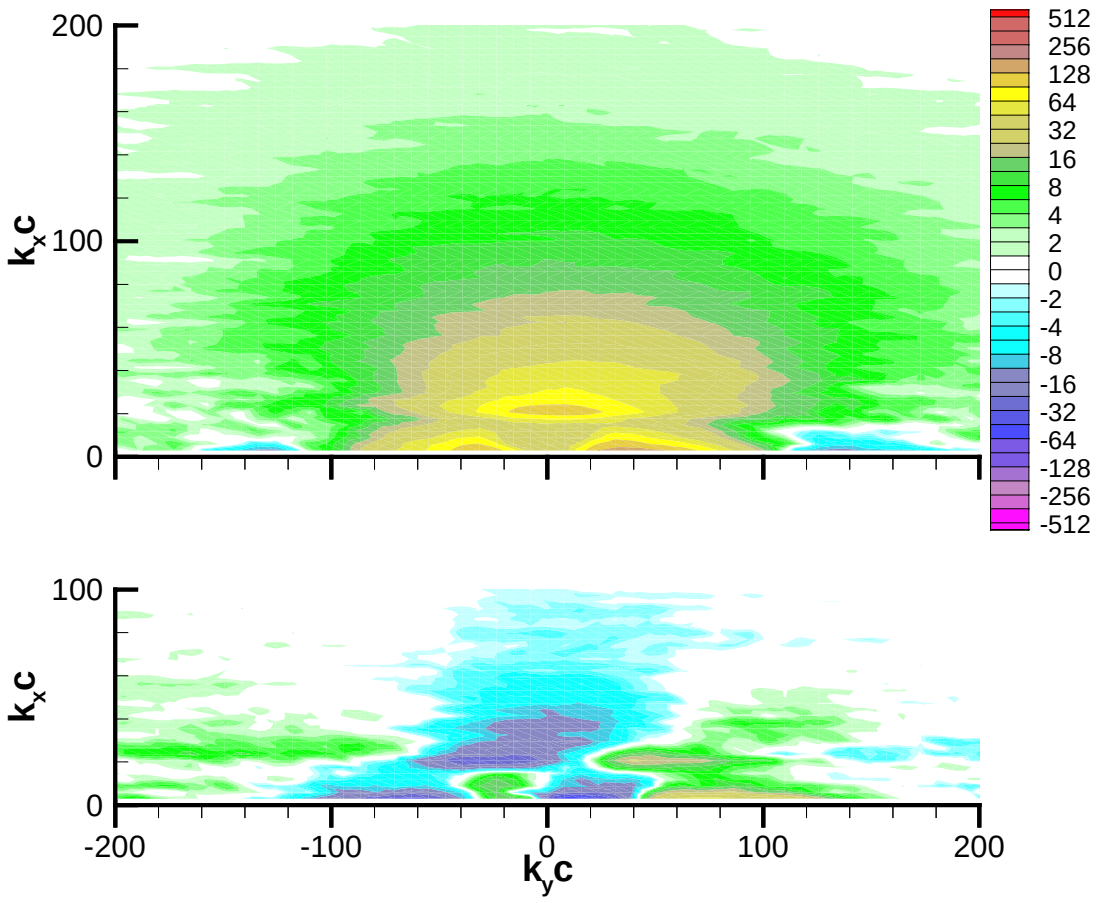

Figure 4.23

Wave number frequency spectrum of the upwash (w) velocity component calculated for two-point profile C3 (see figure 4.9). Contours of the real component of $\frac{\phi_{ww}}{\overline{w^2}\,\overline{c^2}} \times 10^6$ are shown on top and the imaginary part on bottom.